

https://dspace.org/

A real-time turbulence simulator

Mashaba, Nikiwe Precious

2021
https://hdl.handle.net/10539/32379

Downloaded from a DSpace repository. https://dspace.org/

A REAL-TIME TURBULENCE SIMULATOR

Nikiwe Precious Mashaba
Supervisor: Prof A. Forbes



A dissertation submitted to the Faculty of Science, University of the Witwatersrand, Johannesburg, in fulfilment of the requirements for the degree of Master of Science

Declaration

I, Nikiwe Precious Mashaba, declare that the work is carried out by the author alone. Any or whole part of the work has not been submitted before in order to qualify for any other academic degree. The content of the dissertation is the result of work which has been carried out since the date of approval of the research study. All procedures have been followed while preparing this dissertation, according to the University's requirements.

Signed: 

Date: 08 January 2021

Abstract

Optical communication and imaging systems that benefit from the transmission and detection of light propagated through the atmosphere have become essential for numerous practical applications, e.g., for long distance communication, LIDAR systems or imaging. In many applications light is used for target tracking and distance measurements or for telescopes used in astronomical observations. However, the irregular motion of air can distort optical light fields, therefore hindering the performance of optical systems. This happens due to density fluctuations which result in refractive index fluctuations that randomly perturb the optical phase of the light. The result is near field phase fluctuations, which in severe cases may lead to far field intensity variations, giving rise to unwanted distortions. For this reason, the analysis of such effects on optical systems remains topical and of practical relevance.

In this dissertation we will focus on the impact of atmospheric turbulence on the transmission of spatial modes of light. We will explore techniques for characterising optical turbulence and simulating its phase distortions in the lab environment. We use the simulated turbulence to study its impact on laser beams propagating in freespace and turbulence. The laser beams studied here are eigen-modes of freespace that can carry orbital angular momentum (OAM). The modes are associated with spatially inhomogeneous polarisation fields, known as vector vortex modes, having spatial profiles that are characterised by the Laguerre-Gaussian (LG) modes. We will discuss the principle of generating and detecting such spatial modes by tailoring the dynamic phase of the spatial mode of light using Liquid Crystal (LC) displays and digital micromirror devices (DMDs). Subsequently, we study how both the polarisation and spatial components are affected by turbulence using the same tools. Finally,

we will introduce a device called the sonic anemometer to extract velocity data, and we will use this data to calculate parameters that quantify the levels of atmospheric distortions due to optical turbulence. A modern digital micromirror device (DMDs) will then be used to execute a turbulence simulator and show that using digitally encoded phase screens we can accurately mimic realistic turbulence.

Dedication

To my family

and
my people eManyeveni

Acknowledgements

To my great supervisor Professor Andrew Forbes. Thank you for your leadership, brilliance, inspiration, encouragement, enormous experience, guidance, and being there for me.

I would like to thank my competency area manager Simphiwe Mkwelo and the Optronic Sensor Systems group from the CSIR for their immense support and for the golden opportunity that they have given me to pursue my studies. Thank you for the financial support that has fed me and my family.

To the Wits structured light family, there's a lot I learned from you everyday by watching you dealing with projects and quick reaction tasks. Thank you for showing me what makes a successful career. Not everyone is as lucky as I have been.

To my family who never have a graduate. Thank you for reminding me that education is a key to success and that poverty is not what defines you.

I also acknowledge with a deep sense of reverence, my gratitude towards my community (eManyeveni) for not shaming my poverty. I felt ashamed for being poor but they believed in my dreams since I was a young girl. Even though there's not a lot of hope in my community, I shall never forget where I come from because of the people's faith and encouragement. This made me realise that you are not where you come from. Thank you for trusting that I can do better.

Contents

List of Figures ix

List of Tables xvi

Chapter 1: Introduction 1

1.1 Background 2

1.2 Outline 3

1.3 Optical modes 4

1.3.1 The polarisation of light 5

1.3.2 The scalar spatial modes of light 7

1.3.3 Vector modes 10

1.4 Optical turbulence structure simulation 13

1.4.1 Turbulent flow 14

1.4.2 Statistical models of turbulence 16

1.4.3 Sonic anemometer 21

Chapter 2: Experimental techniques 24

2.1 Controlling the phase and amplitude of light with digital devices . . . 25

2.1.1 Generation of digital holograms with an amplitude-only device 25

2.1.2 Generation of holograms with liquid crystal displays 28

2.2 Characterising digital devices 33

2.2.1 Digital micromirror characterization 33

2.2.2 Conversion efficiency of a liquid crystal display 37

2.2.3 Fringe visibility of an interferometer 40

2.3 Generating vector beams using an interferometer 42

2.4 Vector quality factor 46
2.5 Experimental VQF measurements 49
2.6 Conclusions 50

Chapter 3: Experimental results 52

3.1 In-situ velocity measurements 54
3.1.1 Results and discussion 57
3.1.2 Simulating turbulence in the lab 58
3.1.3 Characterising optical turbulence in the laboratory 65
3.2 The robustness of structured light in turbulence 72
3.2.1 Confirming the factorisation relation. 75
3.2.2 Robustness for higher order modes 78
3.3 Conclusions 79

Chapter 4: Conclusion and future work 80

Bibliography 83

List of Figures

1-1 (a) A Poincaré Sphere (PS) representation of the polarisation of light. The right $|R\rangle$, and left $|L\rangle$ circular polarisations, the diagonal $|D\rangle$ and anti-diagonal $|A\rangle$, horizontal $|H\rangle$ and vertical $|V\rangle$ polarisation modes. (b) Analogous representation of OAM states in a given subspace $|\ell|$ of a Bloch sphere. The term Bloch sphere refers to a geometrical representation of the pure state space of a two-level mechanical system. . . . 7

1-2 The intensities of Laguerre-Gaussian modes. The ℓ index controls the size of the vortex seen as a zero intensity and as a phase singularity. The p index controls the number of concentric radial zero-intensity rings. . 8

1-3 Phase maps of Laguerre-Gaussian modes depending on the ℓ and p indices. 9

1-4 The superimposed polarisation and intensity field of a (a)-(c) scalar and a (d)-(e) vector modes. The arrows indicate the vector of the polarisation distribution. This figure will be useful in Chapter 3. 12

1-5 Distortion of a spherical wavefront in turbulence (shown as pink ellipse). This result the final wavefront at some distance away from the normal. The laser beam intensity reduces as the beam propagates further due to the obstacles (e.g., turbulence or aerosols). 14

1-6 Fluid motion; namely, laminar (top) and turbulent (bottom) flow. Here the arrows for laminar flow indicate uniform airflow of the velocity. Whereas the velocity of the airflow (shown as random arrows) for turbulent flow medium indicate random speeds of the liquid. 15

1-7 Representation of the stages involved in creating turbulent flow. Here, (l_0) and (L_0) are the inner and outer scale of turbulence. Kolmogorov turbulence assumes $l_0 = 0$ and $L_0 = \infty$ which simplifies the model significantly [1]. 17

1-8 Free-space propagation of an optical beam through a turbulent medium. Here the Gaussian beam is propagated through random turbulence phase screens and the final wavefront gets distorted. 21

1-9 Two views of a sonic anemometer transducer, dotted lines show transducer pairs. The angle between these three transducers is 60 degrees, which means that no ultrasonic pulse can interfere with the other. The U, V, and W component represent the "red", "green", and "blue" colours. 22

1-10 Time of flight mechanism. The transducers are separated by distance, d. The symbol t_1 and t_2 are the travelling times for each sonic pulse. . 23

2-1 A digital micromirror device (DMD) display. The DMD is made up of micromirrors and can be controlled in a binary fashion (the micromirrors can be set to +12 degrees and -12 degrees from its normal), using DLP Lightcrafter software. 25

2-2 Examples of holograms created to shape light using a digital micromirror device. (a) Field amplitude with an increasing azimuthal index of Laguerre Gaussian (LG) beams. (b) Binary phase holograms. (c) Binary amplitude-phase holograms. 27

2-3 A liquid crystal display spatial light modulator. Here, the crystal cell display is nematic. 29

2-4 Examples of holograms created to shape light using a liquid crystal device. (a) Field amplitude with an increasing azimuthal index of Laguerre Gaussian beams. (b) Phase-only holograms. (c) Amplitude-phase holograms. 32

2-5 (a) An experimental arrangement to measure the DMD efficiency of the diffracted beam for each state of the micromirrors. Here the lenses L_1 (f = 50 mm) and L_2 (f = 150 mm) magnified and collimated the laser beam by 3× onto the DMD. A pin hole (PH) was used to isolate the first diffraction order. (b) Diffraction patterns obtained at various states (±12°, and 24° alignment), respectively. The diffraction patterns were recorded with a commercial cellphone camera since the pattern was too large to fit on a CCD chip. 34

2-6 (a) An experimental arrangement to generate Laguerre Gaussian (LG) beams. Here the lenses L_1 (f = 50 mm) and L_2 (f = 150 mm) magnified and collimated the laser beam by 3× onto the DMD. (b) A normal amplitude only hologram (left) and a stretched hologram, suitable for the dimensions of the DLP3000 DMD (right). (c) Visibility check of an LG intensity profile, filtered by a pinhole (PH) and observed at the Fourier plane of the second lens of the 4-f system (L_3 and L_4 of f = 150 mm) using a CCD camera. 35

2-7 Simulated OAM modes ($l = 0, 1, 2$, and 3 from left to right) are compared with experimental beams using a correlation method. The correlation method works by comparing the intensities of the experimental results with simulated results. 37

2-8 (a) Two holograms (Holo.1 and Holo.2) combined to form a multiplexed hologram (Multi.), and is displayed at the LC display. (b) Experimental arrangement to measure the conversion efficiency with a multiplexed hologram on a liquid crystal device. Here FL is the Fourier lens of f=150 mm. (c) First-order and zeroth-order results with an increasing grating frequency ($G_x = 20 - 70$ mm^{-1}). (d) Zeroth-order and a multiplexed mode with a grating period of 30 mm^{-1} and an OAM of $\ell = 1$. (e) Results of first-order power with their respective gratings. 39

2-9 (a) A set of two digital holograms merged into a multiplexed hologram. (b) An experimental arrangement to check the fringe visibility of the interferometer using two multiplexed Gaussian beams. (c) Visible fringes produced when the angle of the beam between path A and B are interfered. (d) A curve-fit of the intensity profiles using the interference pattern results. 41

2-10 An illustration of the experimental arrangement. A Helium Neon (He-Ne) laser was expanded and collimated onto a liquid crystal (LC) display. Two modes were generated simultaneously from the SLM and were then separated using a D-shaped mirror (DM) and recombined with a beamsplitter (BS). The recombined modes were imaged to the digital micromirror device (DMD), where the turbulence was encoded in combination with the detection holograms. A polariser (P) was added in-order to change the polarisation states. The resulting modes were propagated to the far field with a 500 mm Fourier lens (FL), where the on-axis intensity measurements were performed. 42

2-11 (a) Superposition of OAM modes. Here we tested modes of OAM subspaces of $\ell = \pm\, 3, 5, 10,$ and 20 (from left to right). (b) Experimentally generated vector beams with superpositions of $\ell = 3$. Here the arrows represent the polarisation states (horizontal, diagonal, vertical, and anti-diagonal) that the OAM mode was projected at a time. 44

2-12 Intensity measurements corresponding to those in table 2.1. Two examples are illustrated, a vector vortex mode (left) and a scalar vortex mode (right). The vector vortex mode exhibits both polarization states and is non-separable, whereas the scalar mode subplot has one polarization component and is separable. 49

2-13 Experimental generation and characterisation of vector modes ranging from completely scalar to (VQF=0) to vector VQF(1). 50

3-1 A pair of sonic anemometers mounted on a rail at building 44, situated at the CSIR. This instrument is discussed in Chapter 1. 55
3-2 Schematic setup for acquiring velocities of the airflow. This experimental arrangement show the electronic components, feeding signal to the sonic anemometer. All this components collect and convert the ultrasonic signal into readable values. 56
3-3 Data acquisition in the sonnet.py module. 57
3-4 Calculated results from real-world measurements. (a) U, V, W wind velocities. (b) Average mean wind velocity. (c) Refractive index structure constant, C_n^2. (d) Coherence length, r_0 values with different propagation distances. 59
3-5 A schematic representation of a turbulence phase screen using the Zernike basis. The phase screen shown here is calculated using the sum of the primary aberrations with their weightings (C_{1-5}). 62
3-6 Phase profiles of turbulence screens generated via Zernike-polynomials. These phase screens are created through the summation of the Zernike polynomial and the weighting coefficients. These phase screens are generated with different D/r_0 values. 62
3-7 Fourier power spectrum phase screens created using random phase screens. These phase screens are generated with different D/r_0 values. 62
3-8 (a) Phase profiles of turbulence screens generated via Zernike-polynomials. These phase screens are created for DMDs. (b) Phase profiles of turbulence screens generated via Zernike-polynomials. These phase screens are created for LC displays and are changing with time. (c) Distorted beam profiles over 800 mm distance. 65
3-9 Simulated Strehl Ratio with 0.5, 1, 2 km propagation distances. . . . 66
3-10 Optical beam characterization setup. 67

3-11 Strehl Ratio versus D/r_0 with different aperture size using the Zernike expansion method. It can be seen that when the aperture size is 0.47 mm, the theory agrees with the measured values because the Gaussian beam size match with the encoded beam waist. 68
3-12 Strehl Ratio versus D/r_0 with different aperture size using Fourier power spectrum method. It can be seen that when the aperture size is 0.47 mm, the theory agrees with the measured values. 69
3-13 Strehl Ratio of a Gaussian beam aberrated by turbulence compared with its theoretical values. Here the propagation distance, L was $<$ 0.5 km. Here the term channel is referred to the number of measured samples. 70
3-14 Strehl Ratio of a Gaussian beam aberrated by turbulence compared with its theoretical values. Here the propagation distance, L was 2 km. The values of the laboratory results (which is the red and blue results) were selected from the red region of Fig. 3-9, which is the theoretical SR for different propagation distances. 71
3-15 (a) An illustration of the experimental setup. A Helium Neon (He-Ne) laser was expanded and collimated onto a spatial light modulator (SLM). Two modes were generated simultaneously from the SLM and were then separated using a D-shaped mirror (DM) and recombined with a beam splitter (BS). The recombined modes were imaged to the digital micromirror device (DMD), where the turbulence was encoded in combination with the detection holograms. The resulting modes were propagated to the DMD's Fourier plane with a 500 mm Fourier lens (L), where the on-axis intensity measurements were performed. . 72
3-16 Pure scalar (Top) and vector vortex (Bottom) intensities propagated through varying turbulence strength. The results show that the intensities vary from turbulence to no turbulence. 74

3-17 Vector Quality Factor measurements with varying D/r_0. The VQF tool measures the components from purely scalar (0) to purely vector (1). 75

3-18 Experimental results for the degree of entanglement (VQF or equivalently concurrence) of the input vector mode vs the output mode under the effect of turbulence strengths of $D/r_0 = 2.5$ (a) and 3.5 (b). The circles are for vector modes in the subspace of $\ell = 1$ and squares are for $\ell = 10$. The Vertical error-bars are smaller than the points. The points were obtained from measurements with 30 realisations of the same turbulence strengths. 76

3-19 Measured modal spectrum for the vertical and horizontal polarised spatial modes. (a, c) and (b, d) were measured for cases when $D/r_0 = 2.5$ (right column) and 3.5 (left column), respectively. The top row was measured for $\ell = 1$ subspace and the bottom row for the $\ell = 10$ subspace. Each bar is an average of 30 realisations of the same turbulence strength. In each plot, the distribution on the right corresponds the horizontally polarised mode (blue) while the distribution on the left (red) corresponds to the vertically polarised mode. As expected, the mode distribution is symmetric about $|\ell|$, consistent with the theoretical distribution shown as lines 77

List of Tables

2.1 Normalized intensity measurements. The symbol $\alpha_1 = 0,\ \alpha_2 = \pi/2,\ \alpha_3 = \pi,$ and $\alpha_4 = 3\pi/2$ are the relative phases for the spatial mode superpositions. 48

3.1 Expressions for the Zernike Polynomials Z_j. Here, $Z_j(\rho, \theta)$ represents $Z_n^m(\rho, \theta)$ [2]. The aberration column indicate the types of aberration with respect to its Zernike polynomial. 60

List of publications

Journal articles

1. M. A. Cox, N. Mphuthi, I. Nape, **N. Mashaba**, L. Cheng and A. Forbes, "Structured Light in Turbulence," in IEEE Journal of Selected Topics in Quantum Electronics, vol. 27, no. 2, pp. 1-21, March-April 2021, Art no. 7500521, doi: 10.1109/JSTQE.2020.3023790.

2. Nape, I., **Mashaba, N.**, Mphuthi, N., Jayakumar, S., Bhattacharya, S., and Forbes, A. (2020). Vector mode decay in atmospheric turbulence: a quantum inspired analysis. arXiv preprint arXiv:2011.14702. Accepted at Physical Review Applied.

Chapter 1

Introduction

Temperature fluctuations, humidity, and air velocity changes contribute to the absorption, scattering, and refractive index (or phase) fluctuations that are experienced by light fields when propagated through the atmosphere. Physically, these characteristics cause deleterious effects such as beam wander, loss of coherence, beam directional fluctuations and irradiance fluctuations, limiting the performance optical systems that are used for communication or imaging purposes. For this reason, studying the behaviour of optical turbulence though statistical models (such as those introduced by Kolmogorov [3]) have played a vital role in understanding how it affects light beams. In particular, careful attention has been given to how it affects the transverse spatial modes of light that are compatible with free-space propagation and therefore the atmosphere.

Transverse spatial modes of light are essential in understanding how optical turbulence distorts the wavefront of light fields. In this chapter, I will give an overview of these transverse modes of light. Next, I will discuss the Kolmogorov's statistical theory of turbulence, as it is well-established and widely-used for studying and characterising turbulence. Furthermore, I will demonstrate the effects of turbulence in optical systems, by simulating the near-field turbulence.

1.1 Background

The Earth's turbulent atmosphere can induce blurring effects on images taken from telescopes or imaging devices located far away from an object plane [4–8]. The blurring arises from refractive index fluctuations that randomly perturb the optical phase of the light [9], resulting in distorted optical wavefronts. As a consequence, the spatial resolution of an optical imaging system, and the range at which a target may be detected, recognised, or identified can be affected. This has adverse effects on the images required for observations made in astronomy [10–12], range finding, and line of sight optical communications [13–15]. For this reason, numerous studies have been conducted to overcome some of these unwanted effects, opening up a broad field of study that focuses on light delivery through the turbulent atmosphere [9, 16–21].

Turbulence is an important question in Physics. Modeling the velocity fields of turbulent flow [22] is amongst the turbulence problems in physics. However, this becomes problematic because the flow becomes non-steady (with many coupled spatial and time scales of variation) and is computationally hard to solve because of its non-linearity. Alternatively, statistical approaches by Kolmogorov and Obukhov [23], permitting us to quantify small scales of turbulence, have shown promise. Scintillometry and point source imaging have been the main techniques for turbulence strength in the field experimentally [24, 25]. However, these techniques are limited in providing a measure of turbulence strength that is integrated over the entire optical path because they only measure turbulence in a fixed position. Atmospheric physics which includes the study of meteorological fields in the surface layer of a turbulent atmosphere shows that ultrasonic equipment can be developed using the Kolmogorov and Obukhov law [26–28].

Several techniques to generate atmospheric aberrations have been studied, including wind channels [29], phase screens [30, 31], moving plates [32], liquid crystal (LC) displays [33, 34] and digital micromirror devices (DMDs) [35]. Moreover, since the time scale at which turbulence changes is given by the Greenwood frequency [36], devices such as DMDs are ideal candidates for real-time simulation purposes: they

have modulation speeds of kilohertz, allowing accurate simulation of fast changing turbulence. In general, all the aforementioned devices are ideal for creating dynamic and deterministic wavefront aberrations for studying turbulence effects on optical beams [35].

This research work described in this dissertation aims to demonstrate the effects of turbulence on optical fields. The results of our work have important implications for atmospheric laser communication systems that employ both classical and quantum encryption. These results can be useful in the design of practical free-space and turbulent quantum communication systems. Firstly, we explore the description of transverse modes of light, mainly spin and orbital angular momentum (OAM) modes. We identify scalar modes, where the amplitude and polarisation components can be treated independently of each other. Subsequently, we focus on vector modes, where the amplitude and polarisation components are not separable (they cannot be treated independently of each other). We study techniques to detect OAM modes by encoding the optical phase of light onto spatial light modulators. Next, we deploy a sonic anemometer to acquire atmospheric data. A sonic anemometer is a solid-state, ultrasonic instrument which measures wind velocity in three orthogonal axes as well as the sonic temperature (T_s). Further detailed are provided in Chapter 3. We extract all the parameters to synthesise phase screens that mimic atmospheric turbulence through the Zernike polynomials and Fourier power spectrum turbulence models. Furthermore, we narrow our interest to vector vortex modes, which exhibit azimuthal symmetry in amplitude, polarisation and we study their resilience against turbulence. Lastly, we build a DMD system that simulates turbulence in real-time (using components from old projector).

1.2 Outline

The structure of this dissertation is as follows:

In Chapter 2 we will review and characterise the techniques used to obtain beams of light with specific characteristics. We will explore two types of spatial modulation,

one based on liquid crystals and the other on digital micromirrors. Lastly, we discuss methods to characterize optical beams through free-space and noisy channels.

In Chapter 3 we demonstrate the installation and operation of an ultrasonic anemometer. This instrument maps the spatio-temporal distribution of fluid velocity in the real-world. Using this data one may determine or calculate the refractive index structure function. We generate real-time turbulence phase screens and we encode them onto the DMD by using the Fourier power spectrum. This experimental testbed in the laboratory allows one to characterize the optical effects caused by turbulence. We employ DMDs to execute a turbulence simulator that is real-time. Furthermore, we generate scalar or vector beams (through the multiplexing method), by loading a computer generated hologram into a liquid crystal display and we detect these modes using a DMD. We demonstrate and characterize the propagation of these optical beams through turbulence and free-space channels. In addition, we describe the importance of studying entanglement using classical light. Through this technique, we investigate the contribution of mode separation on the non-separability of a vector mode state to demonstrate resilience for higher order OAM state spaces.

In Chapter 4 we draw conclusions based on the result obtained and discuss future work.

1.3 Optical modes

The transverse spatial profile, polarisation, and the wavelength of light are properties (degrees of freedom) upon which a myriad of technologies in optical imaging and communication are based on. In this section we explore these properties because they will be crucial in understanding how light fields are affected by optical turbulence in later chapters. We only focus on monochromatic (single wavelength) light fields generated from coherent lasers, focus our attention to the polarisation and transverse spatial modes, and focus some of their interesting properties. Firstly we introduce the polarisation of light, and then introduce the transverse spatial modes of light as solutions to the Helmholtz equations. In particular, we will focus on a special

set of solutions that describes spatial modes that are associated with the orbital angular momentum of light. These modes are attractive for their high information capacity. Lastly, using these two properties, (polarisation and spatial modes), we will introduce a set of modes that are coupled in both degrees of freedom resulting in spatially varying polarisations.

1.3.1 The polarisation of light

Polarisation plays a vital role in optical communications [37–39] and in imaging [40–42]. What does it mean for a light field to be polarised? Firstly, a paraxial optical field is a transverse wave that oscillates perpendicular to the direction of motion. When the electric field oscillation direction is well defined, the light beam is said to be polarised, If not, it is said to be unpolarised. For unpolarised light fields, the oscillations occur in random directions. Examples of polarised light sources can be laser, while light sources like the sun and incandescent light bulbs produce unpolarised light.

In the transverse plane, light fields can be decomposed into two orthogonal components. For example; a light field propagating in the $\boldsymbol{z}$ direction and having a uniform amplitude in the transverse plane can be decomposed into the $\boldsymbol{x}$ (horizontal or H) and $\boldsymbol{y}$ (vertical or V) components on the cartesian plane (see Fig. 1-1). In general such a field can be written as

$$\mathbf{E} = E_{0x}\hat{\mathbf{e}}_H + e^{i\alpha}E_{0y}\hat{\mathbf{e}}_V, \tag{1.1}$$

where E_{0x} and E_{0y} are maximum amplitudes for the $\boldsymbol{x}$ and $\boldsymbol{y}$ directions respectively, while the orthogonal unit vectors

$$\hat{\mathbf{e}}_H = \begin{bmatrix} 1 \\ 0 \end{bmatrix}, \ \hat{\mathbf{e}}_V = \begin{bmatrix} 0 \\ 1 \end{bmatrix}, \tag{1.2}$$

represent the $\boldsymbol{x}$ and $\boldsymbol{y}$ directions, respectively. The vectors are commonly known as horizontal (H) and vertical (V) polarisation states. The complex factor $e^{i\alpha}$ represents

a relative phase (delay) between the two orthogonal components [43]. By changing the amplitudes and phase (α) it is possible to generate arbitrary polarisation states.

For example one can generate the right (R) or left (L) circular states when $\alpha = \pm\pi/2$, resulting in the states

$$\hat{\mathbf{e}}_R = \frac{1}{\sqrt{2}}(\hat{\mathbf{e}}_H + e^{i\pi/2}\hat{\mathbf{e}}_V),\ \hat{\mathbf{e}}_L = \frac{1}{\sqrt{2}}(\hat{\mathbf{e}}_H + e^{-i\pi/2}\hat{\mathbf{e}}_V), \tag{1.3}$$

the rectilinear diagonal (D) and anti-diagonal (A) states for $\alpha = 0$ or $\alpha = \pi$, yielding

$$\hat{\mathbf{e}}_D = \frac{1}{\sqrt{2}}(\hat{\mathbf{e}}_H + \hat{\mathbf{e}}_V),\ \hat{\mathbf{e}}_A = \frac{1}{\sqrt{2}}(\hat{\mathbf{e}}_H + e^{i\pi}\hat{\mathbf{e}}_V), \tag{1.4}$$

respectively. Note that for the circular and rectilinear states $E_{0x,0y} = 1$. For unequal amplitudes, i.e., $E_{0x} > E_{0y}$ or $E_{0x} < E_{0y}$ and $\alpha = (0, \pi/2)$ the polarisation is elliptical with various orientations [43]. A convenient way of parameterising the polarisation states of light is with the Poincare Sphere (PS), depicted in Fig. 1-1, as a unit sphere with various polarisation states located on the surface. Using the PS, we can represent all the polarisation vectors as

$$|\chi\rangle = \cos(\theta/2)\,|R\rangle + e^{i\alpha}\sin(\theta/2)\,|L\rangle \tag{1.5}$$

where the azimuthal angle α determines the orientation of the vector and θ controls the amplitudes. The braket vector notation, $|\cdot\rangle$, is equivalent to the unit vector notation used above. At the poles of the sphere, one finds the circular polarisation states, while the linear polarisation states lie on the equator. Notice that in our description of polarisation modes, we treated the field spatial profile as an independent factor. In the next section we consider the spatial distribution of light and introduce transverse spatial modes.

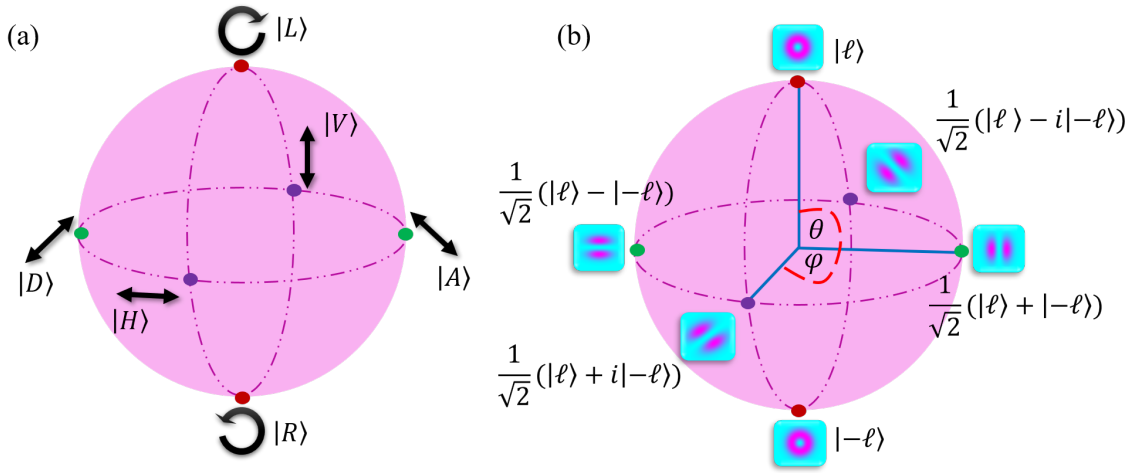


Figure 1-1: (a) A Poincaré Sphere (PS) representation of the polarisation of light. The right $|R\rangle$, and left $|L\rangle$ circular polarisations, the diagonal $|D\rangle$ and anti-diagonal $|A\rangle$, horizontal $|H\rangle$ and vertical $|V\rangle$ polarisation modes. (b) Analogous representation of OAM states in a given subspace $|\ell|$ of a Bloch sphere. The term Bloch sphere refers to a geometrical representation of the pure state space of a two-level mechanical system.

1.3.2 The scalar spatial modes of light

Previously, in describing polarisation states, we assumed a uniform amplitude in the transverse plane. However, in general optical fields can have a variety of spatial profiles, satisfying the Helmholtz equation [44]

$$(\nabla^2 + k^2)U(\mathbf{r}, z) = 0, \tag{1.6}$$

where ∇^2 is the Laplacian operator, k represents the magnitude of the wave-vector and $U(\mathbf{r}, z) = u(\mathbf{r}, z)e^{ikz}$ is the complex field function. Under the paraxial approximation (the limit of small beam divergence in the traverse plane), it can be assumed that $u(\mathbf{r})$ is a slowly varying function of z and therefore the paraxial inequality

$$|\frac{\partial^2}{\partial^2 z}u(\mathbf{r}, z)| << k|\frac{\partial}{\partial z}u(\mathbf{r}, z)|, \tag{1.7}$$

can be satisfied. Subsequently, the Helmholtz equation can be approximated by

$$(\nabla_\perp^2 + ik\frac{\partial}{\partial z})u(\mathbf{r}, z) = 0, \tag{1.8}$$

where $\nabla_\perp^2$ represents the transverse coordinates of the Laplacian. A separable solution of this equation in cylindrical coordinates is

$$U(r, \phi, z) = U(r, z)e^{i\ell\phi}. \tag{1.9}$$

Here ϕ and r are the azimuthal and radial coordinates, ℓ is an azimuthal charge and $U(r, z)$ is the radial profile of the beam.

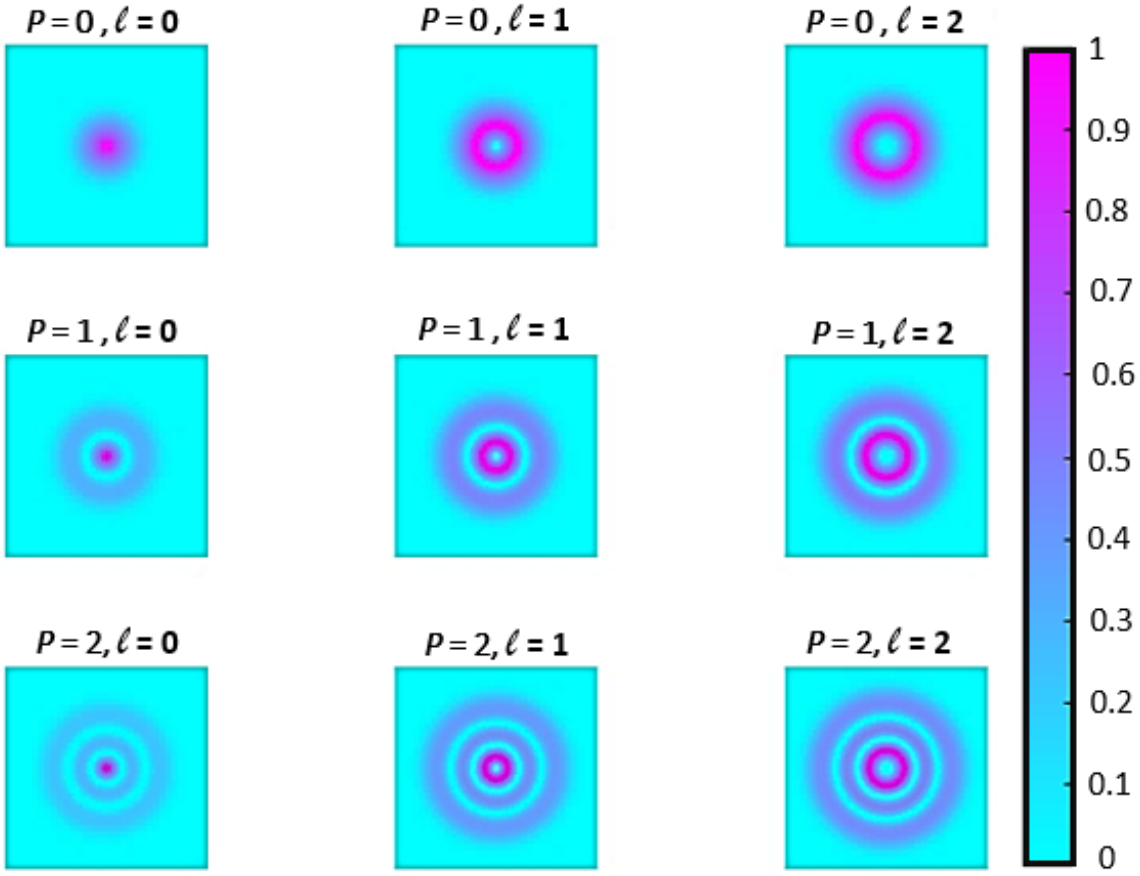


Figure 1-2: The intensities of Laguerre-Gaussian modes. The ℓ index controls the size of the vortex seen as a zero intensity and as a phase singularity. The p index controls the number of concentric radial zero-intensity rings.

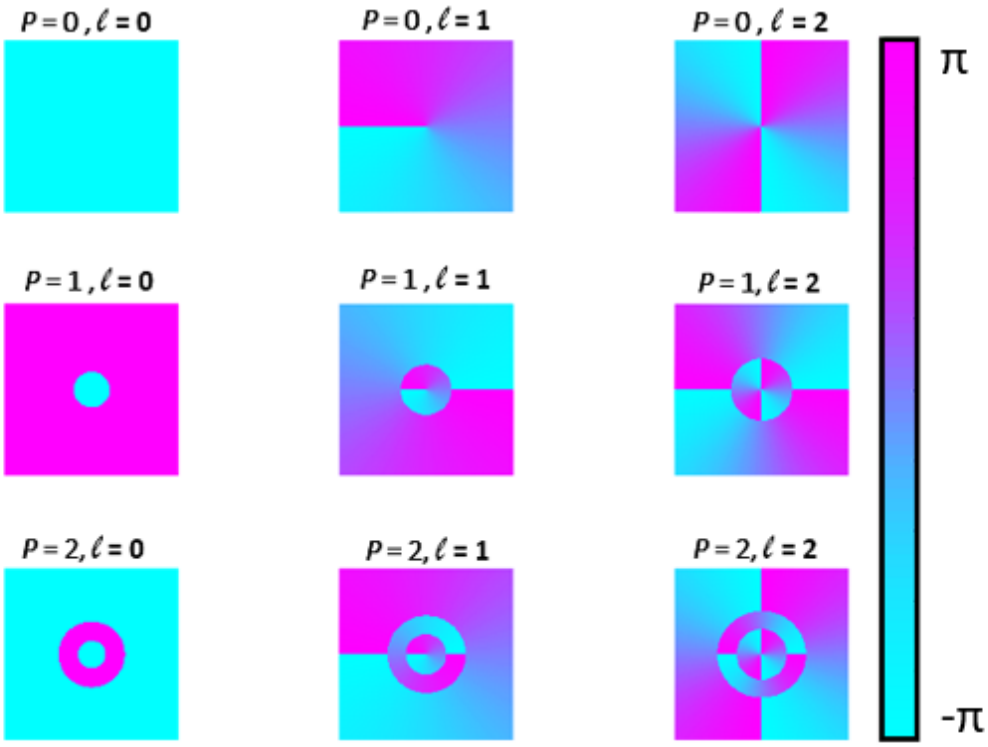


Figure 1-3: Phase maps of Laguerre-Gaussian modes depending on the ℓ and p indices.

In cylindrical coordinates, the solutions are known as the Laguerre-Gaussian (LG) modes, given by

$$LG_{\ell,p} = \sqrt{\frac{2^{|\ell|+1}p!}{\pi(p+|\ell|)!}}\frac{1}{\sqrt{w(z)}}L_{p,l}\left(\frac{2r^2}{w^2(z)}\right)\left(\sqrt{2}\frac{r}{w(z)}\right)^{|\ell|}e^{-\frac{-r^2}{w^2(z)}} \times e^{-ik\frac{r^2 z}{2(z_R^2+z^2)}}e^{i\ell\phi}e^{-i(2p+|\ell|+1)\tan^{-1}(\frac{z}{z_R})}, \tag{1.10}$$

where ℓ, p represents the azimuthal and radial indices, while $L_{p,\ell}(x)$ represents the associated Laguerre polynomials. For $\ell > 0$ one will observe $p+1$ concentric zero-intensity rings around the origin of the beam cross-section with ℓ determining the size of the vortex.

The beam width, $w(z)$, is given by $w_0\sqrt{\frac{z^2+z_R^2}{z_R^2}}$, it is the distance from the axis to a point, along the z axis of the transverse plane, where the intensity of the beam falls to $1/e^2$ of its r-axis and the amplitude falls to $1/e$ of its axial value. Here, w_0 is the

beam waist at $z = 0$, and z_R is the Rayleigh range defined as the distance where the beam area doubles, given by $z_R = \frac{\pi w_0^2}{\lambda}$.

The family that take more fundamental, it is where the radius of curvature is a minimum, the description given in Eq. (1.9). Another family of exotic spatial modes are the Airy beams [45]. In Fig. 1-2 and 1-3 we show a graphical representation of the intensity and phase profiles of several optical beams. These LG beams are intriguing in studying vector modes through turbulence.

1.3.3 Vector modes

In the previous sections, we considered the spatial and polarisation degrees of freedom of optical beams as independent components. Optical beams with spatially varying polarisation states are called vector modes [46]. Owing to their rich structure, vector modes have become a venerable topic of study [47–49] featuring in diverse applications ranging from optical trapping [50, 51], field microscopy, [52] to classical [53, 54] and quantum communication [55–57] because the state of polarisation of a vector mode does not get affected through turbulence. Before we describe what vector modes, are it is essential to first understand what a scalar mode is. In the previous section, we showed that the scalar Helmholtz equation yields scalar solutions. In general, these modes have a homogeneous polarisation state. When we say that the spatial mode is scalar, we mean that the polarisation and spatial components can be written as separable products, i.e.,

$$\mathbf{U}_{scalar}(\mathbf{r}) = u(\mathbf{r}) \cdot \hat{e}_V, \tag{1.11}$$

where the field has a transverse profile given as $u(\mathbf{r})$ and a uniform linear vertical polarisation state $\hat{e}_V$. In practice the polarisation component can be anything (e.g., linear or circular). We see that beams of this form have uniform polarisation states across the transverse plane as illustrated in Fig. 1-4 (a).

In contrast, vector modes have non-uniform polarisation states across the transverse plane. As a result, the electric field has a strong coupling between the polari-

sation and spatial components. To illustrate this, consider a vector mode described by

$$\mathbf{U}_{vector}(\mathbf{r}) = u(\mathbf{r}) \cdot \hat{e}_1 + v(\mathbf{r}) \cdot \hat{e}_2, \tag{1.12}$$

where, $u(\cdot)$ and $v(\cdot)$ are orthogonal spatial modes, and $\hat{e}_{1,2}$ are orthogonal polarisation modes. The field in Eq. (1.12) represents a beam with a spatially non-homogeneous polarisation vector field. A typical example is a radially polarised beam [37]. In the LG basis, it can be written as a superposition of states

$$\mathbf{E}^{+}(\mathbf{r}) = LG_{1,0}(\mathbf{r}) \cdot \hat{e}_R + LG_{-1,0}(\mathbf{r}) \cdot \hat{e}_L, \tag{1.13}$$

where the spatial components are eigenmodes of optical beams that carry OAM. Accordingly, in Eq. (1.13) the right and left circular polarisations are marked with orthogonal OAM modes having topological charges $\ell = \pm 1$, respectively. The intensity and polarisation fields of an LG beam are shown in Fig. 1-4(d), where the field vectors are pointing radially and have rotational symmetry. The direction of the field vectors are determined by the phase, between the terms in the superposition. Other orientations can be obtained by varying this relative phase, e.g, as observed with azimuthally polarised beams shown in Fig. 1-4(e) described as

$$\mathbf{E}^{-}(\mathbf{r}) = LG_{1,0} \cdot \hat{e}_R - LG_{-1,0} \cdot \hat{e}_L. \tag{1.14}$$

Here, the superposition has the same terms as the radial mode in Eq. (1.13) but the relative phase is π. Consequently, the relative phase rotates the polarisation vectors by an angle of $\frac{\pi}{2}$. These two spatial modes are widely produced in optical resonators [58] and naturally generated in step-index and graded-index fibers [59]. Many other vector modes can be generated by simply producing superpositions of scalar modes possessing orthogonal spatial components that have a distinct polarisation.

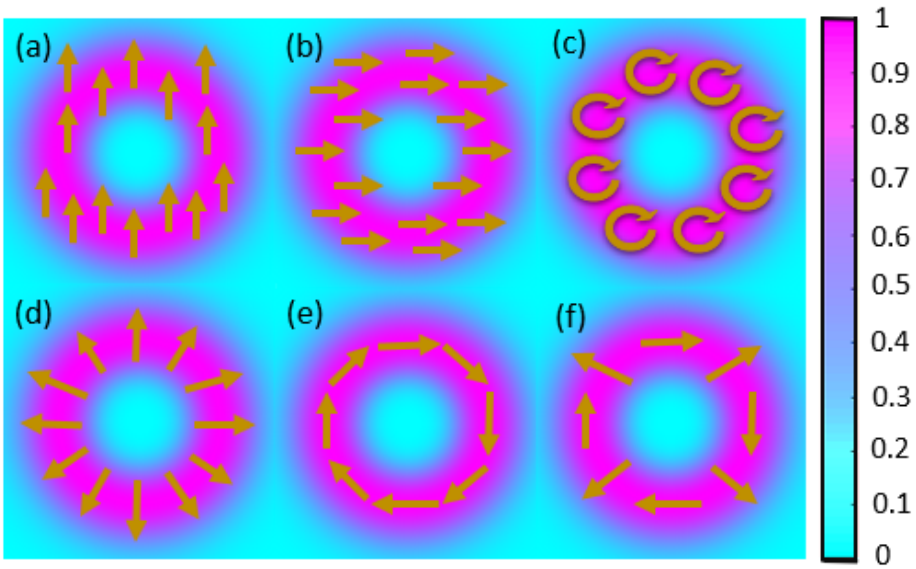


Figure 1-4: The superimposed polarisation and intensity field of a (a)-(c) scalar and a (d)-(e) vector modes. The arrows indicate the vector of the polarisation distribution. This figure will be useful in Chapter 3.

Although scalar and vector modes can be distinguished by their polarisation distributions (uniform or non uniform), a more concrete distinction can be made between them by borrowing tools from quantum mechanics [60], which can quantify the degree of coupling between the polarisation and spatial components. Firstly, an analogy between the separability in the components of the properties of the optical field and quantum states can be made: the state vector of Eq. (1.14) cannot be rewritten as a scalar product of the spatial and polarisation components, i.e., $U_{vector} \neq a_{spatial} \cdot \hat{e}_{polarisation}$, in analogy to an entangled state describing two photons (see ref. [61]). Such vector states have non-separable polarisation and spatial components similar to quantum entanglement and have been used to study the quantum-like features of optical beams [62–65].

1.4 Optical turbulence structure simulation

Transverse modes of light propagating in free-space experience random fluctuations due to fluctuations in the refractive index of the atmosphere (as shown in Fig. 1-5) [9]. These fluctuations are caused by random variations in temperature giving rise to atmospheric turbulence. Atmospheric turbulence is the limiting factor to the deployment of free-space optical communications [66]. The composition of transverse spatial modes, particularly, vortex modes remain unchanged as they propagate in vacuum. In general, the spatial structure (amplitude and phase) of all spatial modes are not maintained when there is atmospheric turbulence along the propagation path [14,67], the modes get distorted. Here we introduce the concept of atmospheric turbulence, resulting in the modes to get distorted and explore some of the statistical tools that are commonly used to model atmospheric turbulence. In particular we focus on the Kolmogorov theory of turbulence. We use this theory to introduce the structure function and structure constant. Lastly, we show how the structure constant can be measured directly using a sonic anemometer.

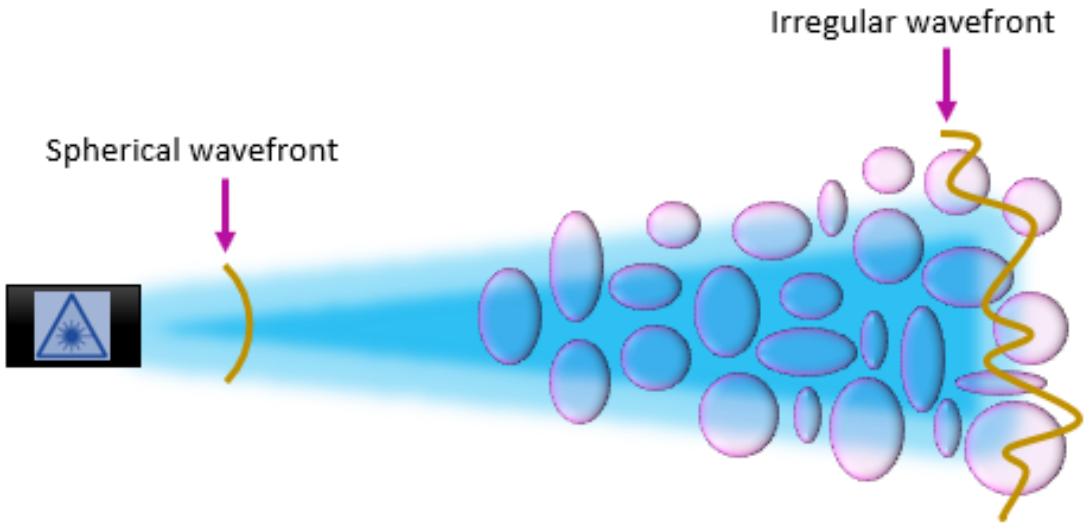


Figure 1-5: Distortion of a spherical wavefront in turbulence (shown as pink ellipse). This result the final wavefront at some distance away from the normal. The laser beam intensity reduces as the beam propagates further due to the obstacles (e.g., turbulence or aerosols).

1.4.1 Turbulent flow

Several studies have shown that the atmosphere can be considered as a viscous fluid with two distinct states of motion, laminar and turbulent [9, 68–71]. The distinction between these motions is that mixing does not occur in steady laminar flow for which the velocity flow characteristics are uniform and parallel. Whereas, in turbulent flow, the velocity field of the airflow becomes different due to dynamic mixing and random displacements caused by the speed of the airflow. A graphical view of the two motions is depicted in Fig. 1-6.

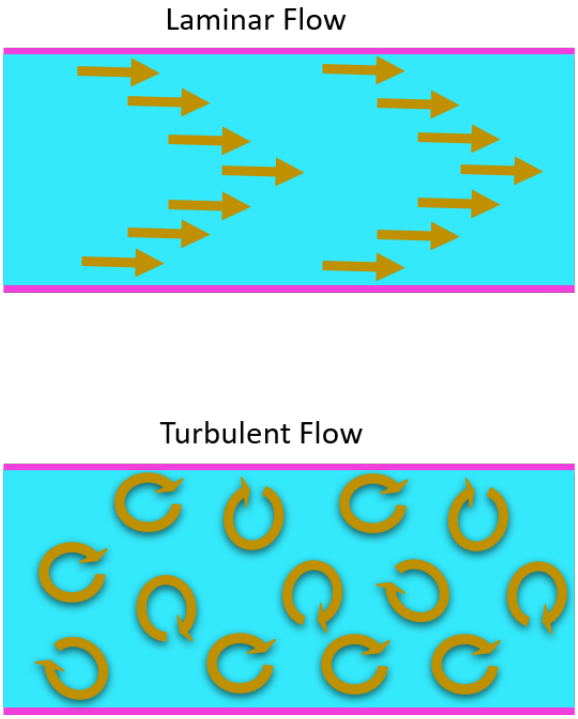


Figure 1-6: Fluid motion; namely, laminar (top) and turbulent (bottom) flow. Here the arrows for laminar flow indicate uniform airflow of the velocity. Whereas the velocity of the airflow (shown as random arrows) for turbulent flow medium indicate random speeds of the liquid.

The change from laminar to turbulent flow can be described by the dimensionless quantity known as the Reynolds number. Over decades, Reynolds developed a similarity theory to define a non-dimensional quantity to characterize the flow. Developed equations that showed the relationship between inertia and viscous flow may be referred as the type of fluid flow in which there is a continuous steady motion of the particles (the velocity at a fixed point always remains constant). Viscous flow theory does have limitations, especially in the high Reynolds number turbulent flow regime. The flow undergoes random fluctuations and is only modeled on a semi-empirical time-mean or statistical basis [9]. Although geometry and fluid buoyancy are critical, the primary controlling parameter is the dimensionless Reynolds number in all viscous flows and it is presented as [72, 73]

$$Re = Vl_d/n, \tag{1.15}$$

where V and l_d are the characteristic velocity (shown as arrows in Fig. 1-6) and one dimensional flow (in metre/second and metre) and n being the kinematic viscosity (in units of m^2/s). The transition from laminar to turbulent flow takes place at a critical Reynolds number, above which the motion is considered turbulent. For laminar flow and turbulent flow, the Reynolds number is $Re < 2300$ and $Re > 4000$.

In the next section Kolmogorov theory, which is respectively a statistical approach to turbulence, will be discussed.

1.4.2 Statistical models of turbulence

In 1941 Kolmogorov and Obukhov developed a statistical model for turbulence, which allows for the computation of statistical quantities that can be simulated and measured in a turbulent system [23]. Kolmogorov's theory of turbulence assumes the atmosphere is homogeneous, isotropic and independent from large scale turbulence. To illustrate this, consider Fig. 1-7, showing how the energy is shoot-up into two turbulent media (the large spatial scales, also known as the outer scale, L_0, as well as the inner scale (l_0)). Both of these effects are deleterious to optical imaging systems. Inner scales distort the wavefront of the light rays, resulting in a randomly aberrated system at the detector plane, while the outer scales causes a propagating beam to be randomly diverted along its path, resulting in image motion, such as beam wander and angle-of-arrival fluctuations at the receiving aperture. These effects cause "image dancing" on an imaging system [74–77]. For example, the accumulative random phase change due to turbulence for a paraxial laser beam of wavenumber, k_0, propagating in vacuum along the z direction and travelling from a source at the plane $z = 0$ is

$$\theta(\mathbf{X}) = k_0 \int_0^L \delta n(\mathbf{x}) dz, \tag{1.16}$$

where $\mathbf{X} = (x, y)$, $\delta_n(\mathbf{x})$ is the refractive index fluctuation at point $\mathbf{x} = (x, y, z)$, and $z = L$ is the distance the light has propagated in the z direction [3]. Understanding the parameter δ_n, is the first step to understanding turbulence. However, δ_n varies rapidly and hence stochastic methods are better suited for its description. These methods are

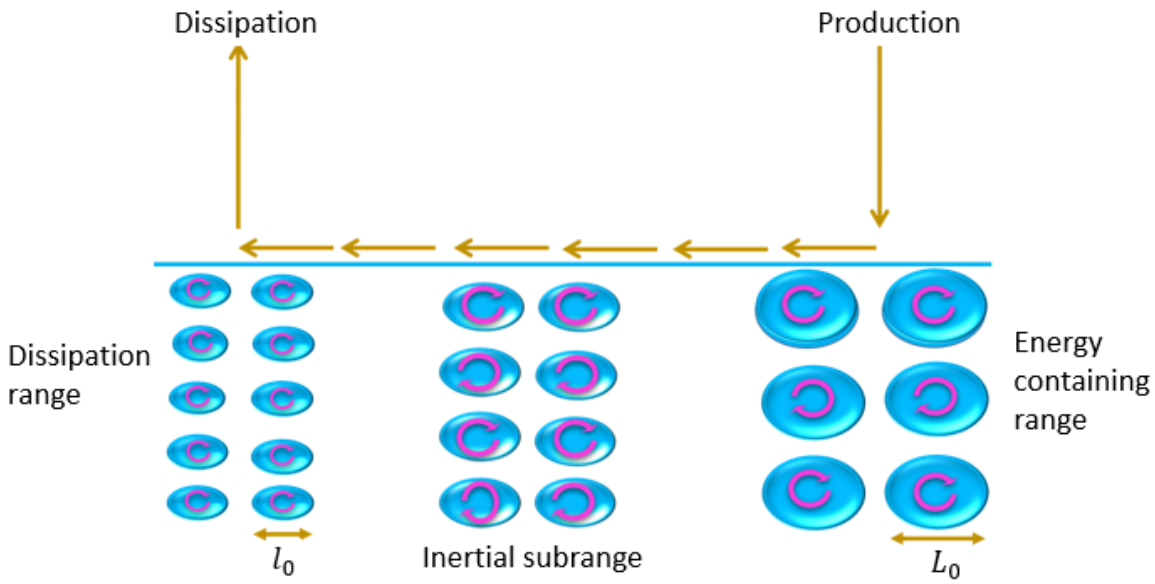


Figure 1-7: Representation of the stages involved in creating turbulent flow. Here, (l_0) and (L_0) are the inner and outer scale of turbulence. Kolmogorov turbulence assumes $l_0 = 0$ and $L_0 = \infty$ which simplifies the model significantly [1].

central to the statistical nature of the model; the variations in the inertial subrange are statistically isotropic. This approach allows structure functions, moments and probability density functions (PDFs) of the refractive index field to be computed. As such, information about the refractive index structure function can be retrieved from the correlation functions. The structure function of the refractive index fluctuations, $D_n(\mathbf{x}_1, \mathbf{x}_2)$, at any point in space can be computed from

$$D_n(\mathbf{x}_1, \mathbf{x}_2) = \langle [\delta n(\mathbf{x}_1) - \delta n(\mathbf{x}_2)]^2 \rangle. \tag{1.17}$$

Accordingly, in the inertial subrange it can be found to be

$$D_n(r) = \begin{cases} C_n^2 l_0^{-4/3} r^2, & 0 \leq r \ll l_0 \\ C_n^2 r^{2/3}, & l_0 \ll r \ll L_0, \end{cases} \tag{1.18}$$

where r is the spatial scale between two points given by, $|\vec{r_1} - \vec{r_2}|$. The symbol, C_n^2 is the refractive index structure parameter, measured in $\mathrm{m}^{-2/3}$, and is given by

$$C_n^2 = (79 \times 10^{-6} \frac{P}{T_a^2})^2 C_T^2. \tag{1.19}$$

Here P is the pressure in millibars, T_a is the absolute temperature in Kelvin, and C_T^2 is the temperature power spectrum which characterizes the size of the fluctuations as a function of temperature. The C_n^2 estimates the strength of optical turbulence and this constant is considered important when characterizing atmospheric turbulence. Typical values of C_n^2 vary from $10^{-17}\mathrm{m}^{-2/3}$ in "weak" turbulence up to approximately $10^{-13}\mathrm{m}^{-2/3}$ in "strong" turbulence [9]. The refractive index auto-correlation function is related to D_n by [78]

$$\langle \delta n(\mathbf{x}_1) \delta n(\mathbf{x}_2) \rangle = \langle \delta^2 n(0) \rangle - \frac{1}{2} D_n(r). \tag{1.20}$$

The auto-correlation function depends only on the difference between the coordinates, according to the assumptions of the homogeneity and isotropy. This means $\langle \delta n(\mathbf{x}_1) \delta n(\mathbf{x}_2) \rangle = \langle \delta n(0) \delta n(\mathbf{x}_2 - \mathbf{x}_1) \rangle$. Moreover, using the Wiener–Khinchin theorem (which states that the auto-correlation function of a wide-sense-stationary random process has a spectral decomposition given by the power spectrum of that process), the power spectral density (PSD) of the refractive index fluctuation, $\Phi_n(\mathbf{k})$, is the Fourier transform of this auto-correlation function [79],

$$\Phi_n(\mathbf{k}) = \mathcal{F}\{\langle \delta n(0) \delta n(\mathbf{x}) \rangle\}(\mathbf{k}), \tag{1.21}$$

where $\mathbf{k}$ is the three-dimensional wavevector. If we assume the turbulence is Markovian (a stochastic model used to model randomly changing systems). $\Phi_n(\mathbf{k})$ is a measure of the statistical distribution of the abundance and size of the turbulent eddies. By combining equations 1.18 and 1.21, the Kolmogorov refractive index PSD becomes

$$\Phi_n(\mathbf{k}) = 0.033 C_n^2 |\mathbf{k}|^{-11/3}. \tag{1.22}$$

The power spectral density of the refractive index fluctuations shows a relationship to the refractive index structure function, C_n^2.

There are a number of turbulence power spectrum models with increasing complexity, for example the Hill power spectrum (which has no analytical solution), the Tatarskii power spectrum, and the von Kármán (vK) power spectrum, which can be written as [9]

$$\Phi_n^{vK}(\kappa, l_0, L_0) = 0.033 C_n^2 \frac{\exp\left(-\kappa^2/k_m^2\right)}{(\kappa^2 + k_0^2)^{11/6}} \quad \text{for} \quad 0 \leq \kappa < \infty, \tag{1.23}$$

where $\kappa = 2\pi(f_x \cdot \hat{x} + f_y \cdot \hat{y})$ is the angular spatial frequency vector, the subscript vK denotes von Kármán, $k_m = 5.92/l_0$, and $k_0 = 2\pi/L_0$. A popular power spectrum is the Modified Atmospheric Spectrum, and builds from the von Kármán and Hill (vKH) spectrums:

$$\begin{aligned} \Phi_n^{vKH}(\kappa, l_0, L_0) = 0.033 C_n^2 \Bigg[1 + 1.802 \left(\frac{\kappa}{k_l}\right) \\ -0.254 \left(\frac{\kappa}{k_l}\right)^{7/6} \Bigg] \frac{\exp\left(-\kappa^2/k_l^2\right)}{(\kappa^2 + k_0^2)^{11/6}} \quad \text{for} \quad 0 \leq \kappa < \infty, \end{aligned} \tag{1.24}$$

where $k_l = 3.3/l_0$ and the subscript vKH denotes von Kármán and and Hill. We choose these power spectrums to generate individual phase screens of turbulence with appropriate statistics [80] in Chapter 3.

The Fried parameter, r_0, commonly known as the atmospheric coherence length, is a useful alternative to C_n^2. The coherence length for a plane wave (approximately a collimated Gaussian beam) in Kolmogorov turbulence is given by

$$r_0 = 1.68 \left(C_n^2 L k^2\right)^{-3/5}. \tag{1.25}$$

while in an unspecified coherence length (r_0), turbulence is given by

$$r_0 = \left(0.423 k^2 \int_0^L C_n^2(z) dz\right)^{-3/5}. \tag{1.26}$$

The atmospheric coherence length is the radius after which the atmospheric turbulence becomes uncorrelated. For example, two beams separated by at least r_0 will experience uncorrelated, independent distortion.

A common parameter to specify turbulence strength is the Strehl Ratio (SR), defined as the ratio of the on-axis intensity in the presence of atmospheric turbulence to the on-axis intensity of the turbulence. The Strehl Ratio of an optical system for a plane wave in Kolmogorov turbulence is given by

$$\mathrm{SR} = \frac{I(0)}{I_0(0)} \approx \frac{1}{[1 + (D/r_0)^{5/3}]^{6/5}}, \tag{1.27}$$

where $I(0)$ and $I_0(0)$ are the on-axis intensities with and without turbulence. D is the aperture diameter. Turbulence leads to scintillation, beam wandering and other effects, resulting the on-axis beam intensity, $I(0)$, reduced on average.

We shall simulate turbulence numerically in Chapter 3. We extend the theory in propagating optical beams in turbulence by multiplying the input beam with turbulence phase screens. The phase screen model is most popular for simulating beam propagation in a turbulent medium. The phase screen model takes into account phase modulations, as the beam propagates in space. Figure 1-8 shows a Gaussian beam, propagating through a series of turbulence phase screens, demonstrating that the output beam is distorted. In addition, we discuss the extraction of turbulence parameters from a sonic anemometer.

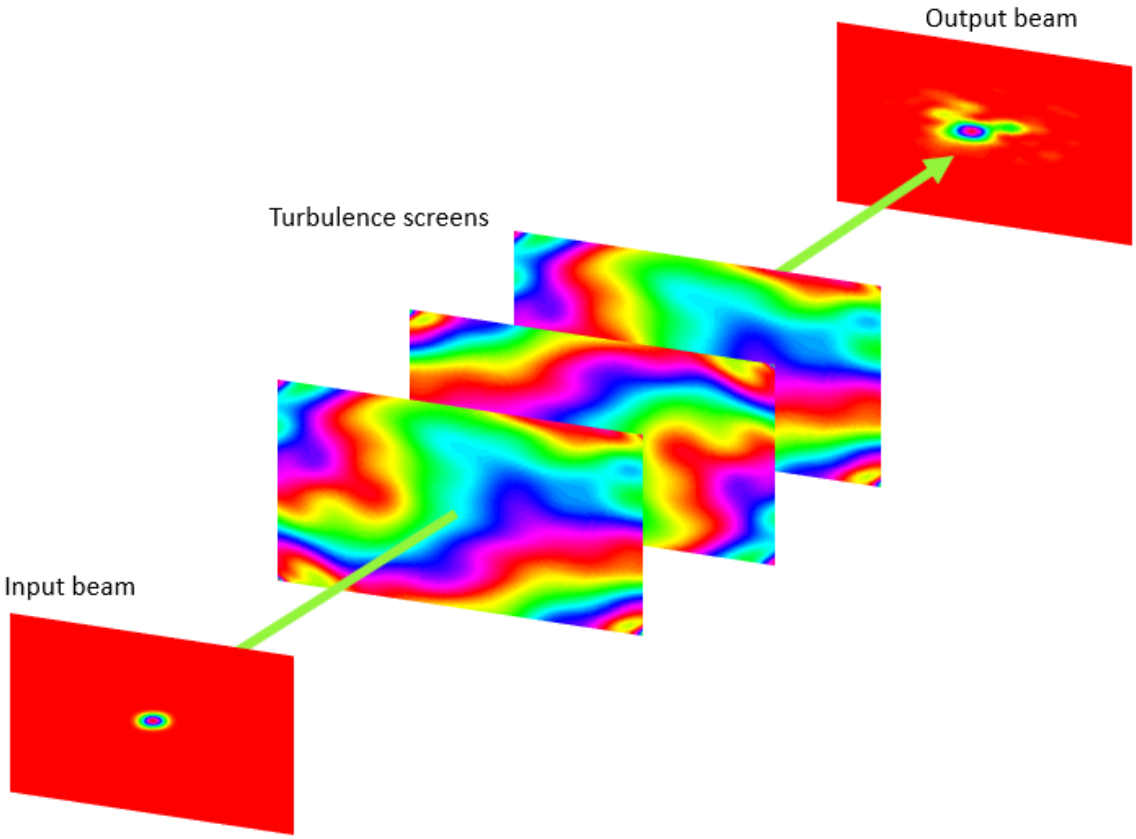


Figure 1-8: Free-space propagation of an optical beam through a turbulent medium. Here the Gaussian beam is propagated through random turbulence phase screens and the final wavefront gets distorted.

1.4.3 Sonic anemometer

Turbulence near the input aperture of an imaging system ("near-field" turbulence) is particularly detrimental to the image quality. Scintillometry and point source imaging have been the main optical techniques to measure turbulence strength [81–83]. However, these techniques are limited to providing local measures of turbulence. Here we review a technique called sonic anemometry, commonly studied by atmospheric researchers to analyse small volumes of turbulence in the near-field [84–87]. To do this, we first review the principles of a sonic anemometer, and subsequently show how to extract the parameters necessary to calculate turbulence from this instrument. A sonic anemometer is a solid-state ultrasonic instrument having the ability to measure wind velocities in three orthogonal axes (U, V, and W) and supplies sonic temperature

[87]. The instrument consists of three pairs of transducers that are orthogonal to one another. Each pair of transducers act alternately in the transmitting and receiving mode, sending ultrasonic pulses between the pair. Figure 1-9 shows the layout of the instrument head. The vertical stiffener member is used as a reference against which to place a spirit level in order to align the instrument head.

Sonic anemometers have made the task of compensating turbulence on imaging systems much easier, by acquiring turbulence parameters for near-field and inputting them into the optical elements design. In the last chapter we deploy a sonic anemometer to acquire velocity data of the airflow outside a field optical test facility and we calculate turbulence phase screens from it.

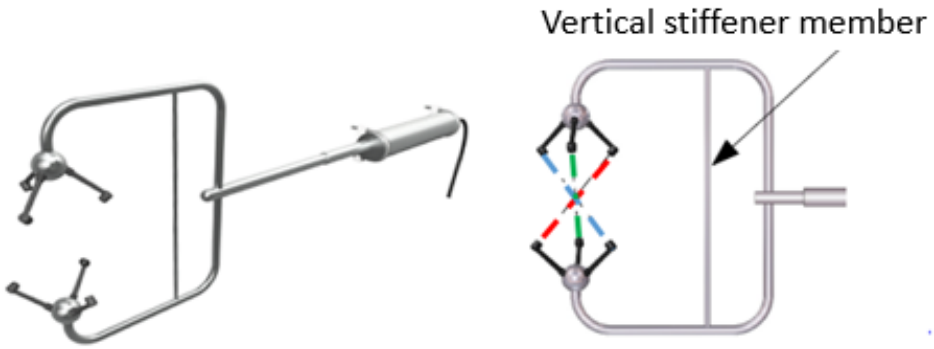


Figure 1-9: Two views of a sonic anemometer transducer, dotted lines show transducer pairs. The angle between these three transducers is 60 degrees, which means that no ultrasonic pulse can interfere with the other. The U, V, and W component represent the "red", "green", and "blue" colours.

Extraction of velocities from a sonic anemometer

A sonic anemometer measures the velocity of the airflow at a fixed position in space. The instrument uses ultrasonic pulses to measure the airflow.

Figure 1-10 shows an example of a pair of transducers, sending and receiving pulses to one another. The transducers are separated by distance d, and the travelling time for each pulse is measured (t_1 and t_2). By measuring the times of flight of each ultrasonic pulse (from either U, V, or W vector component) along the path, the velocity of the airflow from the three components (U, V, or W) can be calculated

separately and simultaneously using,

$$v = \frac{d}{2}\left(\frac{1}{t_1} - \frac{1}{t_2}\right). \tag{1.28}$$

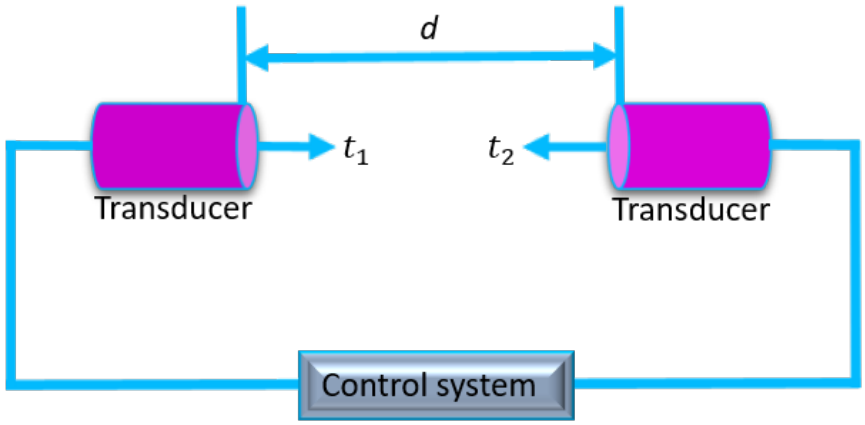


Figure 1-10: Time of flight mechanism. The transducers are separated by distance, d. The symbol t_1 and t_2 are the travelling times for each sonic pulse.

Most sonic anemometers measure the sonic temperature (the temperature measured by the sonic anemometer's thermometer) through [88]

$$T_s = \frac{d^2}{1612}\left(\frac{1}{t_1} + \frac{1}{t_2}\right) + \frac{1}{403}(v_U^2 + v_V^2), \tag{1.29}$$

where d is the distance between the transducers, and $v_U^2 + v_V^2$ are the velocities of the U and V vector components. From sonic temperature measurements, one can estimate turbulence. The intermediate to which this is strongly related is the temperature structure function constant, C_T^2, and is given by [89]

$$C_T^2 = \frac{1}{n}\sum_{i=2}^{n} \frac{(T_{s(i)} - T_{s(i-1)})^2}{\frac{v_{s(i)} + v_{s(i-1)}}{f_{samp}}}, \tag{1.30}$$

where f_{samp} is the sampling frequency. v_s and T_s are the wind speeds and sonic temperature for measurement i and n is the number of raw measurements [89]. In optical terms, the most common measure of turbulence strength is the refractive index structure function constant C_n^2.

Chapter 2

Experimental techniques

Much of the work described in this dissertation involves controlling the amplitude and the phase of light. I want to achieve this in a binary fashion and therefore employ techniques developed by the beam shaping community. Currently the most convenient way to control light is with holographic filters that imprint the desired phase and amplitude via spatially structured gratings. In this chapter I will discuss the use of these devices, and show some of the standard techniques. Next, we test the performance of the spatial modulators using optical beams. We explore characteristics that are important for optical pattern recognition, such as image correlation and visibility. We compare simulated optical beams with experimental ones. Furthermore, we generate vector modes using SLMs via a multiplexing approach in an interferometer. Lastly, we introduce the vector quality factor (VQF), for characterising vector beams. The VQF technique is useful in showing the disparity between purely scalar and purely vector beams. These tools will become crucial in Chapter 3. We will use them to generate and characterize vector beams in turbulence.

2.1 Controlling the phase and amplitude of light with digital devices

A spatial light modulator (SLM) is a pixelated display screen with individually-addressed micron-sized mirrors or liquid crystals. Spatial light modulators offer a simple, fast and digital approach to controlling the amplitude, polarization, and phase of light. Depending on the characteristics of the display and using a relevant hologram preparation procedure, specific field profiles can be encoded on light beams. In this section we will explore SLM technologies that use digital micromirror devices (DMDs) and liquid crystal (LC) cells.

2.1.1 Generation of digital holograms with an amplitude-only device

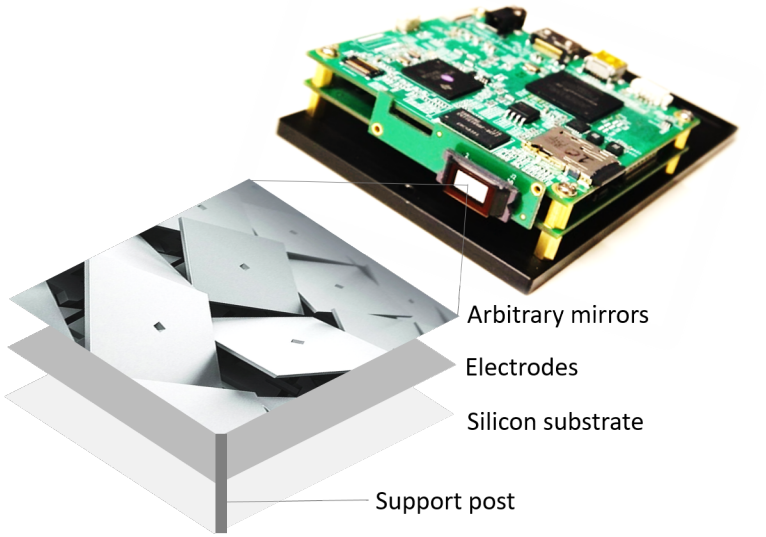


Figure 2-1: A digital micromirror device (DMD) display. The DMD is made up of micromirrors and can be controlled in a binary fashion (the micromirrors can be set to +12 degrees and -12 degrees from its normal), using DLP Lightcrafter software.

A digital micromirror device (DMD) is a device that can only modulate the amplitude of a beam (see Fig. 2-1). Given this limitation, the modulation technique must be tailored to alter both the amplitude and phase of the beam.

To achieve this, a technique was applied to achieve both amplitude and phase control via binarised holograms [90–92]. We will outline this technique here.

Firstly, consider a binarised amplitude grating with a transmission function given by [91]

$$T(x) = \sum_{m=-\infty}^{\infty} \text{rect}\left[\frac{x-(m+p)x_0}{wx_0}\right], \tag{2.1}$$

where the function $\text{rect}(x) = \begin{cases} 1 & |x| \leq \frac{1}{2} \\ 0 & \text{otherwise} \end{cases}$, x_0 defines the amplitude of the function rect with parameters p and w controlling the position and width of each contributing profile and resulting in a uniform grating. By judiciously selecting these parameters it is possible to construct a binary grating that imparts the desired phase and amplitude information onto an optical beam.

The transmission function $T(x)$ is periodic and can therefore be expanded as a Fourier series following

$$T(x) = \sum_{m=-\infty}^{\infty} T_m e^{i\frac{2x}{x_0}}, \tag{2.2}$$

where m indexes the contributing harmonics and T_m are the complex coefficients that depend on w and p (width and position),

$$T_m(x) = \frac{\sin\left[\pi m w(x)\right]}{\pi m} e^{i2\pi m p(x)}. \tag{2.3}$$

Assuming that p and w are dependent on x and observing the first order expansion, we obtain

$$T_1(x) = \frac{\sin\left(\pi w(x)\right)}{\pi} e^{i2\pi p(x)}. \tag{2.4}$$

The mode $T_1(x)$ in this form is a product of an amplitude and phase. As such, the function $w(x)$ can be interpreted as relating to the amplitude while $p(x)$ is related to

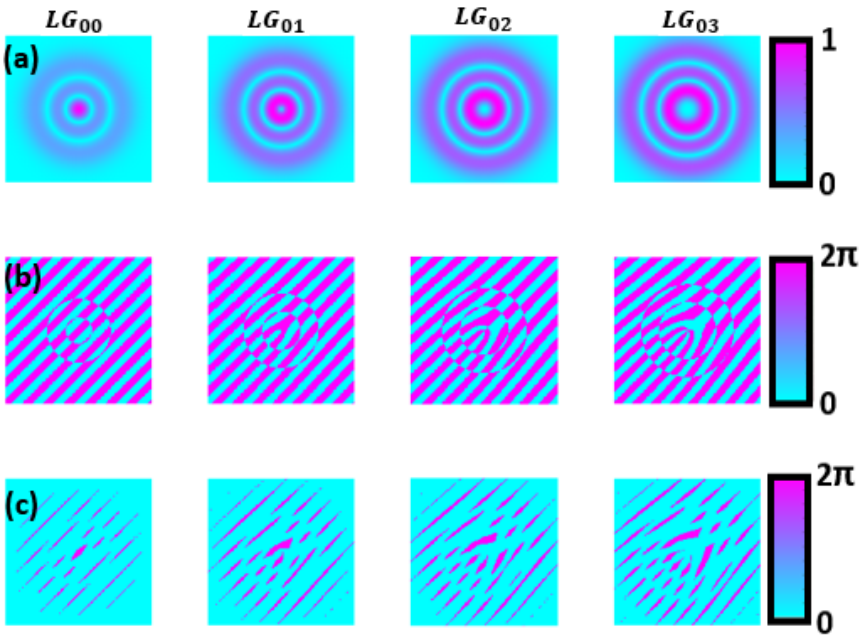


Figure 2-2: Examples of holograms created to shape light using a digital micromirror device. (a) Field amplitude with an increasing azimuthal index of Laguerre Gaussian (LG) beams. (b) Binary phase holograms. (c) Binary amplitude-phase holograms.

the phase. The analysis above is presented for one dimension; in two dimensions it can be shown that the hologram will take the form

$$T(x,y) = \frac{1}{2}\left\{1 + \text{sgn}\left(\cos\left(2\pi\frac{x}{x_0} + \pi p(x,y)\right) - \cos\left(\pi w(x,y)\right)\right)\right\}, \tag{2.5}$$

where the function, $\text{sgn}(x) = \begin{cases} 1 & if \quad x > 0, \\ 0 & if \quad x = 0, \\ -1 & if \quad x < 0 \end{cases}$. Given a desired field function of the form $U(x,y) = A(x,y)e^{i\phi(x,y)}$, we can show that [91],

$$\begin{aligned} w(x,y) &= \frac{1}{\pi}\text{arcsin}(A(x,y)), \\ p(x,y) &= \frac{1}{\pi}\phi(x,y). \end{aligned} \tag{2.6}$$

We have assumed that the field contains no singularity and thus its amplitude can

be normalized to have a maximum of unity (Note that the factor π in the argument of arcsin is dropped since the maximum amplitude is normalized to unity). We have designed two-dimensional binary amplitude holograms to generate Laguerre-Gaussian (LG) modes. Figure 2-2 shows sampled holograms (binary phase and binary amplitude) designed for the generation of vortex OAM and LG modes using a DMD. The blazed gratings chosen to create these vortex modes have a fairly uniform width across their aperture, whereas, for the case of LG modes the blazed grating gradually disappears where the amplitude gets negligibly smaller.

In this section, we have created various two-dimensional binary amplitude and phase holograms using a digital micromirror device. In the next section, we explore a phase-only device and a different technique to create holograms.

2.1.2 Generation of holograms with liquid crystal displays

Among the various devices that can be used to tailor the amplitude, phase or polarisation of light, liquid crystal displays are widely used [93–95].

The technology is based on manipulating the orientation of the liquid crystals situated in each pixel of the display. Each of these pixels can be controlled independently to achieve the relevant phase transfer to an optical beam. Phases transfers as large as 2π, 4π or 8π can be achieved. The phase function of a desired light field is encoded as a grey level image that is loaded on the LC display.

SLMs are pixelated displays consisting of a multitude of individual micron-sized liquid crystals. The angle of the liquid crystals inside the cells are electrically adjusted with an applied voltage. The voltage alters the orientation of the crystals resulting in a phase shift that is proportional to the magnitude of the field. The crystals are birefringent and modulate only the horizontal axis of the incoming beam.

Liquid crystal displays

Liquid crystals are composed of organic molecules that exist at the interface between liquid and solid phase states. They have elongated rod-like structures whose orientation can be affected by thermal, mechanical, and electrical stimuli. Depending on their orientation, they can classified as nematic (randomly oriented), smectic (ordered in position), and cholesteric (helical twisted arrangement which are sometimes referred to as twisted nematic crystals). The nematic (shown in Fig. 2-3) and smectic type differ in the ordering of the crystals; however, in both instances the crystals are aligned in one direction. By contrast, the cholesteric crystals possess a helical orientation that is associated with a rotation angle and have stronger binding forces to avoid separation.

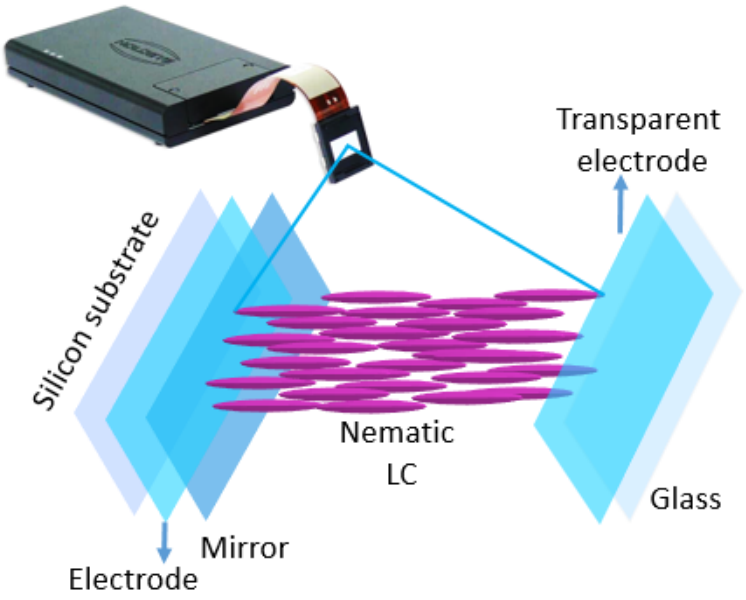


Figure 2-3: A liquid crystal display spatial light modulator. Here, the crystal cell display is nematic.

Most displays make use of nematic crystals cells in which the crystals are addressed by means of an electrical field, controlling the orientation and alignment of the crystals. The alignment of the crystals can be classified as vertically aligned nematic (VAN), parallel aligned nematic (PAN) and twisted nematic (TN), which depend on the kind of display used. The displays can either be transmissive or reflective. The

transmissive variety use transparent liquid crystals while the reflective variety have a silicon substrate, hence called Liquid Crystal On Silicon (LCOS).

The VAN and PAN displays have the liquid crystals sandwiched between a silicon substrate and a transparent electrode for controlling the crystal orientation, which is proportional to the applied voltage. Moreover, the crystals line up according to the strength of applied voltage. The phase shift for each pixel of the liquid crystal display is given by

$$\Delta\chi = \frac{2\pi}{\lambda} nL, \tag{2.7}$$

where n is the refractive index and L is the thickness of the cell. Importantly, the anisotropic crystalline structure makes the liquid crystals in each pixel birefringent and allow modulation to happen. Consequently, the refractive index is larger in the slow axis than in the fast horizontal axis because of the material's density. As such, the phase velocity is larger in one direction upon traversing the crystal.

Amplitude and phase modulation of optical beams with phase-only spatial light modulators

Customizing optical fields requires control of both the amplitude and the phase of a beam. Here we explore how both modulation techniques can be achieved using a phase only device.

Suppose we have an optical field profile given as

$$U(x, y) = a(x, y)e^{i\phi(x,y)}, \tag{2.8}$$

where $a(x, y)$ is the amplitude and $\phi\,(x, y)$ is the phase. The aim is to encode the field function $U(\cdot)$ onto an incoming beam, preferably a plane wave. How do we achieve this with phase only modulation? Here we employ an approach derived by Arrizon [96–98]. Other methods which use similar approaches have also been proposed [99, 100].

The final hologram is expected to take the form

$$H(x,y) = e^{i\psi(a,\phi)}, \tag{2.9}$$

The function $\psi(a,\phi)$ is the phase modulation encoding both the amplitude (a) and phase information (ϕ) of $U(x,y)$ in Eq. (2.8).

By first considering the Fourier expansion of the modulation function $H(x,y)$

$$H(x,y) = \sum_q c_q^a e^{iq\phi}, \tag{2.10}$$

where the coefficients c_q^a can be computed from

$$c_q^a = \frac{1}{2\pi}\int_{-\pi}^{\pi} e^{i\psi(a,\phi)}\ e^{iq\phi}\ d\phi, \tag{2.11}$$

for each q^{th} harmonic in the Fourier series [91]. The first order harmonic gives the relevant phase modulation if $c_1^a = Aa$. Using this condition we find that the imaginary and real parts of c_1^a must satisfy

$$\int_{-\pi}^{\pi} \sin\left(\psi(a,\phi) - \phi\right)\ d\phi = 0, \tag{2.12}$$

$$\int_{-\pi}^{\pi} \cos\left(\psi(a,\phi) - \phi\right)\ d\phi = 2\pi Aa. \tag{2.13}$$

The conditions above imply that $\psi(a,\phi)$ must be selected from a class of functions with odd symmetry.

One such class can be chosen as

$$\psi(a,\phi) = f(a)\sin(\phi), \tag{2.14}$$

with $f(a)$ satisfying

$$J_1\left[f(a)\right] = Aa, \tag{2.15}$$

where $J_1[\cdot]$ is the Bessel function of the first kind [101]. Accordingly, the function $f(a)$ is obtained from the numerical transform inversion of $J_1[f(a)]$. The minimum value for A is 0.5319, corresponding to the maximum value of the first order Bessel function $J_1[x]$ occurring when $x \cong 1.84$.

The creation of vortex beams can be accomplished by encoding an azimuthal variation modulus 2π and a blazed grating to separate the first order from the other orders, taking the form

$$\Phi(\rho, \varphi) = \text{mod}[l\varphi + 2\pi(G_x x + G_y y), 2\pi], \tag{2.16}$$

where mod is the modulus function, G_x and G_y are the grating frequencies along the x and y directions respectively. Figure 2-4 shows the phase and intensity profiles created for a phase-only device.

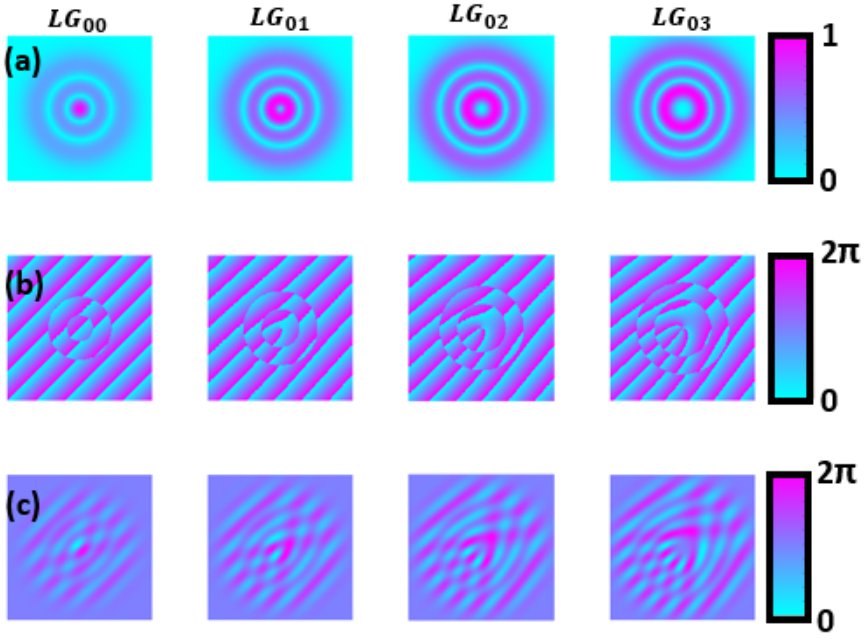


Figure 2-4: Examples of holograms created to shape light using a liquid crystal device. (a) Field amplitude with an increasing azimuthal index of Laguerre Gaussian beams. (b) Phase-only holograms. (c) Amplitude-phase holograms.

In this section we have designed holograms suitable for LC displays. We have simulated intensity profiles for different LG modes. In the next section, we characterize spatial light modulators to test their optical performance using optical beams (written

as holograms on the SLM).

2.2 Characterising digital devices

We have introduced two methods for generating spatial modes using digital displays namely, DMDs and phase-only liquid crystal SLMs. As shown, these devices possess the ability to modulate the phase and amplitude of light in a controllable fashion. These tools will become crucial for generating vector modes and for simulating optical turbulence in the lab environment. However, to achieve this, we first characterise the devices. We will explore the operation of the DMD and measure its conversion efficiency. We will generate diffraction gratings on liquid crystal devices and characterise them with the aim of generating multiplex beams for the purpose of using them to generate vector beams.

2.2.1 Digital micromirror characterization

In our work we used a DLP3000 DMD, purchased from Texas Instruments. This device consists of square shaped micromirrors of 7.5 μm length and a resolution of 608×684 pixels. Unlike the liquid crystal displays that only have a refresh-rate of several tens of Hertz, the refresh rate of this device is approximately 4 kHz. The mirrors are designed to tilt in a binary fashion by setting the deflection angle of each individual mirror to $\pm 12°$. Here, we measured the efficiency of three different states (ON-state, OFF-state and 24° alignment). The ON-state refers to when the micromirrors are rotated $+12°$ from their normal whereas, the OFF-state refers to when the deflection angle between the micromirros and normal is $-12°$. The 24° alignment angle is regarded as the most efficient, according to the supplier's manual. The 24° alignment is the angle that the incoming laser beam hit the surface of the DMD. This angle can be achieved when you set the DMD to the OFF-state mode and then reflect the beam (with the DMD) to the incoming laser beam. Once this is set, the 24° angle will appear if you turn the mirrors to the ON-state mode.

The percentage efficiency of a diffracted order from the DMD without a holographic grating can be computed by

$$\text{Efficiency} = \frac{I_{out}}{I_{in}} \times 100, \tag{2.17}$$

where I_{out} and I_{in} are the intensities measured from a desirable order and the incident beam. We experimentally measured these efficiencies using Fig. 2-5 (a), where a plane wavefront of a helium neon laser is illuminated at the DMD. The beam gets diffracted by the pixelated device and each order is detected at the power meter, the diffracted beam is shown in Fig. 2-5 (b).

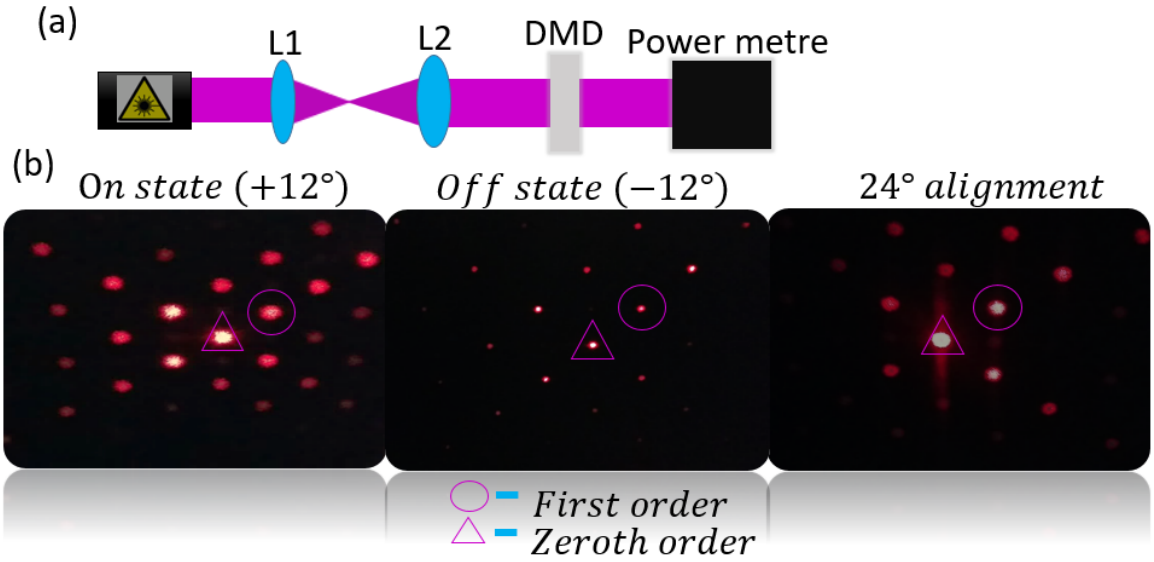


Figure 2-5: (a) An experimental arrangement to measure the DMD efficiency of the diffracted beam for each state of the micromirrors. Here the lenses L_1 (f = 50 mm) and L_2 (f = 150 mm) magnified and collimated the laser beam by 3× onto the DMD. A pin hole (PH) was used to isolate the first diffraction order. (b) Diffraction patterns obtained at various states (±12°, and 24° alignment), respectively. The diffraction patterns were recorded with a commercial cellphone camera since the pattern was too large to fit on a CCD chip.

Figure 2-5 (b) shows the results from three different states. We are mainly interested in the diffracted order (first-order) in which the modulated mode from the DMD is displayed. Here the first-order diffraction beam refers to the first principal maxima from the zeroth-order. When the mirrors are set to the OFF-state (−12°), more than

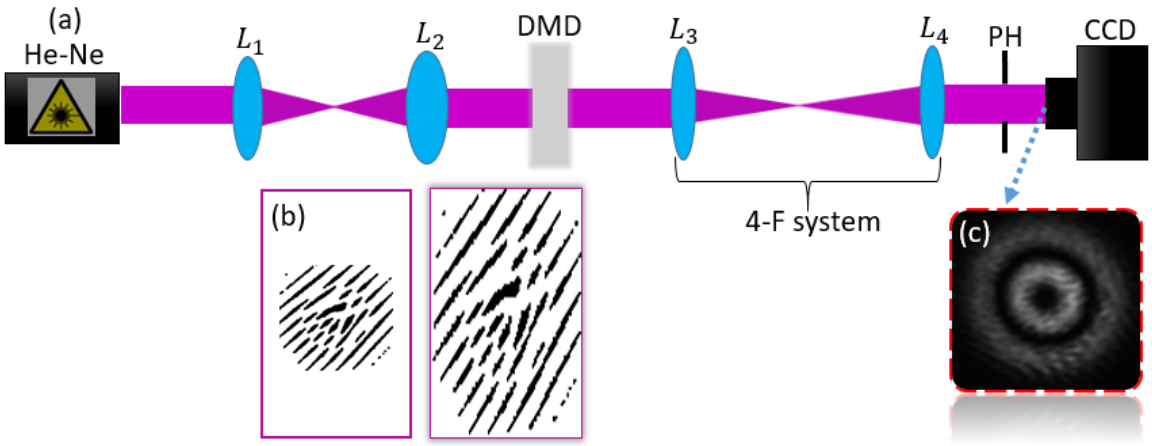


Figure 2-6: (a) An experimental arrangement to generate Laguerre Gaussian (LG) beams. Here the lenses L_1 (f = 50 mm) and L_2 (f = 150 mm) magnified and collimated the laser beam by 3× onto the DMD. (b) A normal amplitude only hologram (left) and a stretched hologram, suitable for the dimensions of the DLP3000 DMD (right). (c) Visibility check of an LG intensity profile, filtered by a pinhole (PH) and observed at the Fourier plane of the second lens of the 4-f system (L_3 and L_4 of f = 150 mm) using a CCD camera.

half of the intensity goes onto the higher orders with only $< 0.5\%$ remaining in the first order. Accordingly, if the mirrors are set to the ON-state ($+12°$), more than half of the intensity goes onto the zeroth-order while the intensity of the first-order is 4.2%. Whereas, if the mirrors are set to 24° and the reflected light is directly 24° apart from the incident beam while the DMD is switched on, 4.6% of the amount of light goes into the first-order. Significantly, it can be seen that the zeroth order is brighter than the higher order modes in Fig. 2-5 (b). Note that the efficiency results are wavelength dependent because DMDs have anti-reflection coatings which change efficiency based on the wavelength and the diffractive properties of the DMDs are also wavelength dependant, so at a different wavelength a different amount of energy will end up in the zeroth-order. Recent studies have shown that the efficiency of any given digital micromirror device is highly sensitive to the values chosen for each mirror width (w) and the spacing between mirror centers [102]. Having characterised the operational (ON and OFF) states of the DMD, we proceeded to generate optical modes using the binary hologram generation technique [91] (see Fig. 2-6 (a)).

We generated Laguerre Gaussian modes with varying topological charges, $\ell =$

$0, 1, 2$, and 3. To test this we expanded and collimated the beam produced by the helium neon (He-Ne) laser using two sets of lenses with 50 mm (near the He-Ne laser) and 150 mm (near the DMD) focal lengths. We mounted the device in a identical orientation to the one recommended by the manufacturer (24° alignment). Computer generated holograms were created and encoded onto the DMD [91]. The holograms for generating optical beams were created by modulating a grating function with 20 micromirrors per each period. These holograms were illuminated with the expanded beam and were diffracted by the DMD. Note that the displayed hologram at the DMD (in Fig 2-6 (b)) is stretched in its y-axis compared to the one on the left-hand side. This is because the DLP3000 screen is not a square. We designed the hologram to compensate the dimensions of the DMD so that it can fit on the DMD screen. A first-order of the generated LG beam was filtered using a pinhole and it was imaged using a 4-f system, from the DMD to the camera. The 4-f system reproduces a near-field of the generated optical beam. We used the DLP-lightcrafter software (offered by manufacturer) to load the holograms on the DMD. We also optimised the gain and exposure of the camera to avoid saturation so that the beams could be correctly identified.

The experimentally measured beams were compared to their matched simulation via the image correlation method. Image correlation is a basic tool which is often used to measure the correlation between simulated and experimental intensity profiles. The process involves overlapping the simulated and the measured intensities, and computing the non-localized correlation function. The correlation function determines the level of resemblance between two selected sub-images [103–105], and is expressed as

$$C = \frac{\sum_m \sum_n \left(A_{mn} - \overline{\mathrm{A}}\right)\left(B_{mn} - \overline{\mathrm{B}}\right)}{\sqrt{\left(\sum_m \sum_n \left(A_{mn} - \overline{\mathrm{A}}\right)^2\right)\left(\sum_m \sum_n \left(B_{mn} - \overline{\mathrm{B}}\right)^2\right)}}. \tag{2.18}$$

A and B are the images which have to be compared. The subscript indices m and n denote the pixel location in the image. When two selected sub-images are exactly the same, the correlation function C is 1. If there is no correlation between two

sub-images, the correlation function is 0.

Here we performed a correlation between two selected images: the reference image (simulated using Matlab), and the experimental image. Figure 2-7 shows a correlation of these LG beams. The results show an average of 98%, which implies a good indication that the simulated modes are reproduced experimentally.

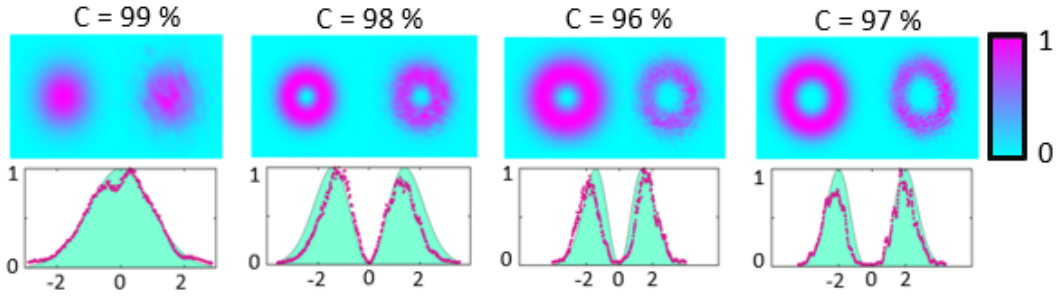


Figure 2-7: Simulated OAM modes ($l = 0, 1, 2$, and 3 from left to right) are compared with experimental beams using a correlation method. The correlation method works by comparing the intensities of the experimental results with simulated results.

In this section we have characterized digital micromirror devices and have outlined a tool for characterizing the quality of structured light beams generated in the laboratory. In the next section we will characterize a liquid crystal display and generate both scalar and vector beams.

2.2.2 Conversion efficiency of a liquid crystal display

Calibrating liquid crystal displays is critical. In principle, the correct way to calibrate a liquid crystal device is by adjusting the voltages to acquire the desired phase change while the digital hologram is displayed on the screen. This can be done using a 150 mm lens, a double pinhole, and a webcam detector. But here we used an LC device which was already calibrated, we only considered testing the conversion efficiency of the device. The reason for testing the conversion efficiency of the LC device is because of their capability of shaping light in different ways.

Here we show how to measure the optical efficiency of a liquid crystal display. We

employ a technique that exploits the superposition principle of optical beams to allow simultaneous generation of vector vortex beams using a single digital hologram, shown in Fig. 2-8 (a). Prior to measuring the first-order efficiency of a multiplexed beam, it is essential to firstly encode a single hologram onto the spatial light modulator, and to compare efficiencies of the first-order against the zeroth-order with different grating periods (shown in Fig. 2-8 (c)), using the experimental arrangement shown in Fig 2-8 (b). The intensity results were measured at a far field of the LC device, using a 300mm Fourier lens (FL). Our results show that choosing a smaller grating allows more light to be modulated into the first-order, the intensity profiles are shown in Fig 2-8 (e).

With all the conclusions made with a single hologram, we further encoded a multiplexed hologram using the same experimental arrangement to see whether the results will vary or not. We measured the multiplexed mode intensity of the first-order against the zeroth-order and the results are shown in Fig. 2-8 (d).

To experimentally generate multiplexed beams using Eq. (2.16), one must place a unique carrier frequency (grating) between them. Take note that when the carrier frequency between the multiplexed beams is increased, i.e., 60 mm^{-1}, more power goes onto the zeroth-order. This deprive the amount of light from getting modulated by the first-order. Therefore, more intensity should go to the order of interest. When the carrier frequency between the multiplexed beams is reduced i.e., 20 mm^{-1}, it almost impossible to separate the modulated multiplexed beam with a D-shaped mirror, the beam gets cut out by the edges of the mirror. In our work, we selected two reasonable grating frequencies, one between the OAM modes is ($G_x = G_y = 30$ mm^{-1}) and the other between zeroth-order and first-order is ($G_x = G_y = 60$ mm^{-1}), accordingly. The results show that the multiplexed beams have uniform intensity. This means that any mode can be encoded on any channel.

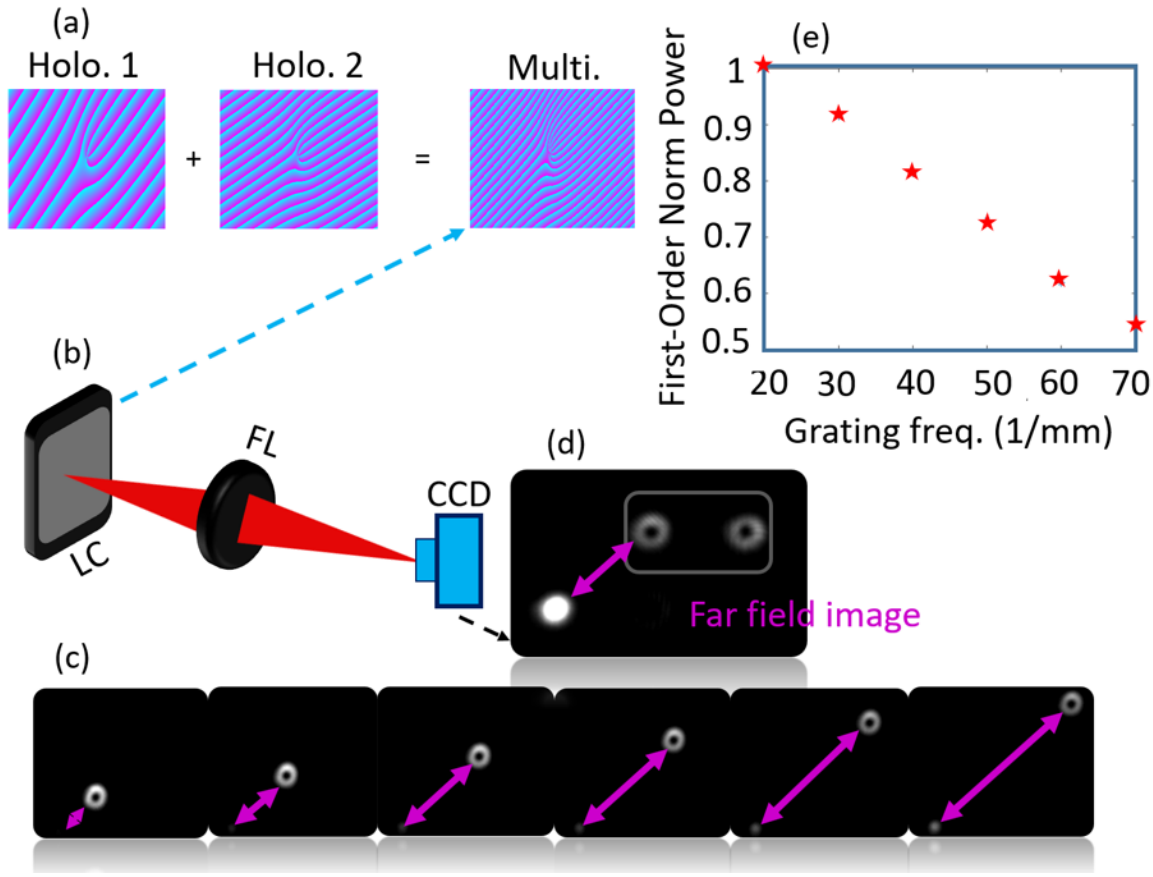


Figure 2-8: (a) Two holograms (Holo.1 and Holo.2) combined to form a multiplexed hologram (Multi.), and is displayed at the LC display. (b) Experimental arrangement to measure the conversion efficiency with a multiplexed hologram on a liquid crystal device. Here FL is the Fourier lens of f=150 mm. (c) First-order and zeroth-order results with an increasing grating frequency ($G_x = 20 - 70$ mm^{-1}). (d) Zeroth-order and a multiplexed mode with a grating period of 30 mm^{-1} and an OAM of $\ell = 1$. (e) Results of first-order power with their respective gratings.

2.2.3 Fringe visibility of an interferometer

In this section we design an interferometer that will be used to generate vector modes. Liquid crystal displays will be used to generate two distinct beams that will be combined using a beamsplitter [101]. To characterize the quality of the interferometer we measure the visibility, which determines how coherent the two beams are.

The fringe visibility is described in terms of the observed intensity maxima and minima in an interference pattern by

$$V_M = \frac{I_{max} - I_{min}}{I_{max} + I_{min}}, \tag{2.19}$$

where I_{max} and I_{min} are the maximum and minimum intensities. If $I_{min} = 0$, V_M becomes 1. This means that the visibility is the optimum. Likewise, If $I_{max} = I_{min}$, V_M becomes zero.

Figure 2-9 (b) shows an example of two beams propagating in different paths (A and B) that are combined using a beamsplitter (BS). A spatial filter is introduced after the BS to filter out higher spatial frequencies. The generated hologram in Fig. 2-9 (a) is a multiplexed hologram and has a topological charge of zero. This means that both carriers have a Gaussian element only. The combination of the beams after the beamsplitter is viewed using the CCD camera. Because of their small angle of separation, the beams interfere fringes are observed (see Fig. 2-9 (c)). The analysis of the interference pattern is shown in Fig. 2-9 (d). We performed a theoretical fit of the measured cross-section intensity by superimposing two identical Gaussian beams with a slight angular separation and the beams were not so destructive.

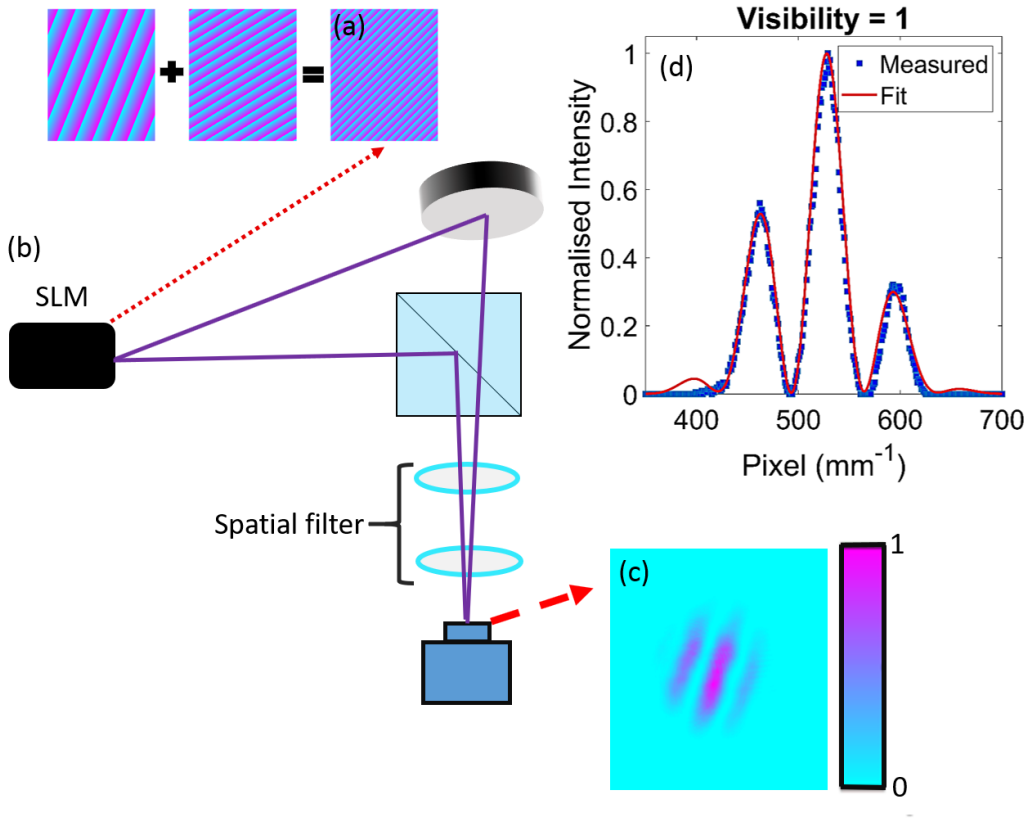


Figure 2-9: (a) A set of two digital holograms merged into a multiplexed hologram. (b) An experimental arrangement to check the fringe visibility of the interferometer using two multiplexed Gaussian beams. (c) Visible fringes produced when the angle of the beam between path A and B are interfered. (d) A curve-fit of the intensity profiles using the interference pattern results.

The small angle between the beams often occurs when using interferometers to build an experimental arrangement. This is because interferometers are highly sensitive to vibrations, especially if the optical bench is not stable. Vibrations slightly change the path length of the arms. A note to be considered when building an interferometer to generate optical beams is that, the path length must be equal on both arms (from the LC to the beamsplitter, where they combine) and the beams should overlap co-linearly.

The results show that small angles cause interference on input Gaussian beams and this must be controlled in the laboratory.

2.3 Generating vector beams using an interferometer

In the previous sections we have characterized two different spatial light modulators. In this section we discuss the generation of scalar and vector vortex beams, and we characterize these two classes of spatial modes, using the experimental arrangement in Fig. 2-10. We provide tips and precautions to consider when generating large OAM modes with a multiplexed beam on an SLM. We experimentally generate these beams in free-space. Both spatial light modulator's grating frequencies are set to their best contrast. While we also included a DMD in the experimental arrangement, it will only be used later for encoding turbulence onto vector modes. Here we only used it to diffract the input (vector) mode into the first order and finally characterised the beams by using a polariser and a CCD camera.

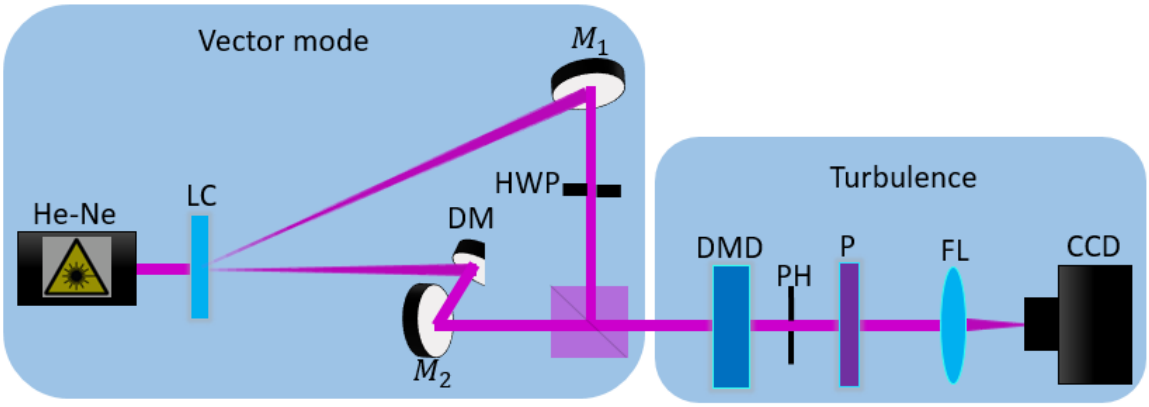


Figure 2-10: An illustration of the experimental arrangement. A Helium Neon (He-Ne) laser was expanded and collimated onto a liquid crystal (LC) display. Two modes were generated simultaneously from the SLM and were then separated using a D-shaped mirror (DM) and recombined with a beamsplitter (BS). The recombined modes were imaged to the digital micromirror device (DMD), where the turbulence was encoded in combination with the detection holograms. A polariser (P) was added in-order to change the polarisation states. The resulting modes were propagated to the far field with a 500 mm Fourier lens (FL), where the on-axis intensity measurements were performed.

We now describe the vector mode generation process. Firstly, we use a He-Ne

laser to illuminate a multiplexed hologram, displayed on a liquid crystal device. Our liquid crystal display only modulates horizontally polarized light. We check the visibility of the modulated beam prior to introducing additional optical elements. This minimizes the misalignment of a system and the efficiency for each digital device is controlled without affecting the efficiency of the DMD screen. Secondly, we propagate a multiplexed beam from the liquid crystal to the beamsplitter. We observe the fringe visibility when the beam passes through the BS. If fringes appear destructively, we control the angles from both arms until the fringes disappear and a desired intensity profile is observed. This indicates that the two beams are well overlapped. The controlling of angles involves tilting the BS (either up or down) by a few microns. This means that, the beamsplitter must be mounted on a rotational tilting stage. The last step is performed only once the system is properly aligned and no fringes appear. The last measurement involves bouncing the beam onto a DMD and observing the visibility. It is advisable to switch off the air-conditioner in the laboratory when working with interferometers to avoid perturbations of the beam.

To generate scalar beams with a multiplexed hologram, we encode $\ell = 1$ and $\ell = -1$ on the two holograms, and propagate them towards the BS. A first-order is filtered using a pinhole from the DMD and Fourier transformed by a lens (of 500 mm focal length) to its Fourier plane where the CCD camera is located. Figure 2-11 (a) shows experimental results of superpositions, $\ell = 3, 5, 10,$ and 20 and $\ell = -3, -5, -10,$ and -20 of the multiplexed scalar beams. The patterns observed in the Fourier plane of the DMD are known as petals. The scalar beam's intensity is uniformly distributed, even in the higher-order topological charges, like $\ell = 20$. How does the petal structure arise? Firstly, since the two beams have the same polarisations, they superimpose coherently. That is, in the azimuthal coordinate, ϕ, the fields add up and result in an intensity profile $|1/\sqrt{2}\,(\exp(i\ell\phi) + \exp(-i\ell\phi))\,|^2 \propto \cos^2(\ell\phi)^2$, where $\pm\ell$ are the corresponding OAM charges of the beam. Consequently, this means that the petal structure will have $2 \times |\ell|$ petals about the azimuth of the final beam.

During the experiment process in the laboratory, we realised that when the pinholes (placed between the LC device and DMD) are set to only filter lower-order

modes, e.g., ($\ell = \pm 3$) to generate beams, the intensities of large OAM modes would be cut-off. Therefore, it is important to make sure that all pinholes in between the LC device and DMD are controlled frequently to allow higher-order beam's intensity to be detected when large OAM holograms are encoded at the LC display. The pinholes must also be controlled even when lower-order modes are being generated, to filter out stray light and higher order modes from interfering with the desired results. Note that any generated mode from the LC device must still fit on the DMD screen. This means that the incident beam size must not be larger than the DMD screen.

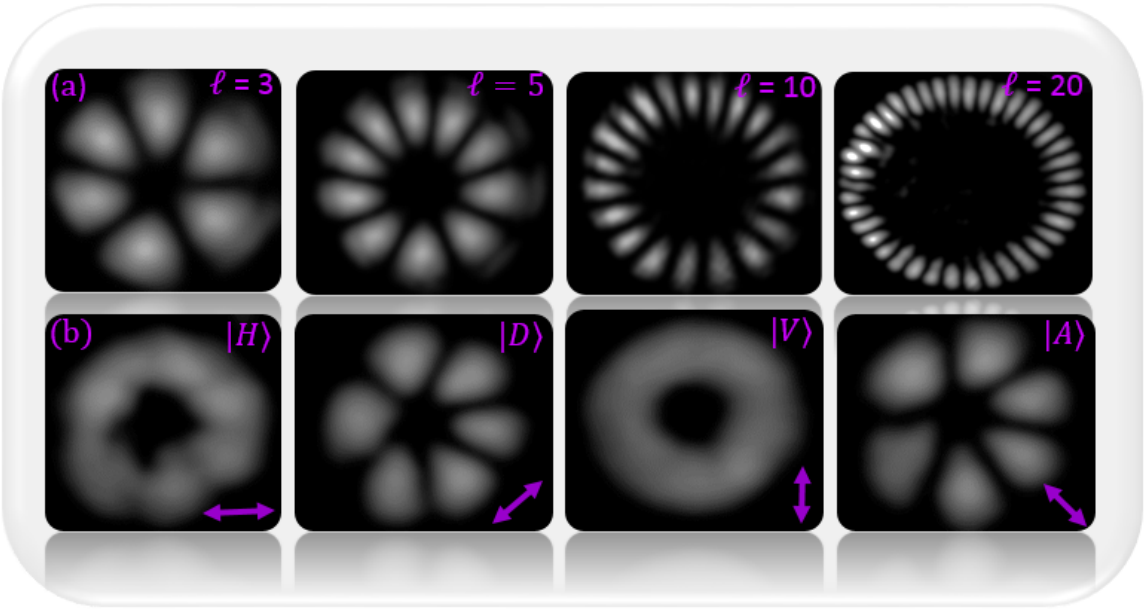


Figure 2-11: (a) Superposition of OAM modes. Here we tested modes of OAM subspaces of $\ell = \pm\ 3, 5, 10,$ and 20 (from left to right). (b) Experimentally generated vector beams with superpositions of $\ell = 3$. Here the arrows represent the polarisation states (horizontal, diagonal, vertical, and anti-diagonal) that the OAM mode was projected at a time.

Furthermore, we generated vector vortex beams using the same experimental arrangement that we used to generate scalar beams; except that in this case, one arm had a half-wave plate. A rotatable polarizer was added between the DMD and the camera to change the polarisation of the incident light. The aim was to make the polarisations of the generated fields orthogonal. As such we marked the, $\ell = -3$ mode with a vertical polarisation ($\hat{e}_V$) and the $\ell = 3$ mode with a horizontal polarisation

state ($\hat{e}_H$). The desired vector mode can be expressed as

$$\mathbf{U}(\mathbf{r}) = u_{-\ell}(\mathbf{r}) \exp(-\ell\phi)\hat{e}_V + u_{\ell}(\mathbf{r}) \exp(\ell\phi)\hat{e}_H. \tag{2.20}$$

In this case, the vertical, $\hat{e}_V$ and horizontal, $\hat{e}_H$ polarisation modes were coupled to the spatial modes of OAM, $u_{\pm\ell}(\mathbf{r}) \exp(\pm\ell\phi)$, having identical radial amplitudes and orthogonal and azimuthal phase fronts that are distinguished by their topological charge $\pm\ell$. Unlike superpositions with identical polarisations, the polarisation field determines the observed spatial mode, in the vector modes. In our experiment, to generate such a mode, a horizontally polarized beam is impinged onto a liquid crystal display, where it acquires a topological charge, let's say $\ell = +1$ and is multiplexed with its opposite charge. Using a D-shaped mirror, the multiplexed beam was separated into two different arms before reaching the beamsplitter. One beam remains with the horizontal polarization component and the other beam passes through a half wave-plate (HWP), where its polarization component is converted to the vertical state. The final projection is performed with a linear polariser, which projects onto various linear polarisations states depending on its orientations. Figure 2-11 (b) shows horizontal $|H\rangle$, diagonal $|D\rangle$, vertical $|V\rangle$, and anti-diagonal $|A\rangle$ polarisation projections (from left to right) results. We projected the vector mode onto the horizontal, vertical and their equally weighted superpositions of diagonal ($\hat{e}_H + \hat{e}_V$) and anti-diagonal ($\hat{e}_H - \hat{e}_V$) states. The orientation of the polariser is shown in Figure 2-11 (b) as arrows relative to the horizontal polarisation state is aligned with the horizontal axis or its orthogonal vertical axis, the intensity profile resembles a well defined OAM mode. The results show that when the polariser is oriented in the diagonal or anti-diagonal ($\pm 45°$) states, azimuthal fringes are observed showing $2 \times |\ell| = 6$ resulting from the interfering OAM modes due to the polarisation measurement.

In this section we have demonstrated the generation of structured light beams, both scalar and vector in nature, in the laboratory. In the next section, we introduce a technique to characterise them quantitatively.

2.4 Vector quality factor

In the previous section we introduced tools to generate spatial modes that have coupled spatial and polarisation components. The principle result was the generation of vector vortex beams. Such beams have recently attracted interest in diverse fields including optical microscopy [46, 106], optical tweezers [51, 107], atmospheric turbulence [67, 108], quantum memories [109], and data encryption [110]. Although we only demonstrated an interferometric approach that is commonly used to prepare them [101, 111–114], numerous tools have been developed to generate them using laser cavities ([115, 116]) or by using custom elements [117–126]. Similarly, various techniques have been developed to detect and characterise vector modes, for example using rotating analyzers with interferometers [127], as well as geometric phase plates in combination with single-mode fibers [53], and through quantitative measures such as the vector quality factor methods [128].

In this section we explore the last method, VQF, as it is crucial in investigating the effects of turbulence on vector modes. The vector quality factor (VQF) method differentiates vector modes from scalar modes based on how non-separable (entangled) the spatial and polarisation components are.

It is instructive to consider a transverse electric field in a coordinate system in the form

$$\mathbf{U}(r, \phi, \theta) = \cos(\theta)\exp(-i\ell\phi)\mathbf{e_L} + \sin(\theta)\exp(i\ell\phi)\mathbf{e_R}, \tag{2.21}$$

where $\mathbf{e_L}$ and $\mathbf{e_R}$ denote left- and right-handed polarization states associated with OAM carrying spatial modes distinguished by a topological charge $\pm\ell$ being the azimuthal index of the beam. For brevity, we only used the azimuthal component of the spatial profile since the OAM basis modes are cylindrical symmetric. In general, the radial component has to be considered. The parameter θ specifies whether the transverse mode, $U(\mathbf{r}, \theta)$, is purely vector ($\theta = (2n + 1)\pi/4$) or purely scalar ($\theta = 2n\pi/2$), where n is a positive integer.

We use a quantity from quantum mechanics, namely the concurrence C [129] (being the degree of entanglement) to define VQF as [128]

$$VQF = Re(C) = Re\left(\sqrt{1-s^2}\right) = |\sin(2\theta)|, \tag{2.22}$$

where s is the length of the Bloch vector, defined as

$$s = \left(\sum_i \langle \sigma_i^2 \rangle\right)^{1/2}. \tag{2.23}$$

Here, $i = 1, 2, 3$ and $\langle \sigma_i \rangle$ are the expected values of the Pauli operators, representing a set of normalized intensity measurements. In practise, s corresponds to the degree of polarization of the averaged polarization.

For a left-(right-)circularly polarized scalar vortex mode, $\theta = 0(\pi/2)$. To calculate s, 12 normalized, on-axis intensity measurements are required: six identical measurements performed for two different basis states. The intensities I_{ij}, normalized to the maximum of I, are defined by the chosen measurement basis i, with six projective measurements j. If circular polarization is chosen as the measurement basis, for instance, $i = \{L, R\}$; the projection measurements are represented by two pure OAM modes, $\pm\ell$, and four superposition states, $\exp(i\ell\phi) + \exp(i\alpha)\exp(-i\ell\phi)$, defined by the inter modal angle α. Importantly, the polarisation measurement basis must match the modes marking the independent spatial modes. For example, using the linear basis, for a vector mode in Eq. (2.20), the polarisation projections can be mapped as $i = \{H, V\}$. Table 2.1 presents the intensities assigned to its respective basis state and projective measurement for a first-order vector vortex mode. Note that the polarisations can be defined in any orthogonal basis and therefore the measurement bases must be adapted accordingly.

Polarisation projections	ℓ_1	$-\ell_1$	α_1	α_2	α_3	α_4
L	I_{11}	I_{12}	I_{13}	I_{14}	I_{15}	I_{16}
R	I_{21}	I_{22}	I_{23}	I_{24}	I_{25}	I_{26}

Table 2.1: Normalized intensity measurements. The symbol $\alpha_1 = 0,\ \alpha_2 = \pi/2,\ \alpha_3 = \pi,$ and $\alpha_4 = 3\pi/2$ are the relative phases for the spatial mode superpositions.

The six OAM state measurements quantify the higher-order Poincarè sphere vector [119]. This traditional technique is adapted from a full-state tomography often used for quantum entangled states, where an over-complete set of measurements is used to determine the full density matrix and compute the degree of entanglement [130]. The expected values of the Pauli operators are computed from the intensities (I) as follows:

$$\langle\sigma_1\rangle = (I_{13} + I_{23}) - (I_{15} + I_{25}), \tag{2.24}$$

$$\langle\sigma_2\rangle = (I_{14} + I_{24}) - (I_{16} + I_{26}), \tag{2.25}$$

$$\langle\sigma_3\rangle = (I_{11} + I_{21}) - (I_{12} + I_{22}). \tag{2.26}$$

These expectation values bear a resemblance to the Stokes parameters used to recover the polarization distribution of a beam [131]. However, they are fundamentally different since they do not represent a series of polarization measurements but rather a series of holographic measurements of the spatial field. They give a measure of the degree of nonseparability of vector beams.

Figures 2-12 (left and right) shows 12 normalized intensity measurements of a vector and scalar vortex beam, respectively. In this case, the circular polarization basis was chosen and six different OAM projections were made for both the left- and right-circular polarization states.

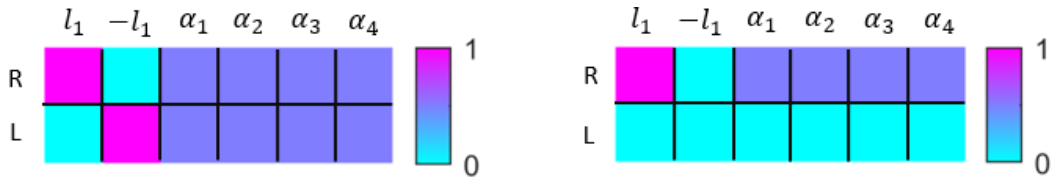


Figure 2-12: Intensity measurements corresponding to those in table 2.1. Two examples are illustrated, a vector vortex mode (left) and a scalar vortex mode (right). The vector vortex mode exhibits both polarization states and is non-separable, whereas the scalar mode subplot has one polarization component and is separable.

2.5 Experimental VQF measurements

Using the experimental arrangement in Section. 2.3 we generated vector modes and characterised them quantitatively using the VQF measure. This section shows the proof of concept for the VQF theory explained above. The experimental results are shown in Fig. 2-13 as points while the corresponding theory is shown as dotted lines. We generated vector modes following Eq. (2.20), in the linear polarisation basis. To control the weightings between the horizontal and vertical components, we varied the grating depth by changing the relative weightings between the multiplexed holograms such that the final hologram was $\Phi(x,y) = \text{mod}\{a\text{Hol}_\ell(x,y) + (1-a)\text{Hol}_{-\ell}(x,y), 2\pi]$, with $\text{Hol}_\ell(x,y)$ encoding the first $\ell = 1$ mode while $\text{Hol}_{-\ell}(x,y)$ encoded the $\ell = -1$ mode. The weightings were adjusted so that, $\theta \approx a\pi/2$ for $a = [0, 0.5]$. Accordingly, the measured VQF followed the theoretical relation $V = |\sin(2\theta)|$ (see Eq. (2.22)). For $\theta = 0$ and $\pi/4$, we obtained a VQF of $V = 0.012 \pm 0.006$ and $\theta = 0$, $V = 0.999 \pm 0.006$ while a perfect system would have $V = 0$ and 1, respectively, indicating that we have generated purely scalar and vector modes. The states between these two extremes were also generated successfully, however, with a slight deviation from theory. For example, for $\theta = \pi/8$, we measured a VQF of $V = 0.609 \pm 001$ while the theory value should be $V = 0.701$. The results show a good quantity of the vector mode.

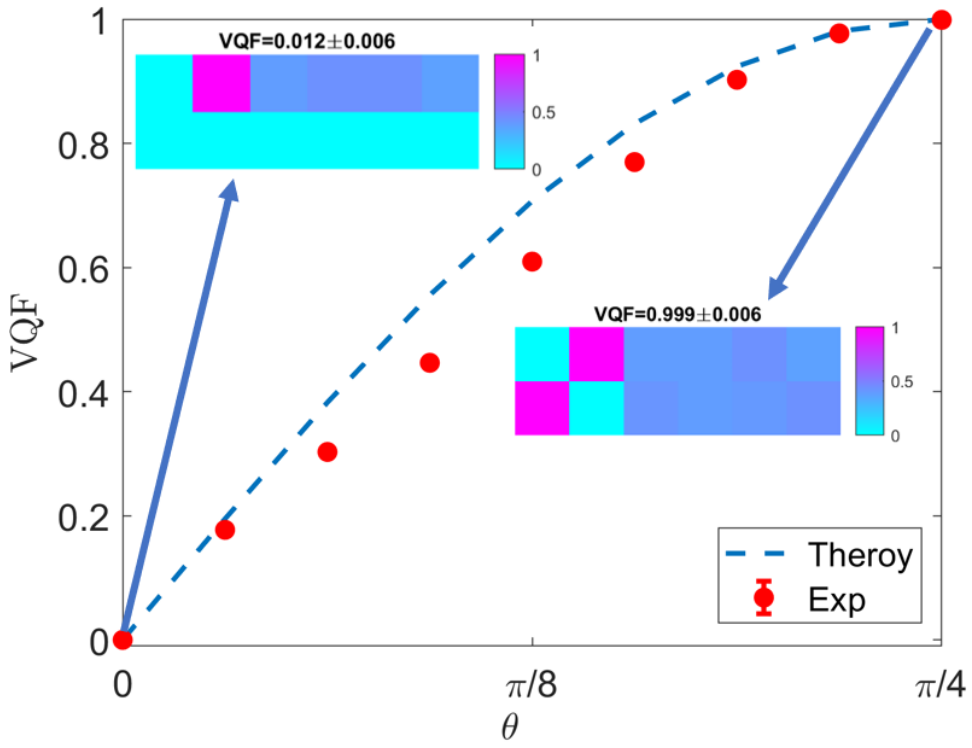


Figure 2-13: Experimental generation and characterisation of vector modes ranging from completely scalar to (VQF=0) to vector VQF(1).

In this section, we have discussed the VQF tool used to measure separable against non-separable modes of light. In the next chapter we will use this tool to generate and characterize vector modes in turbulence.

2.6 Conclusions

In this Chapter, we introduced a toolbox for tailoring the amplitude and phase of optical beams. Firstly, for full control of optical fields, we employed two types of spatial light modulators in the form of digital displays: a liquid crystal display and a digital micromirror device. These devices control the dynamic phase and amplitude of light by addressing individual pixels. We demonstrated how to generate holograms using spatial light modulation. As a result, we successfully generated gratings imprinted with the desired field information. As an example, we generated optical modes car-

rying orbital angular momentum with high accuracy.

To complete our tool box, we demonstrated two techniques used to characterize structured light beams: the correlation method and the VQF. The first method measures the correlation between simulated and experimental images. This technique was used to measure the intensities that is lost from a beam. The VQF quantifies beams from purely scalar (0) to purely vector (1). We experimentally demonstrated, the distinction between scalar and vector vortex beams in terms of the separability of their degrees of freedom. The analysing of information carried by spatial modes, also provides the ability to study light propagating through random media.

In the next Chapter, we create phase screens to simulate turbulence using two different turbulence data and two models, and we experimentally analyse the perturbations caused by the phase screens on a laser beam. Using the SLMs and the VQF technique, we demonstrate optical turbulence in the form of digitally encoded random phase screens using Kolmogorov's statistical models for turbulence. Furthermore, we explore the transfer of vector vortex modes information through free-space and turbulence channels, and we demonstrate the robustness of large OAM modes through turbulent atmosphere.

Chapter 3

Experimental results

Thus far, we have demonstrated the generation of spatial modes using spatial light modulators and shown how they can be characterised using simple linear optical elements. In particular, we showed that the polarisation and spatial components of optical beams can be characterised using quantitative methods like the vector quality factor (VQF), enabling us to distinguish purely scalar and purely vector beams. The VQF measure may be used as a powerful tool for studying deleterious effects that impact the transmission of information encoded in the transverse spatial modes of light. For example, it has proven useful in demonstrating the reconstruction of the phase, amplitude and polarisation of light after encountering absorptive obstructions [64]. Moreover, it has also been proven to be useful in characterising quantum systems with phase dependent aberrations due to optical turbulence at the single photon level [132] owing to the entanglement-like-nature of the nonseparability arising in vector modes.

While the VQF tool offers a novel method of investigating the effects of turbulence effects on optical modes, it is also essential to devise methods for measuring turbulence directly so we can gain better insight into how it evolves. We are able to use this information to accurately model how turbulence affects optical beams and to develop better compensation and adaptive methods to ameliorate the effects of turbulence.

In this Chapter we calculate the strength of optical turbulence and synthesise phase screens. Subsequently, we then demonstrate the benefit of using such phase

screens for studying the effects of optical turbulence on vector modes. To achieve, this we describe the installation and operation of an ultrasonic anemometer. This instrument maps the spatio-temporal distribution of turbulence in the atmosphere. The instrument measures the wind velocity, and we derive the refractive index structure function from the data acquired. We develop an experimental test bed to characterize optical turbulence, using an old commercial projector (that has a DMD in it). Furthermore, we use the VQF technique to characterize scalar and vector beams through turbulence, and in free-space channels. We investigate the contribution of mode separation on the non-separability to demonstrate resilience for higher order OAM state spaces against turbulence.

3.1 In-situ velocity measurements

The work herein has been accepted by IEEE Photonics Society (IPS) Journal of Selected Topics in Quantum Electronics.

To acquire the atmospheric data we deployed a three-dimensional wind vector instrument, a sonic anemometer. A photo of two of these devices attached to the rail of a building in the optical test facility at the CSIR is shown in Fig. 3-1. The location where the instrument is installed is used for testing optical performance of surveillance systems. The main purpose of installing the instrument was to map the velocities of the airflow in-order to calculate and study deleterious effects of near field turbulence on imaging systems.

An additional temperature sensor, a platinum resistance thermometer (PRT), was mounted near the sonic anemometer heads to measure the temperature. The mounting was done firm to prevent inaccurate measurements. The structure to which the mounting bar was attached was on the downwind side of the probe to minimize shadowing of the wind (as shown in Fig. 3-1), the instrument does not move from its position. For best results, the probe was mounted on a boom laterally from the structure. The output cables were fed through the mounting bar and connected to the end of the probe array. The instrument was slid into the mounting bar, lining up the holes in the probe array with the thumbscrews in the mounting bar. The array is secured using the thumbscrews. The other end of the output cable was connected to the serial port of a computer and power source to supply communication.

The sonic anemometer is supported by a number of electronic components, responsible for converting ultrasonic signals into readable results. Myself, together with the optronics sensor systems team at the CSIR, we designed, and integrated the electronic control system (shown in Fig. 3-2) which involves the sonic anemometer, the PRT sensor and the two main communication interface. The Gill electronic box contains a six digitized analogue input connections. The components were dispatched to the power and communications interface anemometer (PCIA) in the RS485 data stream, enabling external sensors to be connected. We also installed a sensor to ac-

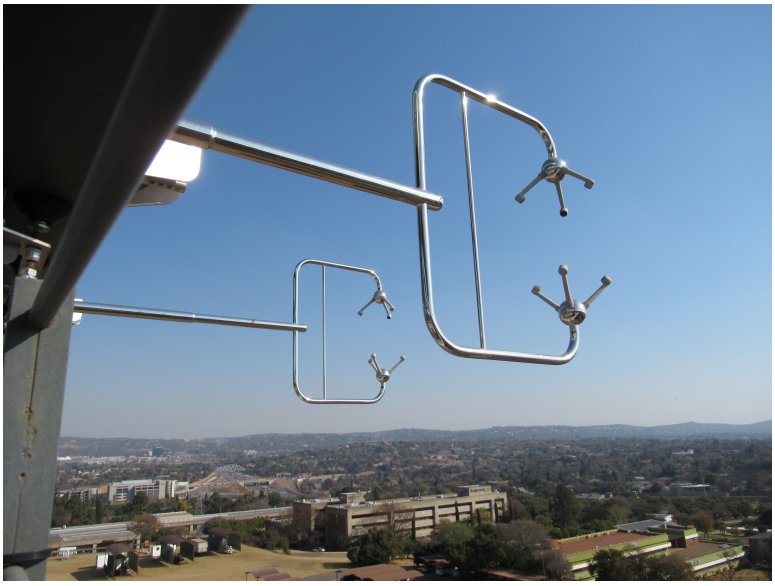


Figure 3-1: A pair of sonic anemometers mounted on a rail at building 44, situated at the CSIR. This instrument is discussed in Chapter 1.

quire humidity at the same time-base as the sonic anemometer. The PCIA supplies power to the sonic anemometer and converts the RS422 signal to the RS232 signal acquired by a computer. The data of the anemometer are stored in a RS422 format and they can be converted to analogue data with the PCIA unit [133].

We tested our connections using the Gill instrument and the electronic components. Testing started with checking the communications and data output from the Gill PCIA unit. This was done using the Gill RCom II software. The initial test starts by connecting a PC to the RS232 output of the PCIA unit (via cable S1 to S2 is routed directly to a native serial port on a PC). Next, we verified that the Gill instrument and associated hardware was working. Communications were established via the Tibbo (serial-over-IP) device. The setup involved Tibbo VSP manager, which is part of the Tibbo device server toolkit.

All the electronic components were tested successfully. The last step was to convert the signals into digital numeric values that can be manipulated by a computer. Since the Tibbo has a wifi adapter, we connected network configurations. The Tibbo setup files were saved and stored in the Tibbo Device Server (DS) Manager.

My CSIR colleague, Derek wrote a python module called sonnet.py to perform

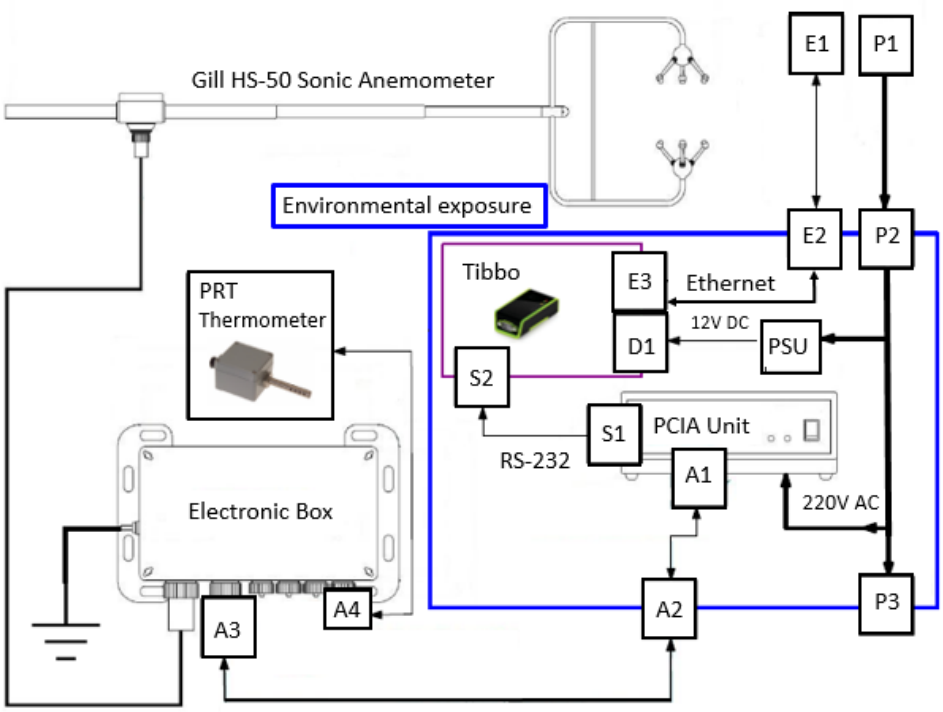


Figure 3-2: Schematic setup for acquiring velocities of the airflow. This experimental arrangement show the electronic components, feeding signal to the sonic anemometer. All this components collect and convert the ultrasonic signal into readable values.

data acquisition from a number of sonic anemometers attached to serial ports on a single computer. The serial communication with the sonic anemometers is transmitted over IP/ethernet links using the Tibbo hardware in the anemometer environmental enclosure. A serial port is used only for a convenient initial setup of the sonic anemometers. The sonnet.py module has two main classes, namely the anemometer class and the SonNet class. When the SonNet class is initiated, it reads the instrument network configuration file "sonic anemometer network" and proceeds to initiate the anemometer class for the instrument in the SonNet. A method is called-up to start SonNet data acquisition. A simplified flow diagram of data acquisition component in the sonnet.py is shown in Fig. 3-3.

Finally, a large amount of data was saved into the computer. These data included parameters such as velocities, sonic temperature, actual temperature, pressure, timestamps, etc. All these parameters are important for computing the refractive index structure function, which is often used to synthesize turbulence using real-world

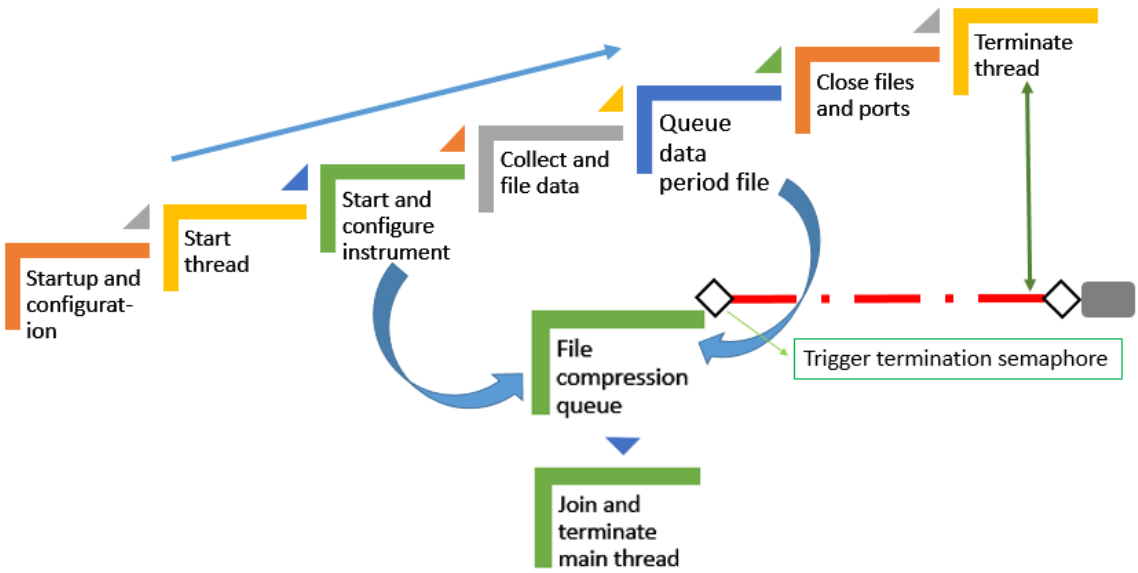


Figure 3-3: Data acquisition in the sonnet.py module.

data. This data was recorded from 10 January 2020 up to almost 28 January 2020.

3.1.1 Results and discussion

Analysis of velocities

The spatial variations of the wind velocities were investigated by analyzing horizontal, vertical, and diagonal distribution of the airflow. The comparison between the pair of a single transducer and the integrated path represent a single point measurement. Figure 3-4 (a) and (b) shows results of different wind velocities. The results show that the transducer components (U, V, and W) measured different velocities (shown in Fig. 3-4 (a)). The colors green, red, and blue represent the U, V, and W component. The velocity results for U and V components are quite low (between 0 and 1 m/s) and they do not differ a lot from one another, while the velocities for the W vector is slightly higher (to almost 2 m/s) than that of the U and V components. This results were continuously monitored every 3 minutes to prevent false results which may result from instrument failure and birds which may fly and block the airflow during the recording process. The mean wind velocity (MWV) shown in

Fig. 3-4 (b) was calculated as

$$MWV = \sqrt{U^2 + V^2 + W^2}. \tag{3.1}$$

The results show a variation in the mean velocity on different days. The variation shows disparity because the data was recorded for many days. This becomes more interesting than just analysing data that was obtained on a single day.

Refractive index and coherence length analysis

From the wind speed results, we calculated the refractive index structure constant, C_n^2 using Eq. (1.19) and the results are shown in Fig. 3-4 (c). The variation in the refractive index can be observed as the time changes. An intermittent turbulence strength (in the order of 10^{-16}) $\mathrm{m}^{-2/3}$ is observed. The reason is the strong turbulence that build up close to the ground by heat, resulting in increase in wind speed.

We further calculated the Fried parameter, r_0, from the refractive index structure results. Figure 3-4 (d) shows results of the calculated coherence length with three different propagation distances (0.5 km, 1 km, and 2 km). The results show a small propagation distance (0.5 km) have larger coherence length in comparison with 1 km and 2 km (being the L symbol in the equation) distances. The further a beam travels the more its wavefront become planar and this is further enhanced by turbulence.

In the next section, we use the calculated C_n^2 values to create turbulence phase screens using two different turbulence models.

3.1.2 Simulating turbulence in the lab

Here we outline two general approaches that we used to simulate optical turbulence using liquid crystal displays and digital micromirror devices for use in a laboratory environment. Optical turbulence phase screens have been utilised in a myriad of experiments for studying the evolution of spatial modes through turbulence [134–136].

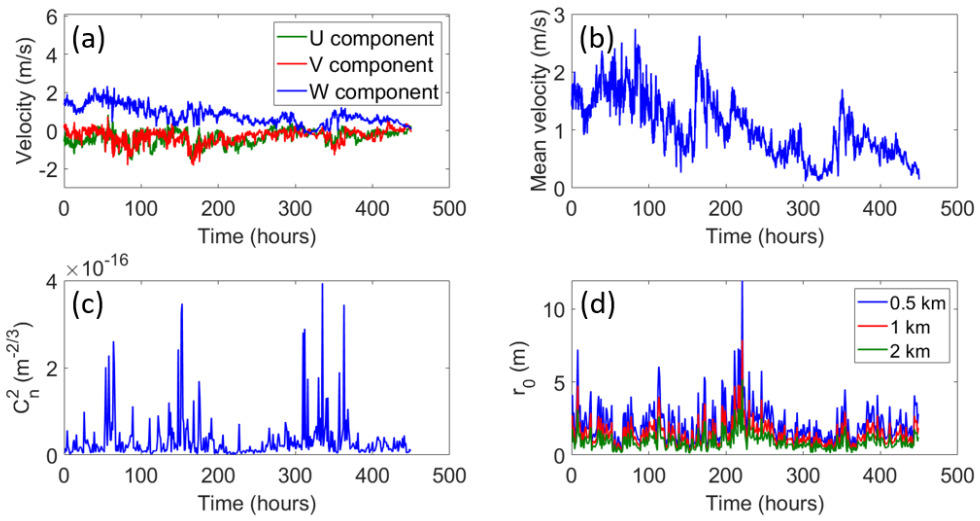


Figure 3-4: Calculated results from real-world measurements. (a) U, V, W wind velocities. (b) Average mean wind velocity. (c) Refractive index structure constant, C_n^2. (d) Coherence length, r_0 values with different propagation distances.

Various numerical methods have been developed to approximate the phase that is imparted on optical beams upon traversing turbulence. One such technique approximates the phase screens, as superpositions of Zernike polynomials. This technique was adopted to simulate turbulence phase screens because it forms a neat basis-set for describing the optical phase and in general, it can generate turbulence phase screens much faster. The Zernike polynomial coefficients can be directly connected to known optical aberrations (see Table 3.1) and it can be computed analytically.

One of the principal uses of the Zernike polynomials is to represent fixed aberrations in optical systems in the form of Zernike polynomials. These polynomials can be expressed in a form [137–141]

$$Z_n^m(\rho,\theta) = \begin{cases} U_{nm}(\rho,\theta) & : m < 0; \quad |m-n| = \text{even} \\ V_{nm}(\rho,\theta) & : m \neq 0; \quad |m-n| = \text{odd} \\ R_n^0(\rho) & : m = 0 \end{cases}, \tag{3.2}$$

where

$$U_{nm}(\rho,\theta) = R_n^m(\rho)\cos m\theta,$$

j	n	m	$Z_j(\rho,\theta)$	*Aberration*
1	0	0	1	Piston
2	1	1	$2\rho\cos\theta$	x tilt
3	1	1	$2\rho\sin\theta$	y tilt
4	2	0	$\sqrt{3}(2\ \rho^2-1)$	Defocus
5	2	2	$\sqrt{6}\rho^2\sin 2\theta$	45 deg Primary astigmatism
6	2	2	$\sqrt{6}\rho^2\cos 2\theta$	0 deg Primary astigmatism
7	3	1	$\sqrt{8}(3\rho^3-2\rho)\sin\theta$	Primary y coma
8	3	1	$\sqrt{8}(3\rho^3-2\rho)\cos\theta$	Primary x coma
9	3	3	$\sqrt{8}\rho^3\sin 3\theta$	
10	3	3	$\sqrt{8}\rho^3\cos 3\theta$	
11	4	0	$\sqrt{5}(6\rho^4-6\rho^2+1)$	Primary spherical

Table 3.1: Expressions for the Zernike Polynomials Z_j. Here, $Z_j(\rho,\theta)$ represents $Z_n^m(\rho,\theta)$ [2]. The aberration column indicate the types of aberration with respect to its Zernike polynomial.

$$V_{nm}(\rho,\theta) = R_n^m(\rho)\sin m\theta,$$

and

$$R_n^m\rho = \sum_{s=0}^{(n-m)/2} \frac{(-1)^s(n-s!)}{s!(\frac{n+m}{2}-s)!(\frac{n-m}{2}-s)!}\rho^{n-2s}. \tag{3.3}$$

n and m are the radial and azimuthal indices.

The orthogonality of the Zernike basis functions allows any phase function ($\phi = (\rho,\theta)$) to be represented as a sum of the weighted Zernike polynomials, and is given by

$$\phi(\rho,\theta) = \sum_{n=0}^{\infty}\sum_{m=0}^{n}[A_{nm}U_{nm}(\rho,\theta) + B_{nm}V_{nm}(\rho,\theta)]. \tag{3.4}$$

Here the amplitudes A_{nm} and B_{nm} (even and odd terms) are given by

$$A_{nm} = K(m)\left(\frac{n+1}{\pi}\right)\int_0^{2\pi}\int_0^1 \phi(\rho,\theta)U_{nm}(\rho,\theta)\rho\mathrm{d}\rho\mathrm{d}\theta, \tag{3.5}$$

$$B_{nm} = K(m)\left(\frac{n+1}{\pi}\right)\int_0^{2\pi}\int_0^1 \phi(\rho,\theta)V_{nm}(\rho,\theta)\rho\mathrm{d}\rho\mathrm{d}\theta, \tag{3.6}$$

where

$$K(m) = \begin{cases} 2: & \text{for} \quad m = 0, n \neq 0 \\ 1: & \text{otherwise} \end{cases} . \tag{3.7}$$

The phase screen is created by both, the sum of the Zernike polynomials and their coefficient terms, found from Noll's covariance method [31,139]. The Noll matrix I_{nm} is used to compute the statistical nature of the Zernike coefficient terms required to explain turbulence. For the Kolmogorov spectrum the coefficients, A_{nm} and B_{nm} in Eq. (3.4) can be sampled from a normal distribution with zero mean and a variance of

$$\sigma_{nm}^2 = I_{nm}\left(D \Big/ r_0\right)^{5/3}, \tag{3.8}$$

where D and r_0 are the aperture diameter and coherence length. Here I_{nm} is

$$I_{nm} = \frac{0.15337(-1)^{n-m}(n+1)\Gamma(14/3)\Gamma(n-5/6)}{\Gamma(17/6)^2\Gamma(n+23/6)}. \tag{3.9}$$

The symbol $\Gamma(x)$ is the gamma function. This turbulence model produces phase screens with statistical properties consistent with the Kolmogorov model for atmospheric turbulence. Figure 3-5 shows a turbulence phase screen, computed using the sum of the phase functions (the first five aberrations presented in Table 3.1), multiplied by their respective polynomial coefficients. The phase screens changes as you change the values of D/r_0 in Eq. (3.8) and the resulting phase screens from this change can be seen in Fig. 3-6.

An alternative method to simulate atmospheric turbulence is the Fourier transform method. Recent studies has shown successful results of propagating a beam through random phase screens, generated through this turbulence model [142–145]. The Fourier power spectrum technique approximates the phase screen as a random phase function

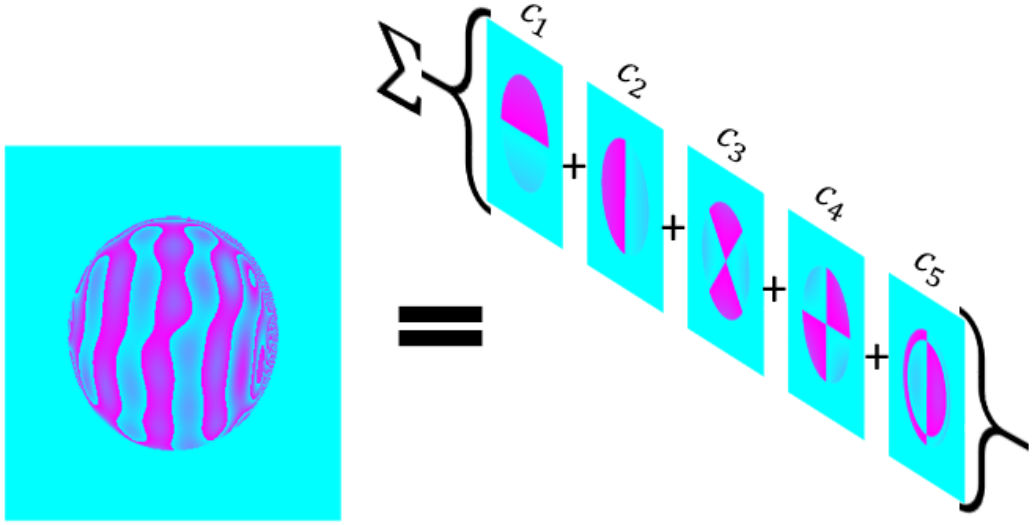


Figure 3-5: A schematic representation of a turbulence phase screen using the Zernike basis. The phase screen shown here is calculated using the sum of the primary aberrations with their weightings (C_{1-5}).

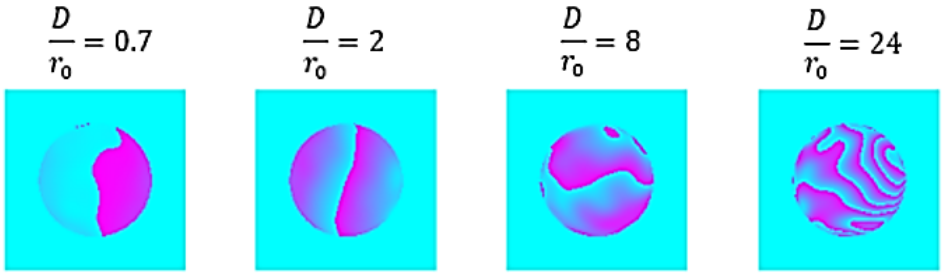


Figure 3-6: Phase profiles of turbulence screens generated via Zernike-polynomials. These phase screens are created through the summation of the Zernike polynomial and the weighting coefficients. These phase screens are generated with different D/r_0 values.

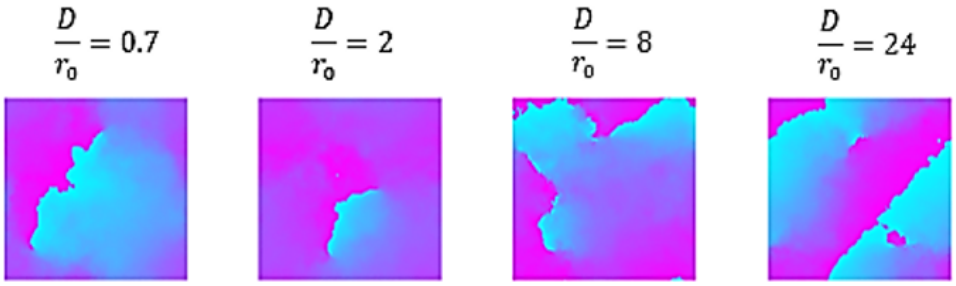


Figure 3-7: Fourier power spectrum phase screens created using random phase screens. These phase screens are generated with different D/r_0 values.

with a variance of [146]

$$\sigma^2(x,y) = \left(\frac{2\pi}{N\Delta x}\right)^2 \Phi(k_x, k_y), \tag{3.10}$$

for an $N \times N$ grid over which the screen is generated. Here Δx is the grid spacing, while k_x and k_y are the spatial frequencies over the grid and $\Phi(k_x, k_y)$ is the phase spectrum given by

$$\Phi(k_x, k_y) = 2\pi k_0^2 L \Phi_n(k_x, k_y). \tag{3.11}$$

The $\Phi_n(k_x, k_y)$ is the refractive index power spectrum, L is the distance over which the screen is simulated for and k_0 is the wave-number (in vacuum) of the optical beam to be used. The desired phase screen can be computed from

$$\psi(x,y) = \mathbb{R}\mathrm{e}\left\{\mathcal{F}^{-1}(\ \mathrm{C}(\mathrm{k_x}, \mathrm{k_y})\sigma(\mathrm{k_x}, \mathrm{k_y})\ )\right\}, \tag{3.12}$$

where, $C(k_x, k_y)$ is a grid of random real numbers ranging from 0 to 1 sampled from a normal distribution with unit variance and 0 mean. The phase screen is computed from the real part of an inverse Fourier transform ($\mathcal{F}^{-1}$). Examples of the phase screens are shown in Fig. 3-7. We varied the coherence length (r_0) and phase screen's aperture (D).

Once the phase functions corresponding to the phase screens are generated. Next, we produce holograms that can be used to imprint the desired perturbation onto an optical beam, using the real-world sonic anemometer data. For example we demonstrate this procedure for liquid crystal displays and DMD devices. Given the phase function, $\psi(x,y)$, a hologram tailored for a phase-only device, can be calculated from [147]

$$H(x,y) = \mathrm{mod}\{\psi(x,y) + n_x x + n_y y, 2\pi\} \tag{3.13}$$

where the factors n_x and n_y are the grating frequencies in the x and y (Cartesian) directions, respectively. The phase depth of the blazed grating was $[0, 2\pi]$. Examples of this are shown in Fig. 3-8 (a) and (c), along with the simulated resulting beam phase and intensity. Some devices can modulate light to up to 8π, which allows

for steeper phase gradients simulation with fewer pixels. The disadvantage of liquid crystal displays is their modulation speed which is typically tens of Hertz. The time scale at which turbulence changes is given by the Greenwood frequency, which is the order of higher magnitude.

For this reason DMDs are ideal: they have modulation speeds of kilohertz, allowing accurate simulation of realistically fast changing turbulence. Unfortunately, DMDs use an amplitude only hologram encoding which limits efficiency: the first diffraction order of a DMD has $< 10\%$ of the initial input power. The desired hologram can be calculated using

$$T(x,y) = \frac{1}{2}\left\{1 + \text{sgn}\left(\cos\left(2\pi\frac{x}{x_0} + \pi p(x,y)\right) - \cos\left(\pi w(x,y)\right)\right)\right\}. \tag{3.14}$$

Since we only consider the phase variations, the amplitude term can simply be set to unity, i.e., $A(x,y) = 1$.

The resulting screens are binary images having zeros and ones as entries. Figure 3-8 (a) shows an example of a DMD and SLM turbulence hologram that was generated with turbulence strengths obtained from the sonic anemometer as examples, along with the resulting beam phase and intensity in Fig 3-8 (c). As shown, the holograms are simply distorted binary gratings. There is no noticeable difference between the hologram patterns. However the far-field intensity patterns are varying in intensity, indicating that the phase distortions encoded on the holograms were successfully transmitted onto the beam. While we do see a variation in the intensity of the fields, we need to calibrate the encoded holograms by optimizing the appropriate parameters so that the encoded and measured turbulence strengths are identical.

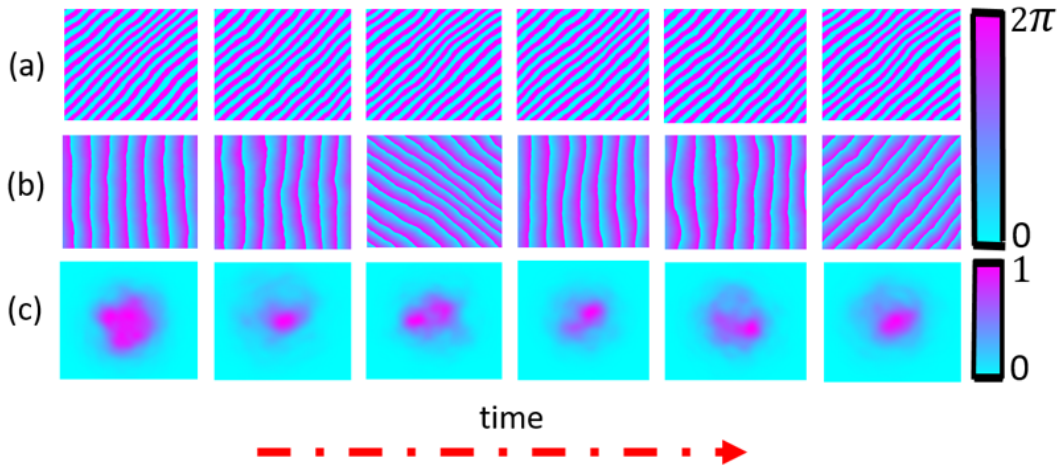


Figure 3-8: (a) Phase profiles of turbulence screens generated via Zernike-polynomials. These phase screens are created for DMDs. (b) Phase profiles of turbulence screens generated via Zernike-polynomials. These phase screens are created for LC displays and are changing with time. (c) Distorted beam profiles over 800 mm distance.

3.1.3 Characterising optical turbulence in the laboratory

Now that we generated some phase screens and were able to produce holograms that can be used to modulate optical beams, how do we quantify the amount of turbulence given the on-axis intensity of the abberated and non-abberated beams? A common quantitative measure is the Strehl Ratio and can be expressed

$$\mathrm{SR} = \frac{I(0)}{I_0(0)} \approx \frac{1}{[1 + (D/r_0)^{5/3}]^{6/5}}. \tag{3.15}$$

which translates as the ratio of the central peak for an unperturbed beam ($I_0(0)$) and the perturbed beam ($I(0)$), where D is the aperture diameter and r_o is the Fried parameter. In the lab these peaks were measured in the far field as an on-axis intensity measurement extracted from the CCD pixel array. Given an image $I(x_i, y_i)$ where (x_i, y_i) are coordinates mapping each pixel, the on-axis intensity is measured with reference to an unperturbed Gaussian beam propagated to the far-field of the DMD. Figure 3-9 shows the calculated Strehl Ratios using the C_n^2 values that were measured

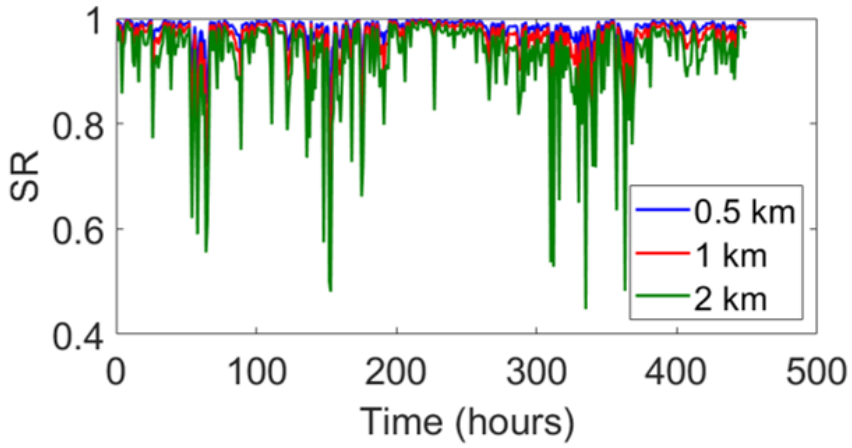


Figure 3-9: Simulated Strehl Ratio with 0.5, 1, 2 km propagation distances.

and plotted in Fig. 3-4. Here, the length of propagation, L, was varied to realise strong turbulence. As shown the SR parameter produces a function scaling from 0 to 1, indicating weak to strong turbulence, respectively. It can be seen that when a laser beam propagates through a short distance it experiences weak turbulence compared to when it propagates through longer distances. We will now show how the DMD can be used to imprint turbulence on optical beams with controllable Strehl ratios and then use the measured C_n^2 from a real-world setting to mimic the same behavior but with simulated holograms.

Firstly, we calibrate the turbulence holograms. It is important to show the relation between the normalised aperture size, D/r_0, and the SR in calibrating phase screens in the lab. Since we want to generate turbulence strengths with a specific coherence length, r_0, we calibrated the system by changing the aperture size argument, D, until the theoretical and experimental SR are equivalent for various values of D/r_0. Figure 3-10 shows a lab setup for using this approach. In the setup, a He-Ne laser beam is dispatched with a near-flat wavefront at the DMD, where turbulence phase screens are displayed in real-time. The DMD was stripped directly from an imaging system which was recently developed for imaging scenes at the CSIR (see the full system in Fig. 3-10 on the far left). A first-order was diffracted by the DMD and imaged by a camera at the far-field of a Fourier lens for various turbulence strengths parameterised by D/r_0. We recorded the on-axis intensity for each image. The Strehl ratio SR was

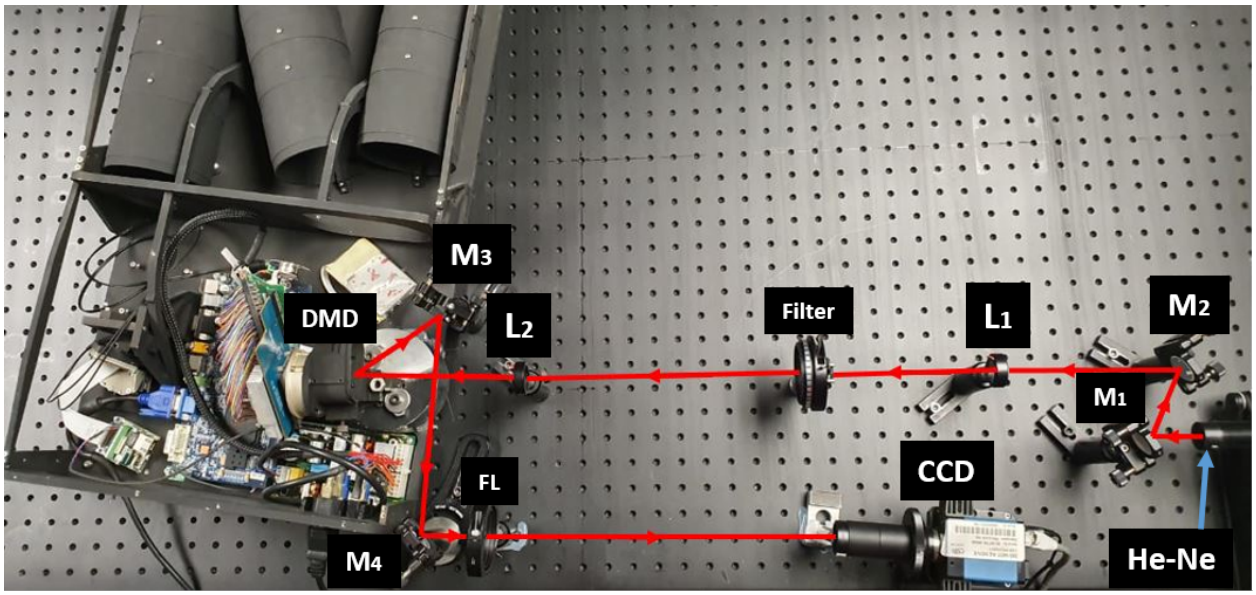


Figure 3-10: Optical beam characterization setup.

calculated from these intensities and then compared to the theory. Figure 3-11 and 3-12 shows the measured SR during the calibration process using the Zernike (Noll) methods and Fourier power spectrum, respectively. Notice that the aperture size here relates to the input Gaussian mode radius by $D = 2w$. In each case we selected a fixed D and scanned through a range of r_0 values while comparing the results to the theory until they were in agreement. The Gaussian beam radius was selected based on the phase screen calibration.

We observed that the two methods, Zernike and power spectrum, both matched when $w = 0.47$. However, the Zernike approach only match the theory when the aperture size is exactly $D = 2w$ otherwise the measured SR deviates significantly from the theory (see Fig.3-11). In contrast, the holograms generated from the power spectrum method filled the entire screen, and therefore the measured SR values were less sensitive to the aperture size although they still needed to be optimised to realise a perfect overlap with the theory.

Now that we have calibrated the holograms, we can use the measured C_n^2 from the sonic anemometer to synthesis turbulence screens. The real-world data that we extracted was larger than the size of the computer that we were using in the laboratory to perform this measurements, so we selected a portion of the data (Region

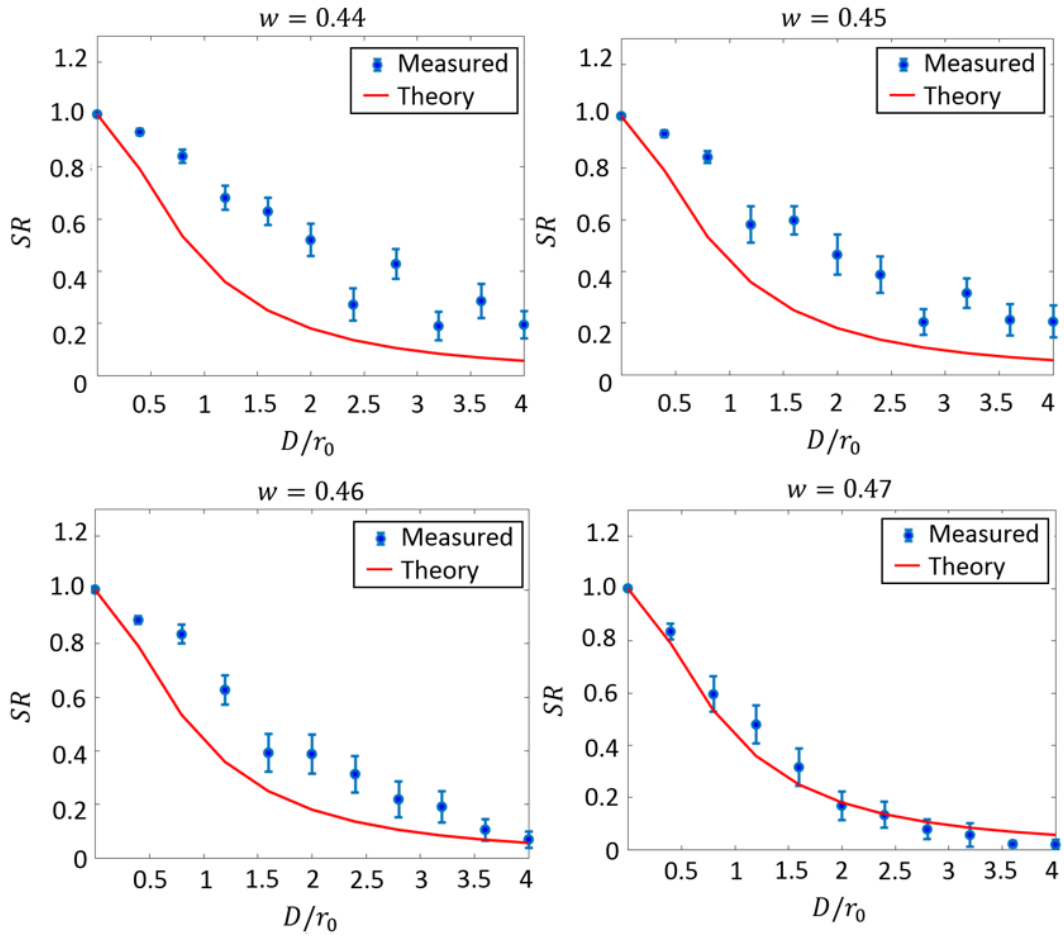


Figure 3-11: Strehl Ratio versus D/r_0 with different aperture size using the Zernike expansion method. It can be seen that when the aperture size is 0.47 mm, the theory agrees with the measured values because the Gaussian beam size match with the encoded beam waist.

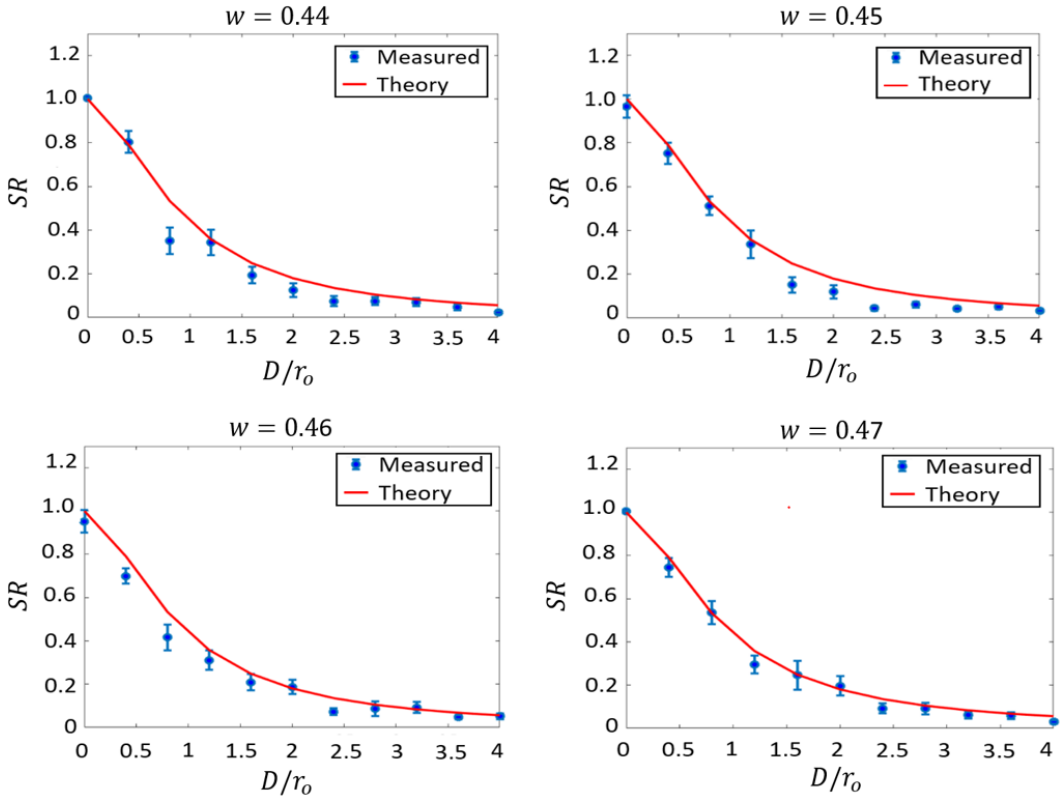


Figure 3-12: Strehl Ratio versus D/r_0 with different aperture size using Fourier power spectrum method. It can be seen that when the aperture size is 0.47 mm, the theory agrees with the measured values.

of Interest (ROI) shown in Fig. 3-9) to test the beam quality with a different turbulence strengths in the lab. Here 30 different samples of each turbulence strength were used. Figure 3-13 and Figure 3-14 show the measured Strehl Ratio from the sonic anemometer data (open circles) and measured (filled circles) from synthesised screens encoded with the same turbulence strengths. The results in Figure 3-13 show that there is almost no turbulence and the theory matches with the experimental results. In this case the beam appears unaffected because a shorter propagation distance ($L = 0.5$ km). However, from the results shown in Fig.3-14, it can be seen that turbulence dominates under long propagation a distance of $L = 2$ km was assumed. Nonetheless, our theoretical and numerical results have a direct bearing in both Fig. 3-13 and 3-14.

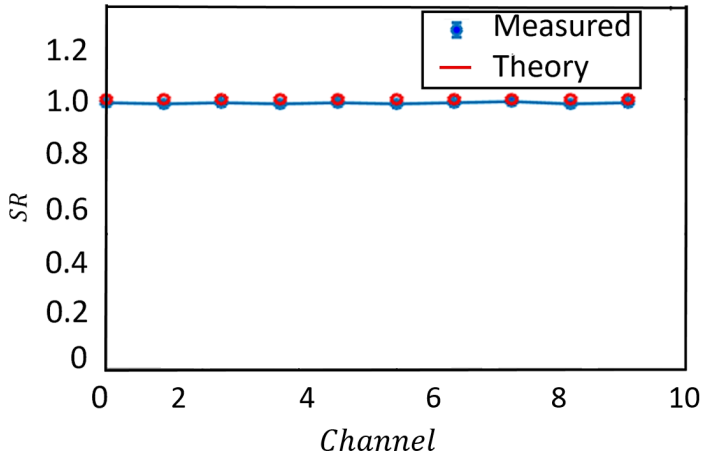


Figure 3-13: Strehl Ratio of a Gaussian beam aberrated by turbulence compared with its theoretical values. Here the propagation distance, L was < 0.5 km. Here the term channel is referred to the number of measured samples.

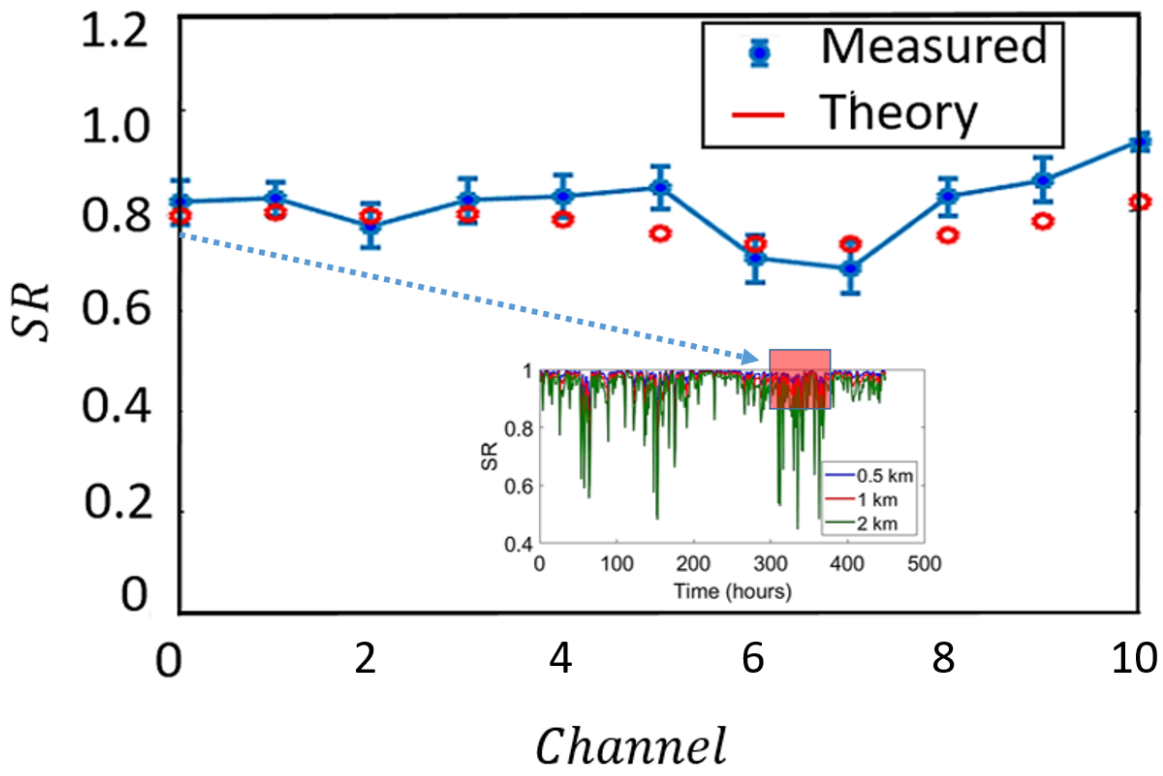


Figure 3-14: Strehl Ratio of a Gaussian beam aberrated by turbulence compared with its theoretical values. Here the propagation distance, L was 2 km. The values of the laboratory results (which is the red and blue results) were selected from the red region of Fig. 3-9, which is the theoretical SR for different propagation distances.

Now that we can experimentally generate and characterize optical turbulence with DMDs, is there a structured light family that is less affected by optical turbulence, where the orthogonality or polarisation is preserved? Different sets of spatial modes have different characteristics and symmetries, which may result in basis-dependent performance in turbulence. In the next section we determine the non-separability states of vector modes using the VQF tool. Moreover, we use this measure to demonstrate the resilience of higher-order OAM entanglement against turbulence. We test this for diverse OAM subspaces.

3.2 The robustness of structured light in turbulence

The work herein is submitted for publication to Physical Review Applied.

In this section, we demonstrate the techniques to generate and characterize optical modes and we show how these modes can be affected by turbulence. We particularly focus on vector modes. Moreover we demonstrate the resilience of higher order OAM modes against turbulence.

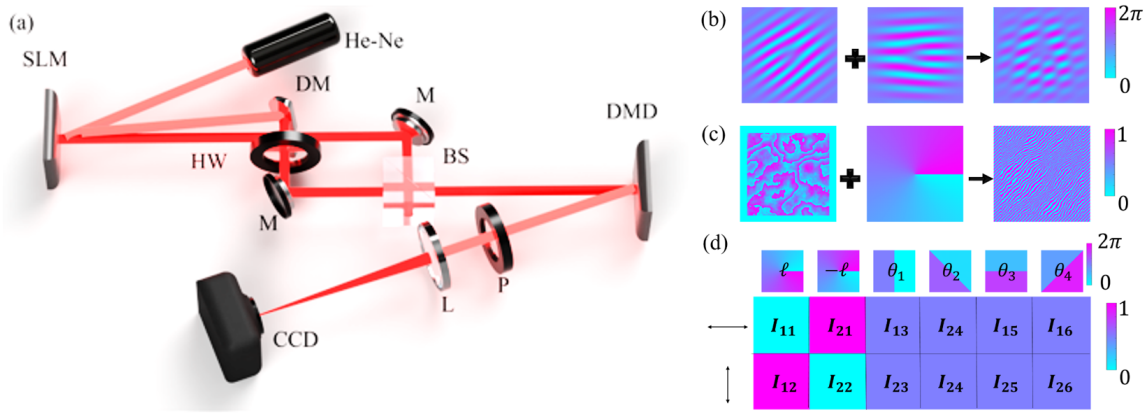


Figure 3-15: (a) An illustration of the experimental setup. A Helium Neon (He-Ne) laser was expanded and collimated onto a spatial light modulator (SLM). Two modes were generated simultaneously from the SLM and were then separated using a D-shaped mirror (DM) and recombined with a beam splitter (BS). The recombined modes were imaged to the digital micromirror device (DMD), where the turbulence was encoded in combination with the detection holograms. The resulting modes were propagated to the DMD's Fourier plane with a 500 mm Fourier lens (L), where the on-axis intensity measurements were performed.

To generate and detect vector beams through turbulence we used Fig. 3-15 (a). In the setup, we used a Helium-Neon (He-Ne) laser with a central wavelength of 633 nm and collimated Gaussian beam profile. We modulated the He-Ne laser beam using a Phase-only Holo-Eye Pluto liquid crystal (LC) display. On the LC, we encoded a multiplexed hologram by combining two orthogonal OAM modes of charges $\pm\ell$ having distinct spatial frequencies [101]. The amplitudes and phases of each mode

were encoded using the Arrizon technique [96]. The vector vortex modes we generated were in the form

$$\Psi_\ell(\mathbf{r}) = u_{-\ell}(r)\exp(-\ell\phi)\hat{e}_V + u_\ell(r)\exp(\ell\phi)\hat{e}_H. \tag{3.16}$$

where the vertical ($\hat{e}_V$) and horizontal ($\hat{e}_H$) polarisation modes are coupled to spatial OAM modes distinguished by their topological charge $\pm\ell$. For example, to obtain the state $\Psi_{\ell=1,10}$, we encoded two multiplexed holograms [101] with Laguerre-Gaussian (LG) modes of charges $\ell = -1(-10)$ and $\ell = 1(10)$ having distinct carrier frequencies (gratings) and separated them in path using a D shaped mirror. An example of the holograms is shown in Fig. 3-15 (b).

Before interfering the two beams on the BS, we rotated the polarisation of the reflected beam from the D-shape mirror by 90° using a half wave-plate. This converted the polarisation from H to V. The two beams now had orthogonal polarisations. After combining the two beams, the resulting vector beam was transmitted to the DMD. On the DMD we encoded Kolmogorov turbulence phase screens following [135] (see Chapter 2 for complete method description) in combination with the detection holograms necessary for the VQF measurements. An example of the detection hologram is shown in Fig. 3-15 (c). The VQF holograms all had phase profiles shown in the first row of Fig. 3-15 (d). The combination of the detection and turbulence encoded hologram resulted in a noisy detection hologram that has both the noise and the desired projection mode. Examples of the intensities which were generated using holograms propagated through, the noisy channel are shown in Fig. 3-16. In the results, we showed both scalar and vector beams.

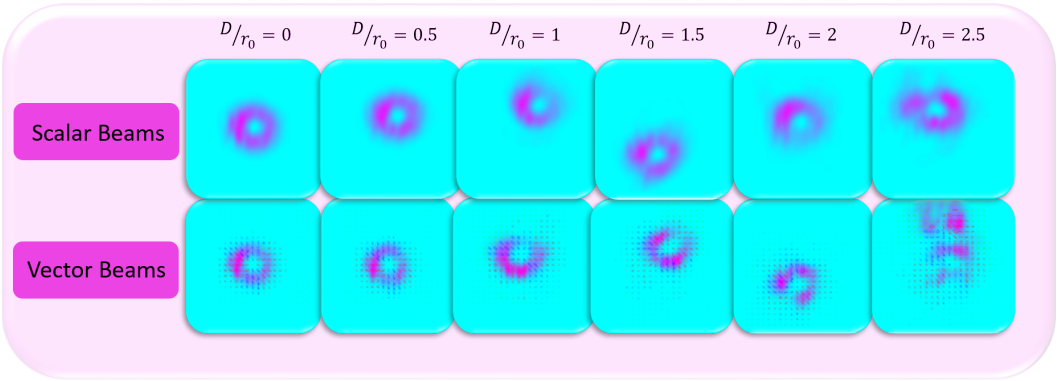


Figure 3-16: Pure scalar (Top) and vector vortex (Bottom) intensities propagated through varying turbulence strength. The results show that the intensities vary from turbulence to no turbulence.

We had a polariser to project onto the H and V polarisation modes after the DMD. The resulting field was then propagated to the far field using a Fourier lens (FL) and an on axis measurement of the intensity was recorded, providing the modal overlap of the input state, the simulated turbulence and the detection mode [148]. For each measurement we prepared up to 30 instances of each turbulence strength for D/r_o=2.5 and 3.5. That is, 30 random phase screens of the same turbulence strength were generated. An example of measurements for intensities I_{uv} is shown in Fig. 3-15 (d). The columns correspond to the spatial projections while the rows correspond to the polarisation measurements.

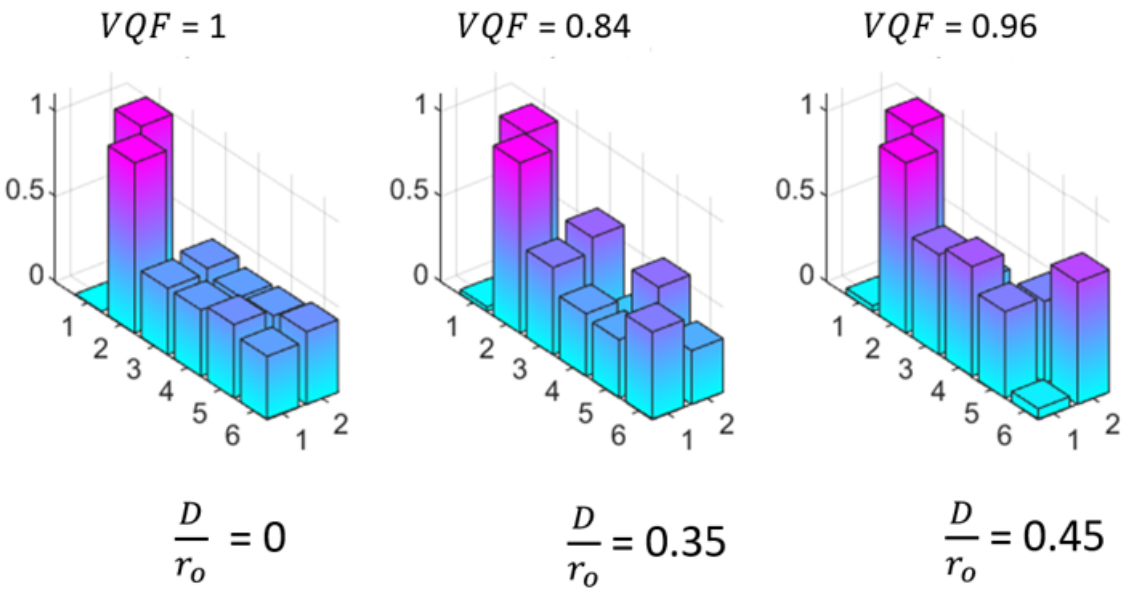


Figure 3-17: Vector Quality Factor measurements with varying D/r_0. The VQF tool measures the components from purely scalar (0) to purely vector (1).

3.2.1 Confirming the factorisation relation.

We first calibrated the system using free space measurements. From these results we could map the input concurrence (VQF) of each mode. To achieve this we varied the relative amplitude of the orthogonal modes on the hologram for generating the multiplexed beam such as to control the VQF of the input mode. Subsequently we measured the non-separability of each of the modes of varying concurrence under turbulence conditions of $D/r_o = 2.5$ and 3.5. The results are shown in Fig. 3-18 (a) and (b) for subspaces $\ell = 1$ (circles) and $\ell = \pm 10$ (squares). The error-bars are smaller than the points.

The gradient of the slopes is indicative of the evolution of mixing of beams: in the absence of turbulence the plots would have a strictly diagonal line following the relation $VQF_{out} = VQF_{in}$, intersecting points (0,0) and (1,1) for a separable and entangled state, respectively. However, in the presence of turbulence the trends follows the relation $VQF_{out} = VQF_{\Psi} \times VQF_{in}$ but still intersects (0,0), meaning that the separable state always maps to a separable state because there is no interaction. Importantly, the slope of the line is determined by VQF_{Ψ}, being the VQF (concurrence)

of the maximally non-separable state, in agreement with [149]. As shown, the resulting concurrence of any input state is constrained by the line connecting the output of a separable and maximally entangled state.

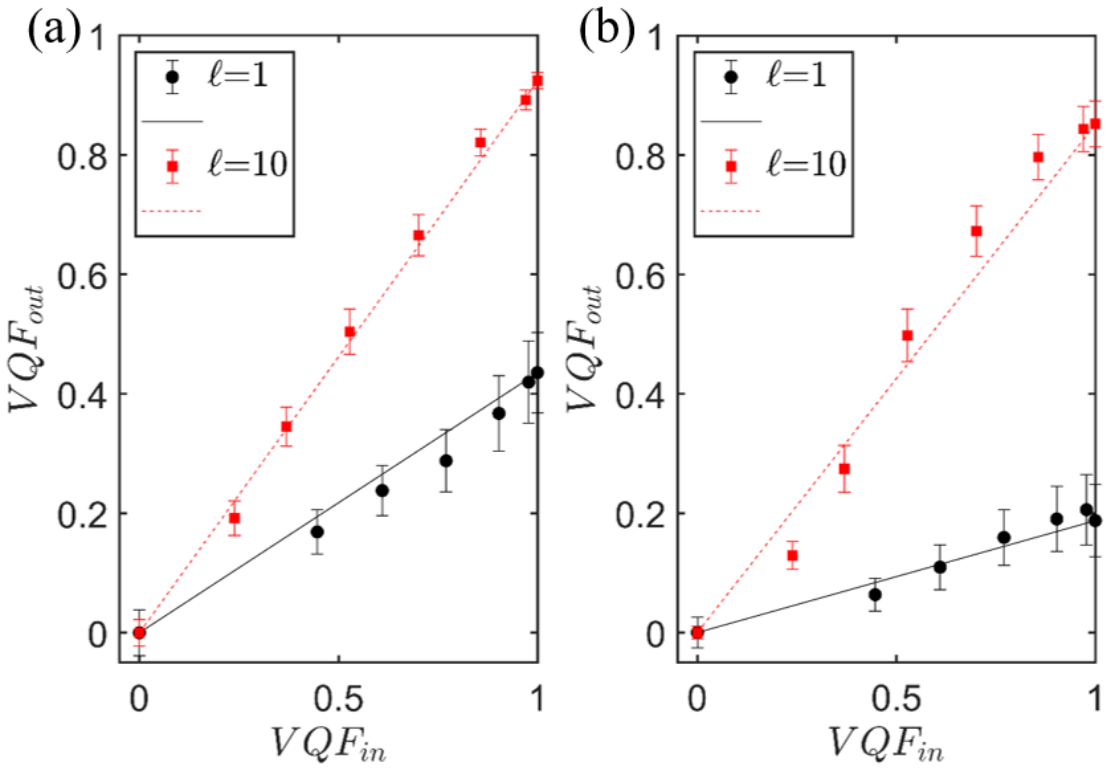


Figure 3-18: Experimental results for the degree of entanglement (VQF or equivalently concurrence) of the input vector mode vs the output mode under the effect of turbulence strengths of $D/r_0 = 2.5$ (a) and 3.5 (b). The circles are for vector modes in the subspace of $\ell = 1$ and squares are for $\ell = 10$. The Vertical error-bars are smaller than the points. The points were obtained from measurements with 30 realisations of the same turbulence strengths.

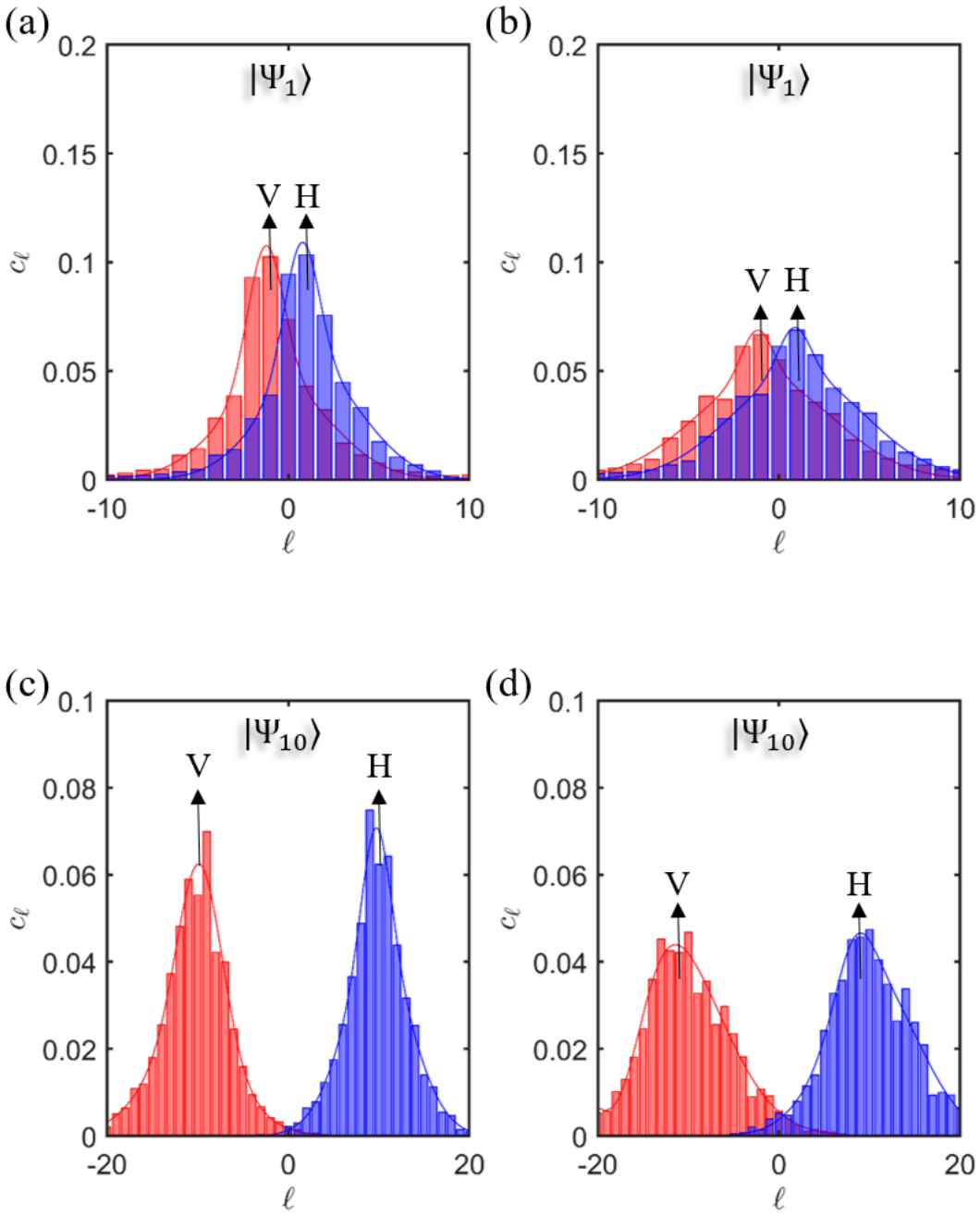


Figure 3-19: Measured modal spectrum for the vertical and horizontal polarised spatial modes. (a, c) and (b, d) were measured for cases when $D/r_0 = 2.5$ (right column) and 3.5 (left column), respectively. The top row was measured for $\ell = 1$ subspace and the bottom row for the $\ell = 10$ subspace. Each bar is an average of 30 realisations of the same turbulence strength. In each plot, the distribution on the right corresponds the horizontally polarised mode (blue) while the distribution on the left (red) corresponds to the vertically polarised mode. As expected, the mode distribution is symmetric about $|\ell|$, consistent with the theoretical distribution shown as lines

3.2.2 Robustness for higher order modes

We investigated the modal distribution for each of the turbulence strengths on the orthogonal components of each vector mode. The modal distributions are illustrated in Fig 3-19. Here, the distribution on the right corresponds the Horizontally polarised mode while the distribution on the left corresponds to the Vertically polarised mode. As expected, the mode distribution is centered at the input OAM mode. Moreover as we introduce turbulence, the modes in Fig 3-19 (c) and (d) for $|\ell| = 1$ and $|\ell| = 10$, respectively, couple into adjacent modes. Note that here, there is no coupling between $\ell = \pm 10$ while $|\ell| = 1$ shows significant coupling to avoid cutting of the OAM. This was done by removing the aperture. Further by increasing the turbulence strength to $D/r_o = 3.5$ more coupling is observed though $\ell = 10$ still maintains minimal coupling.

A closer look at Fig. 3-18 (a) $\ell = \pm 1$ subspace shows a significant decrease in VQF due to the inter modal coupling (spreading of energy) within the $\ell = \pm 1$ subspace shown in Fig. 3-19 (a). We point out that the concurrence of every other input state with a varying degree of nonseparability lies on the curve, connecting the concurrence of the maximum entangled state and a purely separable state, as expected. To compare the $\ell = 1$ and $\ell = 10$ nonseparable modes, we observe the slopes. Evidently the $\ell = 10$ maintains a higher slope. This is due to the large separation of the modes in the $\ell = \pm 10$ subspace ($\Delta\ell = 20$).

We went further and increased the turbulence strength to $D/r_o = 3.5$. The results are depicted in Fig 3-18 (b). The $\ell = 1$ subspace showed a higher decrease in nonseparability while $\ell = 10$ maintained a degree of nonseparability above VQF=0.8, still close to 1 (for a perfectly maximally entangled state). These results are consistent with findings in [78] where the entanglement decay was shown to be more rapid in lower order OAM entangled subspaces. Our results also expand on the work performed in [132] showing the equivalence quantum and classical non-separability of entangled photons and vector modes, respectively.

3.3 Conclusions

In this Chapter we described the operation of a sonic anemometer and we clarified the steps for calculating the velocity of the airflow using the time-of-flight theory. We clarified the purpose of the data obtained by the instrument, that it is useful in generating turbulence phase screens. We demonstrated the steps required to derive the phase structure of turbulence from fluid flow. We developed an experimental testbed for laboratory demonstration and we characterized the optical effects caused by turbulence. We employed DMDs to execute turbulence. Furthermore, we generated scalar or vector beams (through multiplexing method), by loading a computer generated hologram into a liquid crystal display and we detected these modes using a DMD. We demonstrated and characterized the propagation of these optical beams through turbulence and free-space channels. Moreover, we demonstrated the importance of studying entanglement using classical light. Through this technique, we investigated the contribution of mode separation on the non-separability to demonstrate robustness for higher order OAM state spaces. Furthermore, we demonstrated the robustness of large OAM modes through turbulent atmosphere.

Chapter 4

Conclusion and future work

In this dissertation, we developed techniques for characterising outdoor turbulence and synthesising some of its properties in the laboratory environment. With these techniques we were able to study its effects on optical laser beams as well as its impact on imaging systems.

In Chapter 1, we introduced the theoretical concepts that prepare the reader for the body of work explored in this dissertation. We introduced transverse spatial modes of light, particularly those that carry orbital angular momentum, because they are natural solutions of laser beams in free-space. Such beams are commonly used to study the impact of turbulence on imaging and optical free-space communication systems. We also introduced Kolmogorov's statistical theory of turbulence, a well established, intuitive and widely use concept for studying and characterising turbulence. The theory explored the influence of large turbulent cells on the laser beam resulting in distorted wavefronts. We also discussed a technique that became useful to calculate the effects of turbulence on optical systems. We saw that it is possible to extract velocity of the airflow from this instrument, known as a sonic anemometer, and that this velocity data can be converted to a refractive index structure function.

In Chapter 2, we introduced the experimental techniques that were required generating and controlling optical laser beams. This included harnessing techniques for generating and detecting optical beams that carry orbital angular momentum by making use of digital micromirror devices and liquid crystal displays. We first gave an

introduction on how these devices work and we have shown some standard techniques for using them. We tested the performance of the spatial modulators using optical beams. These techniques not only formed the main tools for generating light fields but later, in Chapter 3, formed the part of our methods used for synthesis turbulence in the laboratory and imprinting it on laser beams. We also introduced a detection tool called correlation method, to characterize optical beams that propagates in vacuum. Furthermore, we demonstrated the generation of vector modes using liquid crystal displays via multiplexing approach in an interferometer. Lastly, we demonstrated a technique, called the vector quality factor (VQF) for characterising vector beams. This technique became useful in Chapter 3, for showing the disparity between purely scalar and vector beams.

In Chapter 3, we demonstrated the operation of a sonic anemometer and we discussed steps for calculating the velocity of the airflow using the time-of-flight theory. We extracted turbulence parameters from the velocities of the sonic anemometer data in-order to simulate turbulence by encoding its phase fluctuations onto digital screens while possessing the same statistical properties that we measured from the anemometer. To achieve this, we developed an experimental testbed to characterize real-world turbulence in the laboratory making use of the generated phase screens. The phase screens were generated using Zernike polynomials as well as the Fourier-Transform power spectrum method. The two methods are commonly used for simulating optical turbulence. We found that the measured experimental data for optical turbulence using the sonic anemometer could be accurately simulated using our phase screens; the measured turbulence strength was in good agreement with the theory predictions.

Lastly, we generated scalar and vector beams via methods developed in Chapter 2, by loading a computer generated hologram into a liquid crystal display and interfering the resulting orders. We then detected these modes using a DMD. We demonstrated and characterized the propagation of these optical beams through turbulence. Moreover, we demonstrated the importance of studying entanglement-like features (VQF, see Chapter 2) in classical laser beams, i.e, vector modes. In particularly, we stud-

ied how the VQF (nonseparability) is affected by turbulence using the synthesised turbulence screens that were developed with techniques from Chapter 2. The results showed that depending on the mode order, the OAM content in the vector modes can scatter. In higher order modes (large OAM), the scattering does not impact the VQF as much as it does lower order modes (lower OAM). This suggests that there may be some robustness in the VQF of high-order vector beams in turbulence.

Since we are now able to demonstrate real-world turbulence in the laboratory and have studied some of its effects on optical modes, in future research, we may consider propagating such laser beams through realistic free-space channels. It may be interesting to also synthesise the turbulence screens at higher speeds since we only considered single instances of each phase screen realisation based on the measured data from the anemometer. Therefore, further improvements to the work can be made. Furthermore, our study of the vectors modes in turbulence open up new avenues of research ranging from correction of the phase fluctuations in optical fields due to turbulence, to the development of better ways for characterising its effects on both classical and quantum systems.

Bibliography

[1] L. C. Andrews, R. L. Phillips, and C. Y. Hopen, *Laser beam scintillation with applications*, vol. 99. SPIE press, 2001.

[2] V. N. Mahajan and J. A. Díaz, "Imaging characteristics of zernike and annular polynomial aberrations," *Applied Optics*, vol. 52, no. 10, pp. 2062–2074, 2013.

[3] Andrews, *Laser Beam Propagation through Random Media*. SPIE Press, second ed., 2005.

[4] N. Kopeika, I. Dror, and D. Sadot, "Causes of atmospheric blur: comment on atmospheric scattering effect on spatial resolution of imaging systems," *JOSA A*, vol. 15, no. 12, pp. 3097–3106, 1998.

[5] R. Hufnagel and N. Stanley, "Modulation transfer function associated with image transmission through turbulent media," *JOSA*, vol. 54, no. 1, pp. 52–61, 1964.

[6] N. S. Kopeika and D. Arbel, "Imaging through the atmosphere: an overview," in *Optical Pulse and Beam Propagation*, vol. 3609, pp. 78–89, International Society for Optics and Photonics, 1999.

[7] K. K. Halder, M. Tahtali, and S. G. Anavatti, "Turbulence mitigation and moving object detection for underwater imaging," in *2015 International Conference on Optical Instruments and Technology: Optoelectronic Imaging and Processing Technology*, vol. 9622, p. 96220C, International Society for Optics and Photonics, 2015.

[8] R. R. Beland, "Propagation through atmospheric optical turbulence," *Atmospheric Propagation of Radiation*, vol. 2, pp. 157–232, 1993.

[9] L. C. Andrews and R. L. Phillips, *Laser beam propagation through random media*, vol. 152. SPIE press Bellingham, WA, 2005.

[10] E. Masciadri, J. Vernin, and P. Bougeault, "3D numerical simulations of optical turbulence at the roque de los muchachos observatory using the atmospherical model meso-nh," *Astronomy & Astrophysics*, vol. 365, no. 3, pp. 699–708, 2001.

[11] A. Kellerer, N. Gorceix, J. Marino, W. Cao, and P. Goode, "Profiles of the daytime atmospheric turbulence above big bear solar observatory," *Astronomy & Astrophysics*, vol. 542, p. A2, 2012.

[12] L. Bolbasova, A. Y. Shikhovtsev, E. Kopylov, A. Selin, V. Lukin, and P. Kovadlo, "Daytime optical turbulence and wind speed distributions at the baikal astrophysical observatory," *Monthly Notices of the Royal Astronomical Society*, vol. 482, no. 2, pp. 2619–2626, 2019.

[13] X. Zhu and J. M. Kahn, "Free-space optical communication through atmospheric turbulence channels," *IEEE Transactions on Communications*, vol. 50, no. 8, pp. 1293–1300, 2002.

[14] C. Paterson, "Atmospheric turbulence and orbital angular momentum of single photons for optical communication," *Physical Review Letters*, vol. 94, no. 15, p. 153901, 2005.

[15] J. Shapiro, "Imaging and optical communication through atmospheric turbulence," in *Laser Beam Propagation in the Atmosphere*, pp. 171–222, Springer, 1978.

[16] J. Schmidt, "Numerical simulation of optical wave propagation with examples in matlab," Society of Photo-Optical Instrumentation Engineers, 2010.

[17] T. J. Schulz, "Optimal beams for propagation through random media," *Optics Letters*, vol. 30, no. 10, pp. 1093–1095, 2005.

[18] R. Frehlich, "Simulation of laser propagation in a turbulent atmosphere," *Applied Optics*, vol. 39, no. 3, pp. 393–397, 2000.

[19] G. Gbur and E. Wolf, "Spreading of partially coherent beams in random media," *JOSA A*, vol. 19, no. 8, pp. 1592–1598, 2002.

[20] J. F. de Boer, M. P. van Albada, and A. Lagendijk, "Transmission and intensity correlations in wave propagation through random media," *Physical Review B*, vol. 45, no. 2, p. 658, 1992.

[21] Y. A. Kravtsov, "New effects in wave propagation and scattering in random media (a mini review)," *Applied Optics*, vol. 32, no. 15, pp. 2681–2691, 1993.

[22] T. Coakley, "Turbulence modeling methods for the compressible navier-stokes equations," in *Danvers, MA, USA, 16th Fluid and Plasmadynamics Conference*, p. 1693, 1983.

[23] B. Birnir, "The Kolmogorov–Obukhov statistical theory of turbulence," *Journal of Nonlinear Science*, vol. 23, pp. 657–688, Aug 2013.

[24] T.-i. Wang, G. Ochs, and S. Clifford, "A saturation-resistant optical scintillometer to measure cn2," *JOSA*, vol. 68, no. 3, pp. 334–338, 1978.

[25] E. L. Andreas, "Estimating c_n^2 over snow and sea ice from meteorological data," *JOSA A*, vol. 5, no. 4, pp. 481–495, 1988.

[26] B. Birnir, "The kolmogorov obukhov statistical theory of turbulence," *Journal of Nonlinear Science*, vol. 23, no. 4, pp. 657–688, 2013.

[27] M. Hui, A. Larsen, and H. Xiang, "Wind turbulence characteristics study at the stonecutters bridge site: Part i—mean wind and turbulence intensities," *Journal of Wind Engineering and Industrial Aerodynamics*, vol. 97, no. 1, pp. 22–36, 2009.

[28] N. Kato, T. Ohkuma, J. Kim, H. Marukawa, and Y. Niihori, "Full scale measurements of wind velocity in two urban areas using an ultrasonic anemometer," *Journal of Wind Engineering and Industrial Aerodynamics*, vol. 41, no. 1-3, pp. 67–78, 1992.

[29] O. Keskin, L. Jolissaint, and C. Bradley, "Hot-air optical turbulence generator for the testing of adaptive optics systems: principles and characterization," *Applied Optics*, vol. 45, no. 20, pp. 4888–4897, 2006.

[30] D. J. Butler, S. Hippler, S. Egner, W. Xu, and J. Bähr, "Broadband, static wavefront generation: Na-ag ion-exchange phase screens and telescope emulation," *Applied Optics*, vol. 43, no. 14, pp. 2813–2823, 2004.

[31] L. Burger, I. Litvin, and A. Forbes, "Simulating atmospheric turbulence using a phase-only spatial light modulator," *South African Journal of Science*, vol. 104, 03 2008.

[32] J. Sasian and E. Acosta, "Generation of spherical aberration with axially translating phase plates via extrinsic aberration," *Optics Express*, vol. 22, no. 1, pp. 289–294, 2014.

[33] T. Xu, Y. Li, W. Du, C. Ma, S. Cai, M. Lan, J. Wu, S. Yu, and J. Lin, "Simulating atmospheric turbulence using a spatial light modulator based on fourier transform," in *2014 Conference on Lasers and Electro-Optics (CLEO)-Laser Science to Photonic Applications*, pp. 1–2, IEEE, 2014.

[34] J. D. Phillips, M. E. Goda, and J. Schmidt, "Atmospheric turbulence simulation using liquid crystal spatial light modulators," in *Advanced Wavefront Control: Methods, Devices, and Applications III*, vol. 5894, p. 589406, International Society for Optics and Photonics, 2005.

[35] E. Anzuola and A. Belmonte, "Generation of atmospheric wavefronts using binary micromirror arrays," *Applied Optics*, vol. 55, no. 11, pp. 3039–3044, 2016.

[36] J.-M. Conan, G. Rousset, and P.-Y. Madec, "Wave-front temporal spectra in high-resolution imaging through turbulence," *JOSA A*, vol. 12, no. 7, pp. 1559–1570, 1995.

[37] S. Ramachandran, P. Kristensen, and M. F. Yan, "Generation and propagation of radially polarized beams in optical fibers," *Optics Letters*, vol. 34, no. 16, pp. 2525–2527, 2009.

[38] J. Noda, K. Okamoto, and Y. Sasaki, "Polarization-maintaining fibers and their applications," *Journal of Lightwave Technology*, vol. 4, no. 8, pp. 1071–1089, 1986.

[39] I. Kaminow, "Polarization in optical fibers," *IEEE Journal of Quantum Electronics*, vol. 17, no. 1, pp. 15–22, 1981.

[40] A. F. Gmitro and D. Aziz, "Confocal microscopy through a fiber-optic imaging bundle," *Optics Letters*, vol. 18, no. 8, pp. 565–567, 1993.

[41] W. Groner, J. W. Winkelman, A. G. Harris, C. Ince, G. J. Bouma, K. Messmer, and R. G. Nadeau, "Orthogonal polarization spectral imaging: a new method for study of the microcirculation," *Nature Medicine*, vol. 5, no. 10, pp. 1209–1212, 1999.

[42] C. Zhang, B. Zhao, and B. Xiangli, "Wide-field-of-view polarization interference imaging spectrometer," *Applied Optics*, vol. 43, no. 33, pp. 6090–6094, 2004.

[43] E. Collett, "Field guide to polarization," SPIE Bellingham, WA, 2005.

[44] D. L. Andrews and M. Babiker, *The angular momentum of light*. Cambridge University Press, 2012.

[45] G. Siviloglou, J. Broky, A. Dogariu, and D. Christodoulides, "Observation of accelerating airy beams," *Physical Review Letters*, vol. 99, no. 21, p. 213901, 2007.

[46] Q. Zhan, "Cylindrical vector beams: from mathematical concepts to applications," *Advances in Optics and Photonics*, vol. 1, no. 1, pp. 1–57, 2009.

[47] T. G. Brown, "Unconventional polarization states: beam propagation, focusing, and imaging," in *Progress in Optics*, vol. 56, pp. 81–129, Elsevier, 2011.

[48] E. Galvez, "Vector beams in free space," *The Angular Momentum of Light*, pp. 51–70, 2012.

[49] B. Ndagano, I. Nape, M. A. Cox, C. Rosales-Guzman, and A. Forbes, "Creation and detection of vector vortex modes for classical and quantum communication," *Journal of Lightwave Technology*, vol. 36, no. 2, pp. 292–301, 2017.

[50] Y. Kozawa and S. Sato, "Optical trapping of micrometer-sized dielectric particles by cylindrical vector beams," *Optics Express*, vol. 18, no. 10, pp. 10828–10833, 2010.

[51] M. Donato, S. Vasi, R. Sayed, P. Jones, F. Bonaccorso, A. Ferrari, P. Gucciardi, and O. Maragò, "Optical trapping of nanotubes with cylindrical vector beams," *Optics Letters*, vol. 37, no. 16, pp. 3381–3383, 2012.

[52] P. Török and P. Munro, "The use of gauss-laguerre vector beams in sted microscopy," *Optics Express*, vol. 12, no. 15, pp. 3605–3617, 2004.

[53] G. Milione, M. P. Lavery, H. Huang, Y. Ren, G. Xie, T. A. Nguyen, E. Karimi, L. Marrucci, D. A. Nolan, R. R. Alfano, *et al.*, "4× 20 gbit/s mode division multiplexing over free space using vector modes and a q-plate mode (de) multiplexer," *Optics Letters*, vol. 40, no. 9, pp. 1980–1983, 2015.

[54] A. Wang, L. Zhu, J. Liu, C. Du, Q. Mo, and J. Wang, "Demonstration of hybrid orbital angular momentum multiplexing and time-division multiplexing passive optical network," *Optics Express*, vol. 23, no. 23, pp. 29457–29466, 2015.

[55] G. Vallone, V. D'Ambrosio, A. Sponselli, S. Slussarenko, L. Marrucci, F. Sciarrino, and P. Villoresi, "Free-space quantum key distribution by rotation-

invariant twisted photons," *Physical Review Letters*, vol. 113, no. 6, p. 060503, 2014.

[56] A. Sit, F. Bouchard, R. Fickler, J. Gagnon-Bischoff, H. Larocque, K. Heshami, D. Elser, C. Peuntinger, K. Günthner, B. Heim, *et al.*, "High-dimensional intracity quantum cryptography with structured photons," *Optica*, vol. 4, no. 9, pp. 1006–1010, 2017.

[57] I. Nape, E. Otte, A. Vallés, C. Rosales-Guzmán, F. Cardano, C. Denz, and A. Forbes, "Self-healing high-dimensional quantum key distribution using hybrid spin-orbit bessel states," *Optics Express*, vol. 26, no. 21, pp. 26946–26960, 2018.

[58] Y. Mushiake, K. Matsumura, and N. Nakajima, "Generation of radially polarized optical beam mode by laser oscillation," *Proceedings of the IEEE*, vol. 60, no. 9, pp. 1107–1109, 1972.

[59] G. Volpe and D. Petrov, "Generation of cylindrical vector beams with few-mode fibers excited by laguerre–gaussian beams," *Optics Communications*, vol. 237, no. 1-3, pp. 89–95, 2004.

[60] M. McLaren, T. Konrad, and A. Forbes, "Measuring the nonseparability of vector vortex beams," *Physical Review A*, vol. 92, no. 2, p. 023833, 2015.

[61] R. Horodecki, P. Horodecki, M. Horodecki, and K. Horodecki, "Quantum entanglement," *Reviews of Modern Physics*, vol. 81, no. 2, p. 865, 2009.

[62] E. Otte, C. Rosales-Guzmán, B. Ndagano, C. Denz, and A. Forbes, "Entanglement beating in free space through spin–orbit coupling," *Light: Science & Applications*, vol. 7, no. 5, pp. 18009–18009, 2018.

[63] A. Selyem, C. Rosales-Guzmán, S. Croke, A. Forbes, and S. Franke-Arnold, "Basis-independent tomography and nonseparability witnesses of pure complex vectorial light fields by stokes projections," *Physical Review A*, vol. 100, no. 6, p. 063842, 2019.

[64] E. Otte, I. Nape, C. Rosales-Guzmán, A. Vallés, C. Denz, and A. Forbes, "Recovery of nonseparability in self-healing vector bessel beams," *Physical Review A*, vol. 98, no. 5, p. 053818, 2018.

[65] A. Forbes, A. Aiello, and B. Ndagano, "Classically entangled light," *Progress in Optics*, vol. 64, p. 99, 2019.

[66] M. A. Cox, C. Rosales-Guzmán, M. P. J. Lavery, D. J. Versfeld, and A. Forbes, "On the resilience of scalar and vector vortex modes in turbulence," *Optics Express*, vol. 24, pp. 18105–18113, Aug 2016.

[67] M. A. Cox, C. Rosales-Guzmán, M. P. Lavery, D. J. Versfeld, and A. Forbes, "On the resilience of scalar and vector vortex modes in turbulence," *Optics Express*, vol. 24, no. 16, pp. 18105–18113, 2016.

[68] C. K. Batchelor and G. Batchelor, *An introduction to fluid dynamics*. Cambridge university press, 2000.

[69] T. E. Faber, *Fluid dynamics for physicists*. Cambridge university press, 1995.

[70] G. K. Vallis, *Atmospheric and oceanic fluid dynamics*. Cambridge University Press, 2017.

[71] F. M. White and I. Corfield, *Viscous fluid flow*, vol. 3. McGraw-Hill New York, 2006.

[72] J. Happel and H. Brenner, *Low Reynolds number hydrodynamics: with special applications to particulate media*, vol. 1. Springer Science & Business Media, 2012.

[73] E. M. Purcell, "Life at low reynolds number," *American Journal of Physics*, vol. 45, no. 1, pp. 3–11, 1977.

[74] M. Irani, B. Rousso, and S. Peleg, *Recovery of ego-motion using image stabilization*. Leibniz Center for Research in Computer Science, 1993.

[75] S. Erturk, "Digital image stabilization with sub-image phase correlation based global motion estimation," *IEEE Transactions on Consumer Electronics*, vol. 49, no. 4, pp. 1320–1325, 2003.

[76] C. Morimoto and R. Chellappa, "Evaluation of image stabilization algorithms," in *Proceedings of the 1998 IEEE International Conference on Acoustics, Speech and Signal Processing, ICASSP'98 (Cat. No. 98CH36181)*, vol. 5, pp. 2789–2792, IEEE, 1998.

[77] F. Vella, A. Castorina, M. Mancuso, and G. Messina, "Digital image stabilization by adaptive block motion vectors filtering," *IEEE Transactions on Consumer Electronics*, vol. 48, no. 3, pp. 796–801, 2002.

[78] A. H. Ibrahim, F. S. Roux, M. McLaren, T. Konrad, and A. Forbes, "Orbital-angular-momentum entanglement in turbulence," *Physical Review A*, vol. 88, no. 1, p. 012312, 2013.

[79] J. P. Zbilut and N. Marwan, "The wiener–khinchin theorem and recurrence quantification," *Physics Letters A*, vol. 372, no. 44, pp. 6622–6626, 2008.

[80] R. Lane, A. Glindemann, J. Dainty, *et al.*, "Simulation of a kolmogorov phase screen," *Waves in Random Media*, vol. 2, no. 3, pp. 209–224, 1992.

[81] K. McAneney, A. Green, and M. Astill, "Large-aperture scintillometry: the homogeneous case," *Agricultural and Forest Meteorology*, vol. 76, no. 3-4, pp. 149–162, 1995.

[82] A. Guyot, J.-M. Cohard, S. Anquetin, and S. Galle, "Long-term observations of turbulent fluxes over heterogeneous vegetation using scintillometry and additional observations: A contribution to amma under sudano-sahelian climate," *Agricultural and Forest Meteorology*, vol. 154, pp. 84–98, 2012.

[83] B. Hunt, W. Fright, and R. Bates, "Analysis of the shift-and-add method for imaging through turbulent media," *JOSA*, vol. 73, no. 4, pp. 456–465, 1983.

[84] C. R. Wood, R. D. Kouznetsov, R. Gierens, A. Nordbo, L. Järvi, M. A. Kallistratova, and J. Kukkonen, "On the temperature structure parameter and sensible heat flux over helsinki from sonic anemometry and scintillometry," *Journal of Atmospheric and Oceanic Technology*, vol. 30, no. 8, pp. 1604–1615, 2013.

[85] J. C. Kaimal and J. J. Finnigan, *Atmospheric boundary layer flows: their structure and measurement*. Oxford University Press, 1994.

[86] J. R. Garratt, "The atmospheric boundary layer," *Earth-Science Reviews*, vol. 37, no. 1-2, pp. 89–134, 1994.

[87] J. Kaimal, J. Wyngaard, D. Haugen, O. Coté, Y. Izumi, S. Caughey, and C. Readings, "Turbulence structure in the convective boundary layer," *Journal of the Atmospheric Sciences*, vol. 33, no. 11, pp. 2152–2169, 1976.

[88] J. Kaimal and J. Gaynor, "Another look at sonic thermometry," *Boundary-Layer Meteorology*, vol. 56, no. 4, pp. 401–410, 1991.

[89] W. Skidmore, T. Travouillon, and R. Riddle, "Evaluation of sonic anemometers as highly sensitive optical turbulence measuring devices for the thirty meter telescope site testing campaign," in *Ground-based and Airborne Telescopes*, vol. 6267, p. 62671Z, International Society for Optics and Photonics, 2006.

[90] Y.-X. Ren, M. Li, K. Huang, J.-G. Wu, H.-F. Gao, Z.-Q. Wang, and Y.-M. Li, "Experimental generation of laguerre-gaussian beam using digital micromirror device," *Applied Optics*, vol. 49, no. 10, pp. 1838–1844, 2010.

[91] M. Mirhosseini, O. S. Magana-Loaiza, C. Chen, B. Rodenburg, M. Malik, and R. W. Boyd, "Rapid generation of light beams carrying orbital angular momentum," *Optics Express*, vol. 21, no. 25, pp. 30196–30203, 2013.

[92] P. J. Rodrigo, I. R. Perch-Nielsen, and J. Glückstad, "High-speed phase modulation using the rpc method with a digital micromirror-array device," *Optics Express*, vol. 14, no. 12, pp. 5588–5593, 2006.

[93] E. Otte, C. Schlickriede, C. Alpmann, and C. Denz, "Complex light fields enter a new dimension: holographic modulation of polarization in addition to amplitude and phase," in *Complex Light and Optical Forces IX*, vol. 9379, p. 937908, International Society for Optics and Photonics, 2015.

[94] Z. Yu, H. Chen, Z. Chen, J. Hao, and J. Ding, "Simultaneous tailoring of complete polarization, amplitude and phase of vector beams," *Optics Communications*, vol. 345, pp. 135–140, 2015.

[95] J. Albero, I. Moreno, J. A. Davis, D. M. Cottrell, and D. Sand, "Generalized phase diffraction gratings with tailored intensity," *Optics Letters*, vol. 37, no. 20, pp. 4227–4229, 2012.

[96] V. Arrizón, U. Ruiz, R. Carrada, and L. A. González, "Pixelated phase computer holograms for the accurate encoding of scalar complex fields," *JOSA A*, vol. 24, no. 11, pp. 3500–3507, 2007.

[97] V. Arrizón, "Optimum on-axis computer-generated hologram encoded into low-resolution phase-modul ation devices," *Optics Letters*, vol. 28, no. 24, pp. 2521–2523, 2003.

[98] V. Arrizón, G. Méndez, and D. Sánchez-de La-Llave, "Accurate encoding of arbitrary complex fields with amplitude-only liquid crystal spatial light modulators," *Optics Express*, vol. 13, no. 20, pp. 7913–7927, 2005.

[99] J. L. M. Fuentes and I. Moreno, "Random technique to encode complex valued holograms with on axis reconstruction onto phase-only displays," *Optics Express*, vol. 26, no. 5, pp. 5875–5893, 2018.

[100] C. Wang, N. Chen, G. Situ, and Y. Yu, "Phase-only hologram encoding based on one-dimensional grating function," *Acta Optica Sinica*, vol. 37, pp. 75–80, 09 2017.

[101] C. Rosales-Guzmán, N. Bhebhe, and A. Forbes, "Simultaneous generation of multiple vector beams on a single slm," *Optics Express*, vol. 25, no. 21, pp. 25697–25706, 2017.

[102] S. Scholes, R. Kara, J. Pinnell, V. Rodríguez-Fajardo, and A. Forbes, "Structured light with digital micromirror devices: a guide to best practice," *Optical Engineering*, vol. 59, no. 4, p. 041202, 2019.

[103] E. Franke, D. Wenzel, and D. Davidson, "Measurement of microdisplacements by machine vision photogrammetry (dismap)," *Review of Scientific Instruments*, vol. 62, no. 5, pp. 1270–1279, 1991.

[104] R. C. Gonzalez and R. E. Woods, "Digital image processing addison-wesley," *Reading, Ma*, vol. 2, 1992.

[105] M. Jourlin and J. C. Pinoli, "Logarithmic image processing: the mathematical and physical framework for the representation and processing of transmitted images," in *Advances in Imaging and Electron Physics*, vol. 115, pp. 129–196, Elsevier, 2001.

[106] A. F. Abouraddy and K. C. Toussaint Jr, "Three-dimensional polarization control in microscopy," *Physical Review Letters*, vol. 96, no. 15, p. 153901, 2006.

[107] B. J. Roxworthy and K. C. Toussaint Jr, "Optical trapping with π-phase cylindrical vector beams," *New Journal of Physics*, vol. 12, no. 7, p. 073012, 2010.

[108] W. Cheng, J. W. Haus, and Q. Zhan, "Propagation of vector vortex beams through a turbulent atmosphere," *Optics Express*, vol. 17, no. 20, pp. 17829–17836, 2009.

[109] V. Parigi, V. D'Ambrosio, C. Arnold, L. Marrucci, F. Sciarrino, and J. Laurat, "Storage and retrieval of vector beams of light in a multiple-degree-of-freedom quantum memory," *Nature Communications*, vol. 6, no. 1, pp. 1–7, 2015.

[110] X. Li, T.-H. Lan, C.-H. Tien, and M. Gu, "Three-dimensional orientation-unlimited polarization encryption by a single optically configured vectorial beam," *Nature Communications*, vol. 3, no. 1, pp. 1–6, 2012.

[111] S. C. Tidwell, D. H. Ford, and W. D. Kimura, "Generating radially polarized beams interferometrically," *Applied Optics*, vol. 29, no. 15, pp. 2234–2239, 1990.

[112] B. Lim, P. Phua, W. Lai, and M. Hong, "Fast switchable electro-optic radial polarization retarder," *Optics Letters*, vol. 33, no. 9, pp. 950–952, 2008.

[113] S. Chen, X. Zhou, Y. Liu, X. Ling, H. Luo, and S. Wen, "Generation of arbitrary cylindrical vector beams on the higher order poincaré sphere," *Optics Letters*, vol. 39, no. 18, pp. 5274–5276, 2014.

[114] G. Machavariani, Y. Lumer, I. Moshe, A. Meir, and S. Jackel, "Efficient extra-cavity generation of radially and azimuthally polarized beams," *Optics Letters*, vol. 32, no. 11, pp. 1468–1470, 2007.

[115] D. Naidoo, F. S. Roux, A. Dudley, I. Litvin, B. Piccirillo, L. Marrucci, and A. Forbes, "Controlled generation of higher-order Poincaré sphere beams from a laser," *Nature Photonics*, vol. 10, p. 327, 2016.

[116] V. Niziev, R. Chang, and A. Nesterov, "Generation of inhomogeneously polarized laser beams by use of a sagnac interferometer," *Applied Optics*, vol. 45, no. 33, pp. 8393–8399, 2006.

[117] N. Radwell, R. Hawley, J. Götte, and S. Franke-Arnold, "Achromatic vector vortex beams from a glass cone," *Nature Communications*, vol. 7, no. 1, pp. 1–6, 2016.

[118] Y. Kozawa and S. Sato, "Generation of a radially polarized laser beam by use of a conical brewster prism," *Optics Letters*, vol. 30, no. 22, pp. 3063–3065, 2005.

[119] G. Milione, H. Sztul, D. Nolan, J. Kim, M. Etienne, J. McCarthy, J. Wang, and R. Alfano, "Cylindrical vector beam generation from a multi elliptical core

optical fiber," in *CLEO: Science and Innovations*, p. CTuB2, Optical Society of America, 2011.

[120] M. Stalder and M. Schadt, "Linearly polarized light with axial symmetry generated by liquid-crystal polarization converters," *Optics Letters*, vol. 21, no. 23, pp. 1948–1950, 1996.

[121] P. Chen, W. Ji, B.-Y. Wei, W. Hu, V. Chigrinov, and Y.-Q. Lu, "Generation of arbitrary vector beams with liquid crystal polarization converters and vector-photoaligned q-plates," *Applied Physics Letters*, vol. 107, no. 24, p. 241102, 2015.

[122] F. Cardano, E. Karimi, S. Slussarenko, L. Marrucci, C. de Lisio, and E. Santamato, "Polarization pattern of vector vortex beams generated by q-plates with different topological charges," *Applied Optics*, vol. 51, no. 10, pp. C1–C6, 2012.

[123] Z. Bomzon, G. Biener, V. Kleiner, and E. Hasman, "Radially and azimuthally polarized beams generated by space-variant dielectric subwavelength gratings," *Optics Letters*, vol. 27, no. 5, pp. 285–287, 2002.

[124] G. Machavariani, Y. Lumer, I. Moshe, A. Meir, and S. Jackel, "Spatially-variable retardation plate for efficient generation of radially-and azimuthally-polarized beams," *Optics Communications*, vol. 281, no. 4, pp. 732–738, 2008.

[125] S. Fürhapter, A. Jesacher, C. Maurer, S. Bernet, and M. Ritsch-Marte, "Spiral phase microscopy," in *Advances in Imaging and Electron Physics*, vol. 146, pp. 1–59e, Elsevier, 2007.

[126] V. D'ambrosio, F. Baccari, S. Slussarenko, L. Marrucci, and F. Sciarrino, "Arbitrary, direct and deterministic manipulation of vector beams via electrically-tuned q-plates," *Scientific Reports*, vol. 5, no. 1, pp. 1–5, 2015.

[127] V. K. Inavalli and N. K. Viswanathan, "Switchable vector vortex beam generation using an optical fiber," *Optics Communications*, vol. 283, no. 6, pp. 861–864, 2010.

[128] B. Ndagano, H. Sroor, M. McLaren, C. Rosales-Guzmán, and A. Forbes, "Beam quality measure for vector beams," *Optics Letters*, vol. 41, no. 15, pp. 3407–3410, 2016.

[129] W. K. Wootters, "Entanglement of formation and concurrence.," *Quantum Information & Computation*, vol. 1, no. 1, pp. 27–44, 2001.

[130] B. Jack, J. Leach, H. Ritsch, S. Barnett, M. Padgett, and S. Franke-Arnold, "Precise quantum tomography of photon pairs with entangled orbital angular momentum," *New Journal of Physics*, vol. 11, no. 10, p. 103024, 2009.

[131] Y. Liu, X. Ling, X. Yi, X. Zhou, H. Luo, and S. Wen, "Realization of polarization evolution on higher-order poincaré sphere with metasurface," *Applied Physics Letters*, vol. 104, no. 19, p. 191110, 2014.

[132] B. Ndagano, B. Perez-Garcia, F. S. Roux, M. McLaren, C. Rosales-Guzman, Y. Zhang, O. Mouane, R. I. Hernandez-Aranda, T. Konrad, and A. Forbes, "Characterizing quantum channels with non-separable states of classical light," *Nature Physics*, vol. 13, no. 4, p. 397, 2017.

[133] T. A. Smyth, D. W. Jackson, and J. A. G. Cooper, "Three dimensional airflow patterns within a coastal trough–bowl blowout during fresh breeze to hurricane force winds," *Aeolian Research*, vol. 9, pp. 111–123, 2013.

[134] M. Malik, M. O'Sullivan, B. Rodenburg, M. Mirhosseini, J. Leach, M. P. Lavery, M. J. Padgett, and R. W. Boyd, "Influence of atmospheric turbulence on optical communications using orbital angular momentum for encoding," *Optics Express*, vol. 20, no. 12, pp. 13195–13200, 2012.

[135] S. Zhao, J. Leach, L. Gong, J. Ding, and B. Zheng, "Aberration corrections for free-space optical communications in atmosphere turbulence using orbital angular momentum states," *Optics Express*, vol. 20, no. 1, pp. 452–461, 2012.

[136] M. Cheng, L. Guo, J. Li, and Y. Zhang, "Channel capacity of the oam-based free-space optical communication links with bessel–gauss beams in turbulent ocean," *IEEE Photonics Journal*, vol. 8, no. 1, pp. 1–11, 2016.

[137] R. J. Noll, "Zernike polynomials and atmospheric turbulence," *JOSA*, vol. 66, no. 3, pp. 207–211, 1976.

[138] V. N. Mahajan and G.-m. Dai, "Orthonormal polynomials in wavefront analysis: analytical solution," *JOSA A*, vol. 24, no. 9, pp. 2994–3016, 2007.

[139] R. J. Noll, "Zernike polynomials and atmospheric turbulence," *JOSA*, vol. 66, no. 3, pp. 207–211, 1976.

[140] V. N. Mahajan, "Optical imaging and aberrations, part ii," *Wave Diffraction Optics*, vol. 2, 2001.

[141] N. Mphuthi, R. Botha, and A. Forbes, "Are bessel beams resilient to aberrations and turbulence?," *JOSA A*, vol. 35, no. 6, pp. 1021–1027, 2018.

[142] N. Bornman, A. Forbes, and A. Kempf, "Random number generation & distribution out of thin (or thick) air," *Journal of Optics*, 2020.

[143] J. P. Bos, M. C. Roggemann, and V. R. Gudimetla, "Anisotropic non-kolmogorov turbulence phase screens with variable orientation," *Applied Optics*, vol. 54, no. 8, pp. 2039–2045, 2015.

[144] A. D. McAulay, "Generating kolmogorov phase screens for modeling optical turbulence," in *Laser Weapons Technology*, vol. 4034, pp. 50–57, International Society for Optics and Photonics, 2000.

[145] B. M. Welsh, "Fourier-series-based atmospheric phase screen generator for simulating anisoplanatic geometries and temporal evolution," in *Propagation and Imaging through the Atmosphere*, vol. 3125, pp. 327–338, International Society for Optics and Photonics, 1997.

[146] B. L. McGlamery, "Restoration of turbulence-degraded images," *JOSA*, vol. 57, no. 3, pp. 293–297, 1967.

[147] C. Rosales-Guzmán and A. Forbes, *How to shape light with spatial light modulators*. SPIE Press, 2017.

[148] D. Flamm, D. Naidoo, C. Schulze, A. Forbes, and M. Duparré, "Mode analysis with a spatial light modulator as a correlation filter," *Optics Letters*, vol. 37, no. 13, pp. 2478–2480, 2012.

[149] T. Konrad, F. De Melo, M. Tiersch, C. Kasztelan, A. Aragão, and A. Buchleitner, "Evolution equation for quantum entanglement," *Nature physics*, vol. 4, no. 2, p. 99, 2008.